2011

Design of fault tolerant control system for individual blade control helicopters

Sergio Tamayo
West Virginia University

DESIGN OF FAULT TOLERANT CONTROL SYSTEM FOR INDIVIDUAL BLADE CONTROL HELICOPTERS

by

Sergio Tamayo

Dissertation submitted to the College of Engineering and Mineral Resources
at West Virginia University
in partial fulfillment of the requirements
for the degree of

Doctor of Philosophy
in
Aerospace Engineering

Approved by
Larry Banta, PhD.
Bojan Cukic, PhD.
Marcello Napolitano, PhD.
Mario Perhinschi, PhD., Chair.
Jacky Prucz, PhD.

Department of Mechanical and Aerospace Engineering

Morgantown, West Virginia
2011

ABSTRACT

Design of Fault Tolerant Control System for Individual Blade Control Helicopters

Sergio Tamayo

This dissertation presents the development of a fault tolerant control scheme for helicopters fitted with individually controlled blades. This novel approach attempts to improve fault tolerant capabilities of helicopter control system by increasing control redundancy using additional actuators for individual blade input and software re-mixing to obtain nominal or close to nominal conditions under failure. An advanced interactive simulation environment has been developed including modeling of sensor failure, swashplate actuator failure, individual blade actuator failure, and blade delamination to support the design, testing, and evaluation of the control laws. This simulation environment is based on the blade element theory for the calculation of forces and moments generated by the main rotor. This discretized model allows for individual blade analysis, which in turn allows measuring the consequences of a stuck blade, or loss of the surface area of the blade itself, with respect to the dynamics of the whole helicopter. The control laws are based on non-linear dynamic inversion and artificial neural network augmentation, which is a mix of linear and nonlinear methods that compensates for model inaccuracies due to linearization or failure. A stability analysis based on the Lyapunov function approach has shown that bounded tracking error is guaranteed, and under specific circumstances, global stability is guaranteed as well. An analysis over the degrees of freedom of the mechanical system and its impact over the helicopter handling qualities is also performed to measure the degree of redundancy achieved with the addition of individual blade actuators as compared to a classic swashplate helicopter configuration. Mathematical analysis and numerical simulation, using reconfiguration of the individual blade control under failure have shown that this control architecture can potentially improve the survivability of the aircraft and reduce pilot workload under failure conditions.

DEDICATION

This work is dedicated to my family, for without you this would have had not been possible.

ACKNOWLEDGEMENTS

First and foremost I would like to thank my advisor Dr. Mario Perhinschi for his kind and effective help without which this work would have not been possible. Additionally, I'd like to thank the senior research team in the Unmanned Aerial Vehicle Research group at West Virginia University, Dr. Marcello Napolitano, Dr. Yu Gu, Dr. Brad Seanor, and Dr. Srikanth Gurunjaran who were always available to lend a hand to help in the development of this work.

I also would like to thank my workmates through these years: Jason Jarrell, Joshua Effland, Marco Mammarella, Sebastian Sanchez, Kerri Phillips, Jason Gross, and Hever Moncayo, who made my time at work pleasurable and whose relationship was beyond the limits and the confinements of the office or the laboratory.

To my friends in Morgantown who served as a surrogate family every time I needed them and with whom I shared so many beautiful and happy moments.

TABLE OF CONTENTS

LIST OF TABLES

LIST OF FIGURES

LIST OF ACRONYMS

DOF	Degrees of Freedom
FTTV	Fly to Trim Velocity
IBC	Individual Blade Control
IMM	Interacting Multiple Model
NBS	Total Number of Blade Segments
NLDI	Nonlinear Dynamic Inversion
NN	Neural Networks
PCH	Pseudo Control Hedging
PID	Proportional Integral and Derivative control
RFC	Reconfigurable Flight Control
RSC	Reconfigurable Speed Control
UAV	Unmanned Aerial Vehicle
UKF	Unscented Kalman Filter

LIST OF SYMBOLS

α_{H1}	Horizontal tail angle of attack
α_{HH1}	Total tail angle of attack
α_{Y}	Blade segment angle of attack
α_{TRANS}	Transformed blade segment angle of attack
α_{WF}	Body axis angle of attack fuselage
β_{IB}	Blade flapping angle
β_{WF}	Sideslip angle fuselage
β_{H1}	Sideslip angle tail
Γ	Circulation on the section
γ	Yaw angle for the airspeed over a given blade segment
δ	Control input vector
$\delta_{collective}$	Collective control increment over trim value
$\delta_{lateral}$	Lateral cyclic control increment over trim value
δ_{IB}	Blade lagging
$\delta_{longitudinal}$	Longitudinal control increment over trim value
δ_{pedals}	Pedals control increment over trim value
$\Delta\eta_{CC}$	Control input due to classic control
$\Delta\eta_{NLDI}$	Control input due to the NLDI scheme
ΔL_{HBC}, ΔM_{HBC}, ΔN_{HBC}	Delta moments at hub due to blade constraints
Δu_{LR}, Δv_{LR}, Δw_{LR}	Turbulence increments to blade segment velocities
ζ	Damping ratio
Θ, Φ, Ψ	Euler angles
θ_{blade}	Total blade angle due to inputs
θ_{0}	Blade input due to collective
θ_{twist}	Blade input due to blade twist
θft	Blade input due to the Individual Blade Control

θ_{vs}	Blade angle input from the virtual swashplate
θ_{TR}	Tail rotor blade pitch angle
θ_{dyn}	Blade angle according to the dynamic twist
λ	Total normal inflow velocity/Eigenvalues
μ_{TOT}	Normalized total velocities at the shaft
$\mu_{XH},\mu_{YH},\mu_{ZH}$	Normalized velocities at the hub
$\mu_{XS},\mu_{YS},\mu_{ZS}$	Normalized velocities at the shaft
$\mu_{XTR},\mu_{YTR},\mu_{ZTR}$	Normalized velocities at the tail rotor shaft
v_{uv}	Rotor plane aerodynamic velocity
ξ	Blade section fraction
ρ	Air density
$\sigma_u,\sigma_v,\sigma_w$	Turbulence RMS intensities
υ	Pseudocontrol vector
χ	Inversion error
χ_{MR}	Rotor wake skew angle
ψ	Blade azimuth angle
ψ_{WF}	Wind model yaw angle
ω	Angular rates/Natural frequency
Ω_T	Nominal rotor speed
Ω_{TR}	Nominal tail rotor speed
A	Desired translational dynamics gain matrix/Error stability matrix
A_{0FMR}	Steady flapping
A_{0LMR}	Steady lagging
A_1	Longitudinal cyclic blade pitch/Stability matrix for the transational states
A_2	Stability matrix for the rotational states
A_{1FMR}	Longitudinal first harmonic flapping
A_{1LMR}	Longitudinal first harmonic lagging
A_{BDSH}	Body to shaft transformation matrix

$A_{LD},B_{LD,}C_{LD},D_{LD},R_{LD}$	Input constants defining the geometry of the lag damper kinematics
A_{TR}	Blade section lift curve slope
b	Number of blades/Sensor bias/Error control matrix
B	Blade tip loss factor/Control matrix
B_1	Lateral cyclic blade pitch
B_{1FMR}	Lateral first harmonic flapping
B_{1LMR}	Lateral first harmonic lagging
B_{LCGB}	Distance along the y axis of the center of gravity to the main rotor shaft
C_1,C_2,C_3	Basis functions for the neural network
C_{LY}	Lift coefficient for the local blade segment
C_{LA}	Main rotor rolling moment coefficient
C_{MA}	Main rotor pitching moment coefficient
C_{DY}	Drag coefficient for the local blade segment
C_R	Blade chord at the root
C_T	Blade chord at the tip
C_{TA}	Main rotor thrust coefficient
C_y	Blade segment chord
D_{W0}	Uniform component of downwash at the rotor disk
D_{WC}	Cosine component of downwash
D_{WS}	Sine component of downwash
D_{WSHTR}	Uniform downwash at the tail rotor disc
e	Distance from the center of the shaft to the blade hinge/Error vector
e_{abs}	Absolute value of the transient error
e_{ss}	Steady state error
E	Error metrics evaluation
$EKXWF$	Rotor wash interference factor for the x direction
$EKZWF$	Rotor wash interference factor for the z direction
F	Stability matrix

F_δ	Axial force output from lag damper
F_P, F_R, F_T	Aerodynamic forces acting on the blade segment on blade span axes
F_{PB}, F_{RB}, F_{TB}	Aerodynamic forces acting on the blade in blade span axes
F_{P0},F_{PC},F_{PS}	Harmonic components of the blade resultant force
FPDYMR	Resultant force at blade root
F_{XA}, F_{YA}, F_{ZA}	Blade aerodynamic forces acting on the blade in shaft rotating axes
F_{XI}, F_{YI}, F_{ZI}	Blade inertial forces acting on the blade in shaft rotating axes
F_{XT}, F_{YT}, F_{ZT}	Aerodynamic and inertial acting on the blade segment in shaft rotating axes
F_{SCGB}	Distance along the x axis of the center of gravity to the main rotor shaft
FF	Surface failure factor
g	Earth gravity/Neural network input vector
g_1,g_2,g_3	Dryden turbulence coefficients
g_x,g_y,g_z	Components of gravity in each axis
HP_{MR}	Horsepower consumed by the main rotor
k	Multiplying constant for sensor failure/Weight adjustment for error/Update rate
K_{1X},K_{1Y}	Glauert downwash factors
KBLKTR	Tail rotor blockage from vertical tail
K_{FP0},K_{FPC},K_{FPS}	Harmonic weighting coefficients for blade torsional wind-up
K_p,K_d	Proportional and derivative gains
IB	Blade index
I	Blade segment index
L_{DT}	Axial displacement of lag damper
L_{HA}	Aerodynamic component of rolling moment
L_{IB}	Body to inertial axes transformation matrix
L_{MR},M_{MR},N_{MR}	Rotor moments in body axes at the fuselage center of gravity
L_u,L_v	In plane turbulence scale length

$MACHMR$	Blade segment Mach number
$MODESP$	Equivalent first torsional mode of the blade
M_b	First mass moment of the blade about the hinge
$M_{FAB,}M_{LAB}$	Aero moments about hinge-blade span axis
M_H, L_H, Q_H	Total moments at the main rotor hub
M_{FFD}	Flapping moment due to flap damper
M_{FLD}	Flapping moment due to lag damper
M_{HA}	Aerodynamic component of pitching moment
M_{LLD}	Lagging moment due to lag damper
M_{LFD}	Lagging moment due to flap damper
N_{SS}	Number of blade sections
p	Probability for actuator failure
p,q,r	Angular rates
p_S,q_S,r_S	Angular rates at the shaft
Q_{H1QWF}	Dynamic pressure at the horizontal tail
r	Constante sensor output
R_T	Main rotor radius
R_{TR}	Tail rotor radius
S	Normalization scaling matrix
S_f	Failed aerodynamic surface at the blade segment
S_y	Aerodynamic surface at the blade segment
t_f	Time step at which failure occurs
t_{31},t_{32},t_{33}	Bailey coefficients
T_H,, H_H,, J_H	Total forces at the main rotor hub
T_{HA}	Aerodynamic component of thrust
$THDYMR$	Blade segment torsional deflection
$TWST_{TR}$	Linear blade twist for the tail rotor
u_y	Total flow component at the blade segment
u_f	Channel input to be affected by actuator failure
u,v,w	Helicopter speed in body axes
U	Freestream velocity/Forward velocity

U_{ad}	Adaptive input
U_{pd}	Proportional-derivative shaping of the error
U_s	General pseudocontrol vector
U_{TA}, U_{PA}, U_{RA}	Total components of air velocity on the blade segment in blade span axes
U_{TB}, U_{PB}, U_{RB}	Total components of air velocity on the blade segment in blade span axes
U_{TD}, U_{PD}, U_{RD}	Total components of downwash on the blade segment in blade span axes
U_{TG}, U_{PG}, U_{RG}	Total components of gust on the blade segment in blade span axes
U_{TW}, U_{PW}, U_{RW}	Total components of airfarme upwash on the blade segment in blade span axes
$U_T,\ U_P,\ U_R$	Components of the airspeed on the blade segment in blade span axes
U_{YA}	Total flow component at the blade segment
V	Sideward velocity/Lyapunov function for stability
V_{Xb}, V_{Yb}, V_{Zb}	Components of the air velocity in body axes
V_{XH}, V_{YH}, V_{ZH}	Components of the helicopter velocity in hub axes
$V_{XH1}, V_{YH1}, V_{ZH1}$	Total velocity at the horizontal tail
$V_{XIH1}, V_{YIH1}, V_{ZIH1}$	Horizontal tail total interference velocity
$V_{XMRH1}, V_{YMRH1}, V_{ZMRH1}$	Rotor interference velocity at the horizontal tail
$V_{XIWF}, V_{YIWF}, V_{ZIWF}$	Total velocity components at the fuselage center of gravity
V_{XS}, V_{YS}, V_{ZS}	Components of the helicopter velocity in shaft axes
$V_{XTR}, V_{YTR}, V_{ZTR}$	Total velocities at the tail rotor in shaft axes
$V_{XTRB}, V_{YTRB}, V_{ZTRB}$	Total velocities at the tail rotor in body axes
$V_{XWF}, V_{YWF}, V_{ZWF}$	Rotor wash interference on the fuselage
x_B	State space vector in body axis coordinate system
x_I	State space vector in inertial coordinate system
$XESEGMR$	Blade segment location
X_s, Y_s, Z_s	Main rotor shaft reference frame

X_H, Y_H, Z_H	Distances between the center of gravity and the hub reference frame
X_{LD}, Y_{LD}, Z_{LD}	Component displacements of lag damper relative to pick up points
X_{MR}, Y_{MR}, Z_{MR}	Rotor forces in body axes at the fuselage center of gravity
X, Y, Z	Displacement of the helicopter's center of gravity
Y_2	Distanve from blade hinge to blade segment center
w	Weight vector
W_b	Weight of each blade
w_{BD}	Weight of the helicopter without the blades
W_{LCGB}	Distance along the z axis of the center of gravity to the main rotor shaft

1 Introduction

1.1 Problem Introduction

In September 2009, the National Transport Safety Board administrator declared 2008 as the deadliest year on record for the helicopter medical services, hence a safety recommendation was issued[1] by the same institution, placing the improvement of this type of medical services in the top 10 most wanted transportation safety objectives. This safety recommendation, addressed specifically to helicopters, suggests that the Federal Aviation Administration requires from medical service helicopters the addition of night vision systems, dual pilots and improved autopilots, among others in order to improve helicopter safety. Several incidents, that include hydraulic failure and hydraulic power loss, have instigated in turn, helicopter control failure, in some cases decreasing the capability of the helicopter to the point where the pilot can engage in recovering maneuvers and in some other cases in which the pilot could not retain control of the aircraft, culminating in the loss of the aircraft and human lives.

Helicopters are used in the evacuation of injured persons or getting medical help to accidents, because they have the ability to reach places that do not have a prepared landing strip. However, they lack the redundancy of their fixed wing counterparts when it comes to produce control forces and moments. Hence, this work proposes a new additional redundancy architecture based on individual blade control. This concept has been investigated in other areas that address vibration and cockpit noise reduction, but a systematic investigation of its fault tolerant capabilities has yet to be performed.

1.2 Literature Review

This literature review will be divided into two parts. The first one will discuss the efforts done in helicopter control and reconfiguration after failure, and the second will cover recent efforts in the development of the individual blade control concept, as a full authority alternative to the classic swashplate approach, as a tool for vibration reduction and as an option for helicopter reconfiguration under failure.

1.2.1 Control/Reconfiguration

Ever since the inception of avionics to improve the performance and flight characteristics of an aircraft, additional effort in the area of flight safety has been incremented. All these efforts have been designed to provide adequate performance and control under abnormal conditions, while producing the smallest impact on the response of the aircraft at nominal or healthy conditions. Implementation started by basically mimicking the work of experienced pilots, and then implementing alternative techniques that are not possible to be done by a human, limited by physical constraints. Fruition of these efforts has produced encouraging results in the areas of fault tolerance to sensor and actuator failure. These efforts started with analysis of reconfiguration techniques for fixed wing aircraft and have recently been extended to rotorcraft. Reconfiguration for fixed wing aircraft can be performed using redundancy of the control surfaces and the inherent characteristic of the decoupling of the dynamics. However, this still involves a highly nonlinear behavior; thus techniques such as Modern Control, Adaptive Control, Neural Networks (NN), Genetic Algorithms, Fuzzy Logic, and Robust Control, among others, have been proposed and some of them successfully implemented in full scale[2] and small scale aircraft such as Unmanned Aerial Vehicles (UAV's)[3].

In his work, Heiges[4] performs a feasibility study over the possibility of using the same (or slightly adjusted) reconfigurable control techniques from fixed wing aircraft to rotorcraft, under failure conditions. This research opened the door for other studies (Drozeski et al[5]) since it successfully stated the ability of fixed-wing techniques to be translated to rotorcraft and implement new architectures such as the inclusion of individual blade control (servo-flaps) and flapping accelerometers, to improve the flying conditions under failure. The suggested architecture for rotorcraft includes a robust multivariable baseline control design, a failure recognition module and a reconfiguration module. Reconfiguration is performed redistributing control power to the remaining control surfaces, which in this case are servo flaps located in each of the blades. This is done by means of a mixer gain matrix. A generalized inverse of the failed control effectiveness matrix is used to calculate new control mixer gains so the reference performance can be obtained. Although this study had an exploratory nature, it showed proof of concept with a solution for individual blade control such as servo flaps as an additional control surface.

Later on, Enns et al[6] described a flight control system reconfiguration for actuator failures using a classic swashplate architecture. Furthermore, an actuator geometry is suggested to work in accordance to the controller design. This is achieved by coupling the control axes so that if one of the actuator fails, reconfiguration of the swashplate can be performed without losing a great amount of helicopter maneuverability and performance. For instance, one case includes reconfiguration such that pitch and roll attitude control is maintained by sacrificing vertical control, and then vertical control is achieved by increasing forward speed so that higher inflow speeds are obtained or by increasing the rotor headspeed. The geometry reconfiguration is obtained by means of the flight computer action, given that mechanical mixing already occurs in the swashplate itself. Thus a new software "remixing" is performed in order to obtain the same or close to same performance of nominal flight conditions. Classic Proportional Integral and Derivative control (PID) and neural networks were used to test the robustness of the reconfiguration methods, Fly to Trim Velocity (FTTV) Reconfigurable Flight Control Strategy (RFC) and Rotor Speed Control (RSC) . The controller and geometry setup was tested using a high complexity nonlinear Apache helicopter simulator. Although the reconfiguration is achieving close to nominal performance, if more actuators fail, the reconfiguration is not explored, furthermore there's a significant sacrifice of performance. This architecture does not have the potential to be used as a tool for vibration alleviation under nominal conditions.

Furthermore, Leitner et al[7] implemented a neural network approach in order to improve the performance of the control, by compensating modeling errors resultant from the different conditions of the flight envelope. Test of the adaptive neural network was performed using a 6 DOF nonlinear model of the AH-64 Apache helicopter. Promising results were obtained, but further work was suggested, especially regarding the architecture of the adaptive neural network. This work not only proved that the implementation of the nonlinear dynamic inversion is feasible for helicopters with classic swashplate architecture, but also that through careful design of the neural network architecture the helicopter performance is not sacrificed. Although the research was performed under nominal conditions, the robustness of the neural networks and nonlinear dynamic inversion proved to be a feasible option for helicopters.

In a similar case, Kumar et al[8], designed and tested a reconfigurable neural network controller for a helicopter simulator. However, in this case, the flight control uses feedback error learning control to achieve the desired performance of the helicopter. Again, a conventional

controller is used to control the inner loop and an outer loop with neural networks is used to compensate for modeling errors and intrinsic nonlinearities. A simulation environment with a 6 DOF motion is used to provide the results and performance evaluation. Positive results were obtained for ADS33[9] compliance and obstacle clearance.

In more exploratory work with the use of neural networks, Qi et al[10] propose an adaptive threshold neural network method for sensor fault detection for UAV's. In this case a three layer back propagation network structure is used to approximate the nonlinear continuous functions. This setup can not only detect the failure, but the specific state that is being affected by the failure and the specific sensor that is failing. The implementation of this method is done using data acquired from a small rotorcraft UAV to train the neural networks. The adaptive threshold allows for better performance sensor failure detection, especially reducing the number of false alarms. Although this study only covered for failure detection, the fact that the neural network configuration is used in a small UAV rotorcraft not only shows that implementation is possible, solving computational problems, but also that a similar structure can be used for identification and control, using neural network methodology. In a similar way, in their work, Cork et al[11], use a different implementation than neural networks to detect sensor failures. In this case, an interacting multiple model (IMM) in conjunction with an unscented Kalman filter (UKF) is used to improve the state estimation in the presence of inertial sensor faults. Simulation results were presented for a fixed wing UAV model and comparisons were made using the reference model under failure, a slightly different model, with model mismatch. Results showed that the IMM-UKF had better performance than the models using only the UKF under sensor failure conditions. Then Qi et al[12], implemented the same technique for a rotorcraft UAV. They used the mathematical nonlinear model as the reference model and used acquired data from the small helicopter to test for the scheme, which then showed in simulations, the ability to compensate for actuator failures.

On the search for different options using artificial intelligence techniques, such as fuzzy logic, Garcia et al[13] developed a fuzzy logic controller capable to perform waypoint navigation under tail rotor failure. The work was simulated and tested for a small UAV rotorcraft. In this case, the failure does not occur for full loss of tail rotor force instead, the failure is generated by locking the tail rotor collective actuator. The fuzzy controller was chosen because of its inherent ability to handle minor errors and noise in sensor data, which is prevalent in helicopters due to

the vibration generated by the main rotor and the engine. The fuzzy rule base was developed with the help of the pilot and were tuned by hand, and included more than 800 rules, given that not only the tail rotor loop included a fuzzy logic controller but also the main rotor cyclic and collective, so appropriate navigation could be performed. Although no control stability analysis was performed, the results were satisfactory. Unfortunately, the use of fuzzy logic demands great knowledge of the system itself, and in the case of individual blade control, little data if any are available from pilots.

1.2.2 State of the Art in Individual Blade Control (IBC)

Individual blade control was born as an alternative to solve for vibrations and cockpit noise. In his work, Ham[14] demonstrates that the individual blade control was not only feasible from a physical standpoint (given that tests on the wind tunnel were performed), but also that closed-loop control was also feasible at least for vibration alleviation. Accelerometers were located strategically to monitor blade flapping and lag motion.

McKillip[15] described the design of a periodic control for an individual blade control helicopter as an extension of modern techniques for helicopter controls. An optimal control problem is outlined with cost functions specially aimed at reducing vibrations. Tests using simulation and wind-tunnel data were performed and it was shown that modal control using the IBC concept was possible for different advance ratios with a feasible reduction on computer power. This work additionally proves that IBC is not only feasible, but also allows using different techniques such as robust control and periodic control, instead of classical continuous time control.

In a similar way, Shen et al[16,17] proposed the use of a swashplateless rotor with trailing edge flaps for flight, and vibration control. In this case, the individual blade control is achieved by means of active trail edge flaps, thus changing the pitching moment of the blade indirectly by changing the orientation of the trail edge of the blade. To obtain the results, the authors implemented a swashplateless UH-60 main rotor with trailing edge flaps. Blade element method was used to analyze the performance of the main rotor under these conditions, thus a discretization of the blade, with smaller segments towards the tip, was performed. The blade pitch of the blade was computed as the sum of the blade pitch index angle and the blade pitch calculated as a function of the behavior of the trail edge flap. An analysis, proving the

performance of the main rotor without the use of a conventional swashplate and additional vibration reduction was done.

Having provided simulation results, for individual blade control using classic swashplate configuration for vibration and cockpit noise alleviation, a real implementation was the next step to take. Thus, in their work, Arnold et al[18] proved in a real helicopter a closed loop individual blade control system to reduce vibrations and cockpit noise. Their research was performed using a simulation scheme of the CH-53G helicopter, including the design of a vibration control schemes. Real time implementation was performed using Matlab/Simulink/DSpace for the closed loop and open loop cases. The helicopter was fitted with hydraulic actuators that changed the blade pitch additionally to the classic swashplate approach. For the closed loop scheme, an adaptive control was implemented using a discrete Fourier transform to process the data coming from the accelerometers located in the helicopter. These signals are then used to generate a T-Matrix[19], which establishes a linear relationship between the vector of active rotor inputs for each of the actuators and the accelerations inside the helicopter. In order to avoid problems with instability and make sure that the actuators were capable of performing the tasks generated by the controller, software restrictions were added to the output of the controller. Furthermore, not only cockpit noise and vibrations were significantly reduced, but also the power requirements at high speeds (>130 kts) were significantly reduced also. Similar work was done by Haber et al[20], who developed, manufactured, and tested the components of an individual blade control system for a UH-60 helicopter. Full scale tests were performed at NASA's Large Rotor Test Apparatus. Later work[21] was performed to test the ability of the system to reduce blade vortex interaction noise with satisfactory results.

Although individual blade control was firstly used for vibration alleviation, later on in his work, Nguyen[22] developed a blade stall active control by the use of higher harmonic control, to avoid blade stall for certain flght conditions. This is performed by using individual blade control that changes the blade pitch angle actively around the swashplate. Simulation results were obtained for a variation of the BO-105 hingeless rotor.

Having demonstrated the individual blade control as an alternative for stall, vibration and cockpit noise alleviation, research was performed to prove that a full authority swashplateless main rotor was indeed feasible. In their work, Malpica et al[23] discuss the implementation of a swashplateless helicopter with the use of trailing edge flaps. This is performed by simulating a

UH-60 main rotor fitted with the aforementioned flaps. Optimization to achieve full authority of the flight envelope with the least power required was done. Although full authority is proven, some issues regarding the structural stability of the blade were noticed.

The implementation of a full authority individual blade control system without the use of the swashplate is described and simulated by Arnold et al[24]. The design evaluated the best actuator technology for the application considering previous experience, and opted for electric servo motors, which not only allow for a weight reduction but also a simpler design, especially for robustness. The robustness of the system is improved since it's simpler to attach power supplies to an electric actuator than it is to a hydraulic one, for which additional plumbing, accessories, and pumps are needed. The system was simulated, for a 6 bladed rotor, with a failure of a decrease of 50% in the pitch amplitude. Reconfiguration was obtained by combining certain blades into groups. To control them, a cost function depending on the body axes accelerations (translational and rotational) was defined trying to obtain the same performance as without failure. In general terms, the stability is preserved to the expense of a reduction of the flight envelope.

In their work, Ganguli et al[25] evaluated the possibility of individual blade control as a way to improve the survivability of helicopters. Although no specific individual blade control technology was specified (the study was made using the blade pitch angle), analysis was performed for actuator failure for the longitudinal, lateral, and collective channels. This was done by specifying the total blade angle as the sum of the contributions made by the collective, lateral and longitudinal cyclic. Each of these values was multiplied by a damaging factor to account for the damage in the actuator, 0 for no damage at all and 1 for complete actuator failure. As a result it is clear that if one actuator fails, the failure would be reflected in all channels, it is a good alternative as a first step towards understanding the phenomenon of individual blade control under failure. The results were obtained using a BO-105 hingeless rotor. Tests at hover and forward flight were performed for different damaging factors from 0 to 1. In this case no control scheme is used and it is assumed that the pilot performs the reconfiguration himself, trying to obtain the same performance as the nominal conditions. This study ends by stating the potential of individual blade control as an innovative way of achieving helicopter robustness under failure, even with the limited conditions at which the simulations were performed.

Alternative work in the field of individual blade control has been performed, by Stevens[26] not to improve the flight envelope under failure but to acquire additional information to check for ballistic damage, blade cracks, distributed stiffness fault and loss of trim mass failure and monitor the health of the entire system. In this case, piezoelectric servo flap actuators are used to excite each of the blades, and the response, measured through modal frequencies is used to evaluate whether the system is under failure or not. Similar work in this area has been performed by Kiddy et al[27], who used eigenstructure assignment to identify damages to the blade, with the help of measured modal test data and a finite element model of the blade. These techniques allow for health system monitoring using the architecture suggested in this work, and provide a good alternative for fault detection and identification of actuator and structural failure.

1.2.3 Helicopter Accident Statistics

Accident statistics have shown the presence of hydraulic failure as one of the many contribuors in helicopter accidents. A database of helicopter accidents in the United Kingdom has been built by griffin helicopters[28] based on accidents occurring in the same country since 1997. Sorting that database, the results in Table 1 were compiled. As can be seen only 3 hydraulic failures caused major accidents, which account for 0.78% of the total amount of accidents for helicopters in the United Kingdom alone, the value is small when compared to other different failures such as mishandled controls and heavy landings. However, the development of Individual Blade Control is still significant because it can provide additional safety to medical helicopters or any other type of helicopters in situations where several lifes are at stake.

1.3 Research Objectives

The main objective of this research effort is to investigate the potential of IBC for fault tolerance, develop a fault tolerant control system, and test it through numerical simulation. In order to do this, a full helicopter simulator, with an individual blade control system, must be implemented including models for abnormal conditions of swashplate actuators, blade actuators, and blade surface.

This work aims to exploit the individual blade control potential for fault tolerant capabilities, within the conceptual framework of a “virtual swashplate”, which will be described in detail later on. The use of the virtual swashplate is a powerful tool for fault tolerant purposes,

however it limits the design of the control laws, since IBC, in itself, allows for an endless combination of blade pitch angle combinations.

Finally, the demonstration of numerical evaluations of the helicopter under failure and under the action of the control system, are required for full evaluation of the fault tolerant control system. The control system will include a Nonlinear Dynamic Inversion (NLDI) augmented with Neural Networks (NN), which has provided with very good properties to stabilize complex nonlinear systems, especially under failure.

The research objectives can be summed up in the following personal contributions:

- Development of an individual blade control simulator capable of simulating several types of actuator abnormal conditions.
- Implementation of individual blade control as an alternative for fault tolerant capabilities in single main rotor helicopters.
- Design of control laws specifically aimed at the reinforcement of individual blade control as a comprehensive technique for fault tolerant helicopters.
- Application of a custom error metrics for the design and analysis of fault detection and identification schemes.

1.4 Overview of the Thesis

In this thesis, a novel approach to the analysis of individual blade control is performed. Special attention is given to this technology as an alternative technique to improve the fault tolerant capabilities of a helicopter. Development of adaptive control and reconfiguration techniques is also performed with extensive use of computational tools.

The next chapter contains an overview of the helicopter mathematical model, and the reasons behind the selection of such a model and a brief discussion over the different methods for calculating the main rotor forces. Then, an overview of the Individual Blade Control System and a comparison with the classic swashplate configuration, along with a detailed description of the different techniques for the implementation of the IBC is presented. In Chapter 4, the simulation environment designed with the specific purpose of the evaluation of the control algorithms is described. The modeling of the failures for the swashplate actuator, blade actuator, sensor, and surface delamination is also discussed. In Chapter 5, a detailed overview of the design of the fault tolerant control strategy and implementation is presented along with the

results for each of the particular failures. Chapter 6 includes the analysis of the controller performance for each of the failures. Finally the conclusions and suggestions for future work are presented.

Table 1 Helicopter accident causes in the United Kingdom 1997 - present[29]

Accident Cause	Number (%)	Accident Cause	Number (%)
Mishandled Controls	(23.32%) 90	Landing Area Unsuitable	(0.78%) 3
Heavy Landing	(20.21%) 78	Mid Air Collision	(0.78%) 3
Dynamic Rollover	(11.92%) 46	Over Pitching	(0.78%) 3
Loss Of Control VMC	(8.81%) 34	Authority Investigation	(0.78%) 3
Tail Rotor Strike	(6.74%) 26	Control Restriction	(0.52%) 2
Drivetrain Failure	(4.92%) 19	External Load Hit	(0.52%) 2
Engine Failure	(4.92%) 19	Foreign Object Damage	(0.52%) 2
Wire Strike	(4.40%) 17	Fuel Contamination	(0.52%) 2
Engine Power Loss	(3.89%) 15	Ground Collision	(0.52%) 2
Loss Of Control IMC	(3.89%) 15	Hydraulic Deselection	(0.52%) 2
Under Investigation	(3.89%) 15	Mast Bumping	(0.52%) 2
Maintenance Error	(3.37%) 13	Mechanical Defect	(0.52%) 2
No Fault Found	(3.11%) 12	Previous Overtemp	(0.52%) 2
Collision with Ground Object	(2.85%) 11	Role Damaged	(0.52%) 2
Airframe Failure [Break Up]	(2.59%) 10	Autopilot Disengagement	(0.26%) 1
Main Rotor Struck Tailboom	(2.59%) 10	Baggage Contents Lost	(0.26%) 1
Smoke In Cockpit	(2.07%) 8	Birdstrike	(0.26%) 1
Anti Torque Failure	(1.81%) 7	Control Friction Left On	(0.26%) 1
Lightning Strike	(1.81%) 7	Control System Defect	(0.26%) 1
Distraction	(1.55%) 6	Crew Hit By Rotors	(0.26%) 1
Downwind Approach	(1.55%) 6	Crew Incapacitation	(0.26%) 1
Insufficient Power Available	(1.55%) 6	Crew Lost	(0.26%) 1
Loss Of Tail Rotor Eff.	(1.55%) 6	Door Detached	(0.26%) 1
Training Rollover	(1.55%) 6	Fuel Cap Not Fitted	(0.26%) 1
Windshear	(1.55%) 6	Fuel Spillage	(0.26%) 1
Carb Icing	(1.30%) 5	Gauge Fault	(0.26%) 1
Collision with water	(1.30%) 5	Hydraulic Failure	(0.26%) 1
Fuel Starvation	(1.30%) 5	Lack Of Seat Cushion	(0.26%) 1
Manufacturing Defect	(1.30%) 5	Landing Gear Retraction	(0.26%) 1
Rotor System Failure	(1.30%) 5	Low Fuel State	(0.26%) 1
Vibration In Flight	(1.30%) 5	Low Rotor RPM	(0.26%) 1
Vortex Ring State	(1.30%) 5	Mishandled Malfunction	(0.26%) 1
Downwash Related	(1.04%) 4	Changed Course	(0.26%) 1
Electrical Fault	(1.04%) 4	Overweight	(0.26%) 1
Fouled Controls	(1.04%) 4	Previous Overspeed	(0.26%) 1
Fuel Exhaustion	(1.04%) 4	Rotated During Startup	(0.26%) 1
Loss of Fenestron Control	(1.04%) 4	Rotor Brake Application	(0.26%) 1
Student Overpowered Instructor	(1.04%) 4	Rotors Turning w/o Pilot	(0.26%) 1
Undetermined	(1.04%) 4	Spurious Fire Warning	(0.26%) 1
Anti Torque Defect	(0.78%) 3	Static Rollover	(0.26%) 1
Cowling detatched in flight	(0.78%) 3	Turbulence Encountered	(0.26%) 1
Fire Damage	(0.78%) 3	Unidentified Noise	(0.26%) 1
Fuel System Defect	(0.78%) 3	Unlicensed Pilot Owner	(0.26%) 1
Inadvertant Control	(0.78%) 3	Wake Vortex Encounter	(0.26%) 1

2 Helicopter Mathematical Model

Mathematical models provide the ability to reproduce the behavior of a real rigid body in an artificial environment like a computer. In the case of helicopters, this is a complex process that includes considerably more variables than its fixed wing cousin. An analysis with the different approaches for main rotor helicopter modeling and the specific method chosen for this work are presented next.

2.1 Main Rotor Modeling Methods

In the modeling of a helicopter, the most important part is how the forces and moments generated by the main rotor are calculated, considering that these forces and moments provide the ability to the helicopter to fly.

There are several approaches to main rotor modeling that can be divided into 3 categories: momentum theory, blade element theory, and vortex theory.

2.1.1 Momentum Theory

Momentum theory[30,31] is based on the classic laws of conservation in fluid mechanics, such as the conservation of momentum and the conservation of mass and energy. The main rotor is considered a simple input/output system by defining an actuator disk through which a mass of air is accelerated. Using Newton's law, an action/reaction system is modeled by means of the action of the thrust force of the air on the blades and the reaction of the wake of air that is accelerated downwards. Therefore, there's a loss of energy that is transferred to the wake that comes from the drag forces from the rotor blades.

The actuator disk is modeled as a circular surface of zero thickness capable of withstanding the pressure difference between the top of the rotor and the wake. Thus, considering the main rotor as an actuator disk is equivalent to considering an infinite number of rotor blades.

This method is very useful to calculate the forces when model precision is not very important, and the modeling computer has computational limitations. Thus its simplicity is its biggest advantage and also its biggest flaw. Since the analysis does not cover the action of each blade it is not recommended for individual blade analysis.

2.1.2 Blade Element Theory

The blade element theory[32,33] is based on the calculation of the forces on the blade due to its motion through the air. The blade is assumed to be a rotating wing. Therefore, the lifting line theory applies in the same way as for airplanes with minor adjustments. For this approach, it is assumed that each blade section acts as a two dimensional airfoil to produce aerodynamic forces considering the angle of attack of the blade and the wake of rotor. Thus, in order to solve this system, the momentum theory or vortex theory has to be implemented so the induced velocity at the rotor disk can be calculated and included in the analysis.

Once the inflow is solved, the airspeed along the airfoil can be calculated. Using the airspeed and the angle of attack, values for the lift and drag coefficient can be obtained by means of the airfoil wind tunnel data. With the previous values, the aerodynamic forces for the airfoil can be calculated, and since the blades are continuous sections of airfoils, a numerical integration can be performed to obtain the forces and moments for each blade. The forces and moments for each blade are then added together, thus obtaining the forces and moments for the whole main rotor.

The blade element method is a useful tool that allows for better precision, than the momentum theory, with regards to the main rotor model. Furthermore, it includes the action of each of the blades and the aerodynamic analysis is simplified. Given that additional calculations are required, more computational power is necessary to solve the dynamical system.

2.1.3 Vortex Theory:

In general terms, the vortex theory[30,34] is a rotor analysis that calculates the flow field of the rotor wake, in particular the induced velocity at the rotor disk, by using the fluid dynamic laws governing the action and influence of vorticity such as the Helmholtz, Kelvin, and Biot-Savart laws.

Vortices are generated by fluid speed difference between the bound circulation and the static field around it. However, there's also the existence of vortices in the wave and tip of the turning blades, which generate induced speeds within the wake. These vortices produce additional induced air velocity that passes through the airfoil, decreasing some of the efficiency of the rotor.

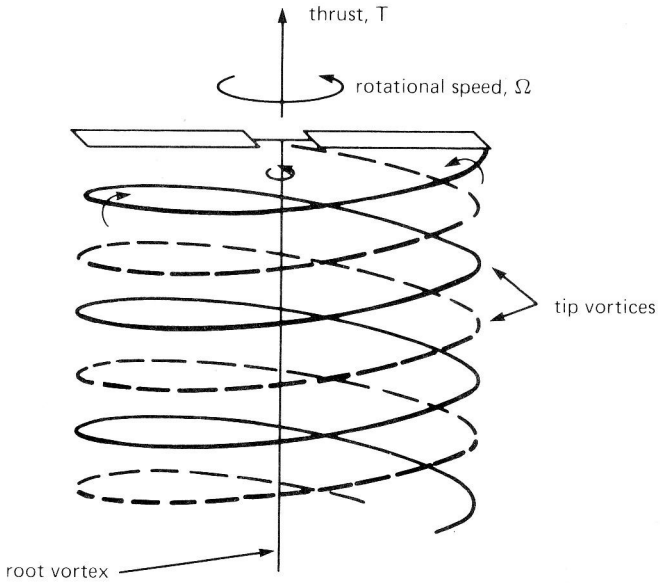

Figure 1 Main rotor wake for a two blade rotor[30]

In Figure 1, the vortex generated by the wake of the tip is represented as a continuous line, and the direction of the vortices are from down up in the direction given by the arrows shown in the figure. Root vortices are circumferential and induce air velocity towards the tip of the blade. The wake of the blades can be understood as a surface in helix form, with the root vortex as the center and in the direction of the tip vortices.

The lift generated by the main rotor can be calculated by using the circulation on an airfoil, which is given by the equation:

$$L = \rho U \Gamma \quad \textbf{(1)}$$

Where L is the lift, ρ is the fluid density, U is the free stream velocity and Γ is the circulation about the section. The difference between the different models of the vortex theory lies in the different ways to approach the calculation of the circulation.

Circulation can be calculated using 3 different techniques that are described as follows:

2.1.3.1 Actuator Disk Vortex Theory

In this case the discreteness of the blades wake is neglected, and only the vortex state around and under the actuator disk (similar as the one used for momentum theory) is taken into account[30]. Therefore, only tip and root vortices are generated for which a line in the center of the disk and a ring around the disk, are the lines around which the vortex theory is applied. However, since there's a flow of air going down because of the action of the actuator, a Venturi-shaped

surface is generated also. Thus, the surfaces outside the ring and upstream the disk, are irrotational, given that no energy is provided to them.

The results for this model, given its mathematical simplicity, can be obtained with little computational effort however, the results are exactly the same as the ones generated by the momentum theory, with the addition of computation time, and thus, no gain is generated but rather an increase in the use of the resources.

2.1.3.2 Finite Number of Blades

In this case not only the vorticity generated by the tip and root are taken into account but the slipstream of each of the blades, then instead of a cylinder, a set of helical lines and surfaces lie behind each of the blades.

Given the complexity of the surfaces and lines involved, the mathematical intricacy increases, making this problem solvable only through numerical methods with the help of high-speed computers.

For this particular model[30] the solution for the wake vorticity determines the loading on the blade. Solutions in 2D (by Prandtl) and 3D without flow through the wake (by Goldstein) are suggested as a way to solve them. Prandtl solves the vorticity lines generated by the tip of the blade, and Goldstein analyses the wake of the blade as a helical surface through wich no air passes.

2.1.3.3 Nonuniform Inflow

This method[30] is based on the numerical solution for the rotor induced velocity, loads and performance, using a complex model of the vortex wake, including the effect of the discrete tip vortices and a distorted wake geometry. In general the vortex model increases the precision of the overall main rotor model and it allows for individual blade analysis, however it comes with a high computational price given the mathematical complexity of the model itself.

2.2 Helicopter Model

Having shown the different methods for calculating moments and forces for a rotor, it was decided that the best solution for the simulator was the blade element method, given that it had the ability to use different blade angles for each of the blades in order to change the forces and moments, contrary to the momentum theory, that considers the rotor as a whole.

Furthermore, the vortex theory was rejected also given that although the accuracy is better and allows for different blade angles, the mathematical complexity that this method entails, would require fast computers that are not available for this research. Besides, the blade element theory provides enough accuracy for most applications.

Considerable research has been performed[20,21,54] based on the Sikorsky UH-60 Blackhawk helicopter to investigate the use of IBC for vibration alleviation. Howlett[35] has developed an aerodynamic and dynamic model for the purpose of helicopter simulation with pilot in the loop and as a tool for the design and analysis of control techniques. This model included complete aerodynamic characteristics, dynamic models of vehicle components, control system, and a blade element method for calculating the forces and moments for the main rotor. This model was selected as a template for the research effort presented in this thesis. The model was implemented in Matlab/Simulink and customized/modified to allow for different control configurations and the injection of a variety of upset conditions as described later. Modifications to this model based on the work by Ballin[36], were also implemented in order to improve the overall accuracy of the model and increase its computing speed.

2.2.1 Helicopter Characteristics

The UH-60 Blackhawk helicopter was developed as a multi purpose helicopter by Sikorsky to replace the UH-1 family helicopters. This helicopter has been widely used for tasks as dissimilar as an attack helicopter, ambulance and transport helicopter. Its classical layout includes 4 blades in the main rotor and the tail rotor. Both rotors are slightly tilted, the main rotor is slightly tilted to the front, with an angle with respect to the horizontal waterline of 7 degrees and the tail rotor, is tilted 20 degrees with respect to the vertical axis, as shown in Figure 2.

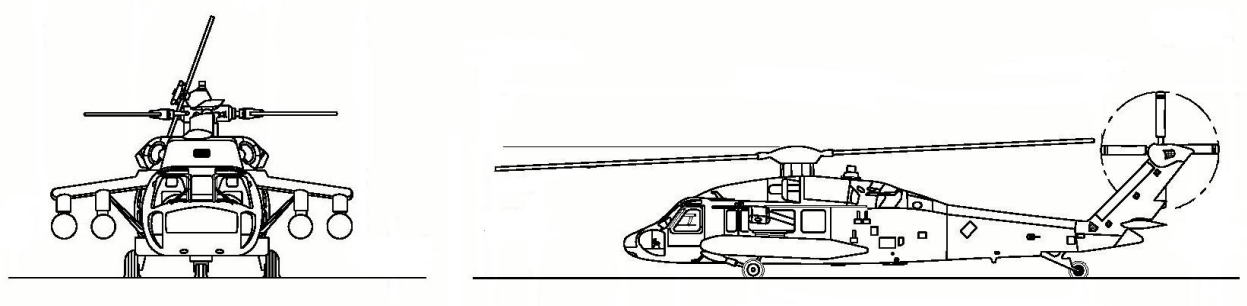

Figure 2 UH-60 Blackhawk general dimensions

The helicopter is fitted with two General Electric T700 turboshaft engines capable of generating 1890 hp each, and lift a payload of approximately 8000 lbs. Additional helicopter data is shown in Table 2.

Element	Qty
Number of blades	4
Rotor Radius	26.83 ft
Nominal Rotor Speed	27 rad/s
Blade chord	1.73 ft
Weight	16638 lbs
Weight of one blade	256.9 lb

Table 2 Blackhawk characteristics

2.2.2 Reference Frames

Three reference frames, different for the earth fixed reference frame have been used to develop and implement the helicopter simulator, and are described as follows.

2.2.2.1 Body Centered Reference Frame

This reference frame, similar to the one defined for fixed wing aircraft, is located in the helicopter's center of gravity and its x (X_B) or longitudinal axis is pointing towards the nose of the aircraft. The y (Y_B) or lateral axis is pointing towards the right of the aircraft, and finally the z (Z_B) or vertical axis, is pointing down towards the aircraft's landing gear, as the result of the cross product of the two previous axes.

2.2.2.2 Main Rotor Hub Reference Frame

This reference frame, as shown in Figure 3, is located at the center of rotation of the main rotor in the same orientation as the body axes, with the x (X_H) axis pointing towards the nose of the aircraft, the y (Y_H) axis pointing towards the right of the airframe and finally with the z (Y_H) axis pointing downwards towards the landing gear.

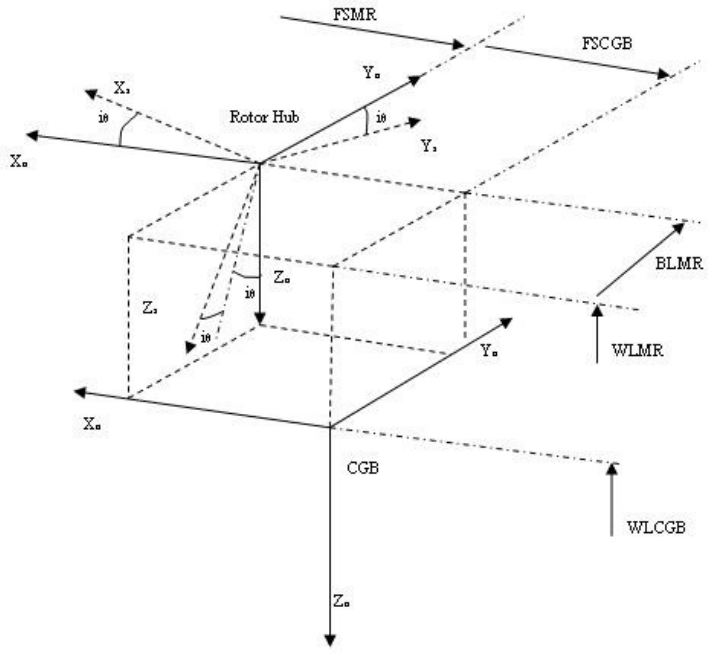

Figure 3 Body, hub, and shaft reference frames[35]

2.2.2.3 Main Rotor Shaft Reference Frame

This reference frame is located at the same point as the main rotor hub reference frame; however it is rotated according to the Euler angles of the shaft. For the Blackhawk, the main rotor shaft is tilted an angle i_θ of 7 degrees, as can be seen in Figure 3.

2.2.2.4 Main Rotor Hinge Reference Frame

As shown in Figure 4, this reference frame is located at the blade hinge, at a distance "e" from the main rotor shaft reference frame, and it rotates at the same rate as the main rotor. The z (Z_S) axis is pointing downwards in the same direction as the main rotor shaft reference frame. The y (Y_S) axis is pointing towards the main rotor blade if no lag is present. Finally, the x (X_S) axis is the cross product of the two previous axes.

2.2.2.5 Blade Span Reference Frame

This reference frame is located at each of the blade section's midpoint and is rotated with two Euler angles β and δ with respect to the main rotor hinge reference frame. The lag angle δ, is rotated around the z axis of the aforementioned reference frame and the flapping angle β, is

rotated around the hinge reference's frame x axis, forming the X_{BS}, Y_{BS}, and Z_{BS} axes as shown in Figure 4.

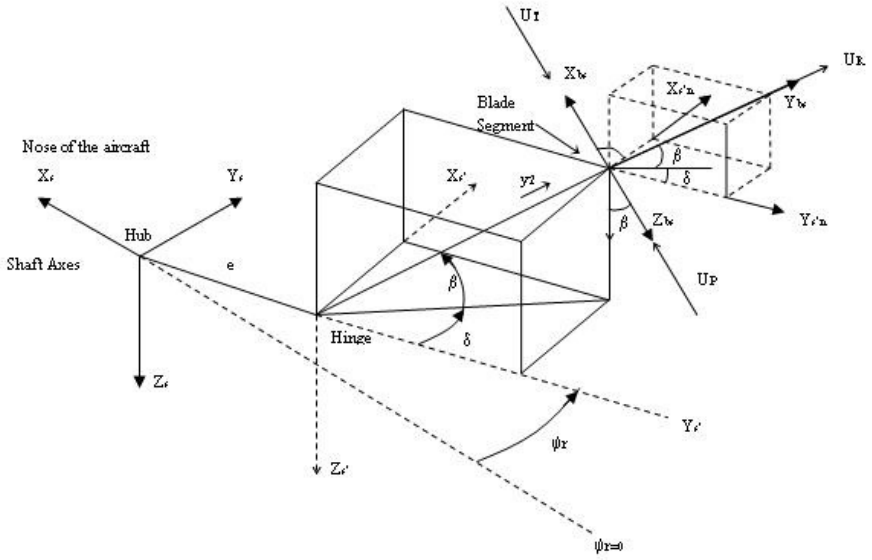

Figure 4 Shaft, hinge and blade span reference frames[35]

2.2.3 Main Rotor Model

The main rotor model which was implemented is based on the blade element theory, in which each blade is divided into segments with equal area, which allows for better analysis on high pressure areas, distributing segments in that particular section of the blade. Furthermore, this model assumes uniform downwash distribution developed from momentum theory.

2.2.3.1 Blade Geometry

To implement the blade element theory, sections of the blade must be analyzed, as shown in Figure 5, thus the need for blade segments with a given area and midpoint for force application must be calculated as seen in the equations (2) to (7).

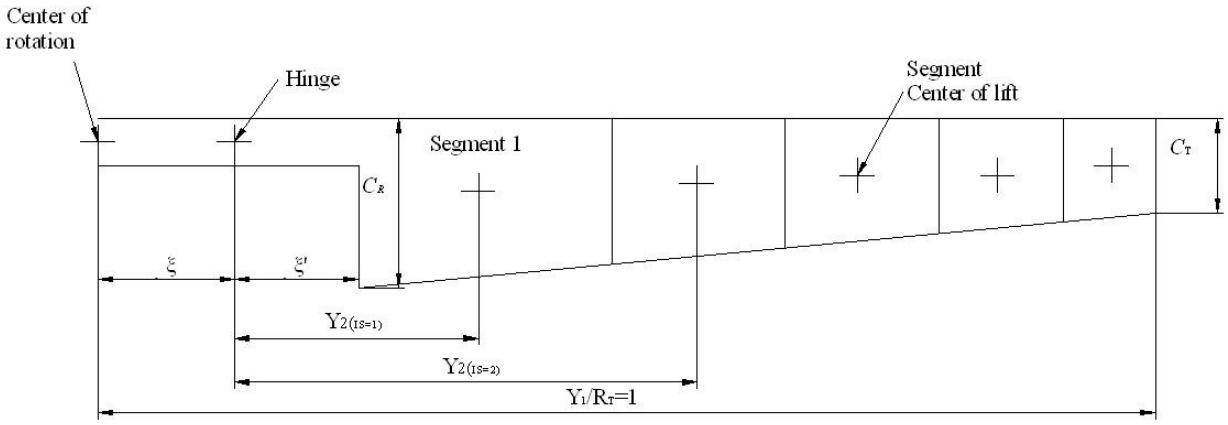

Figure 5 Sketch for blade geometry

These equations account for the discretization of the blade and definitions of the segments. It is assumed that the resultant aerodynamic force of each segment is applied on the midpoint of each segment, thus the need for the calculation of the midpoint. Calculations for the blade surface area and blade mean chord can be found in equations (8) to (10). The need to calculate for the mean chord comes from the possibility of including tapered blades into the simulation package; however, since the Blackhawk's blades are not tapered, the mean chord stays the same. Furthermore, let it be noticed that in equation (10) the value for failure factor (FF) is included in order to include the action of blade damage, as it will be explained further in this work.

$$\xi = {}^{e}\!/_{R_T} \tag{2}$$

$$\xi' = {}^{e'}\!/_{R_T} \tag{3}$$

$$y_{2_{IS=1}} = \left\{ \left[\frac{1-(\xi+\xi')^2}{2N_{SS}} \right] + (\xi+\xi')^2 \right\}^{1/2} - \xi \tag{4}$$

$$y_{2_{IS=2..N_{SS}}} = \left\{ \left[\frac{1-(\xi+\xi')^2}{N_{SS}} \right] + \left(\xi + y_{2_{(IS-1)}}\right)^2 \right\}^{1/2} - \xi \tag{5}$$

$$y_{2_{OUTB=2}} = \left\{ \left(\xi + y_{2_{(IS-1)}}\right)^2 + \left[\frac{1-(\xi+\xi')^2}{2N_{SS}} \right] \right\}^{1/2} \tag{6}$$

$$y_{2_{INB=2}} = \left\{ \left(\xi + y_{2_{(IS-1)}} \right)^2 - \left[\frac{1-(\xi+\xi')^2}{2N_{SS}} \right] \right\}^{1/2} \quad \textbf{(7)}$$

$$\Delta y_{IS} = \left[y_{OUTB_{IS}} - y_{INB_{IS}} \right] \quad \textbf{(8)}$$

$$Cy_{IS} = \left[\frac{(C_T - C_R)}{(1-\xi-\xi')} \cdot \frac{y_{OUTB_{IS}} + y_{INB_{IS}} - 2(\xi+\xi')}{2} \right] + C_R \quad \textbf{(9)}$$

$$Sy_{IS} = R_T \left(Cy_{IS} \right) \left(y_{OUTB_{IS}} - y_{INB_{IS}} \right) FF \quad \textbf{(10)}$$

2.2.3.2 Effect of Rotor Blade on Center of Gravity (CG) Position

Since that the total weight of the helicopter is given, and an independent dynamic analysis of the main rotor and the body of the helicopter is performed, the weight of the blades must be removed, and the location of the cg recalculated as a consequence. This approach allows also for independent analysis of the weight characteristics of the blades, if mass is lost due to damage. The analysis is described in equations (11) to (14).

$$w_{BD} = weight - bW_b \quad \textbf{(11)}$$

$$F_{SCGB} = \frac{weight \cdot F_{SCG} - bW_b F_{SMR}}{W_{BD}} \quad \textbf{(12)}$$

$$W_{LCGB} = \frac{weight \cdot W_{LCG} - bW_b W_{LMR}}{W_{BD}} \quad \textbf{(13)}$$

$$B_{LCGB} = \frac{weight \cdot B_{LCG} - bW_b B_{LMR}}{W_{BD}} \quad \textbf{(14)}$$

2.2.3.3 Translational Accelerations at the Rotor Hub

Before the analysis on the main rotor itself is done, the accelerations of the body of the helicopter must be transformed to the main rotor hub. Firstly, the distances from the rotor hub to the center of gravity are calculated using the distances from the hub to the helicopter's reference point, which are shown in equations (15) to (17).

$$X_H = \frac{(F_{SCGB} - F_{SMR})}{12} \quad \textbf{(15)}$$

$$Y_H = \frac{(B_{LCGB} - B_{LMR})}{12} \quad \textbf{(16)}$$

$$Z_H = \frac{\left(W_{LCGB} - W_{LMR}\right)}{12} \quad \textbf{(17)}$$

Then, the gravity vector is adjusted depending on the attitude of the helicopter, as can be seen in equations (18) to (20).

$$g_x = g \sin\theta_b \quad \textbf{(18)}$$

$$g_y = -g \sin\phi_b \cos\theta_b \quad \textbf{(19)}$$

$$g_z = -g \cos\phi_b \cos\theta_b \quad \textbf{(20)}$$

Next, the accelerations of the helicopter are transformed into hub axis, using the previously calculated distances from the center of gravity to the hub and the components of the gravity on each axis, so the kinematic effects of the motion of the helicopter can be later added to the dynamics of the main rotor. The transformations are shown in equations (21) to (23).

$$\dot{V}_{XH} = \dot{V}_{X_b} - r\dot{V}_{Y_b} + qV_{Z_b} - X_H\left(q^2 + r^2\right) + Y_H\left(pq - \dot{r}\right) + Z_H\left(pr + \dot{q}\right) + g_x \quad \textbf{(21)}$$

$$\dot{V}_{YH} = \dot{V}_{Y_b} - p\dot{V}_{Z_b} + rV_{X_b} - X_H\left(pq + \dot{r}\right) - Y_H\left(p^2 + r^2\right) + Z_H\left(qr + \dot{p}\right) + g_y \quad \textbf{(22)}$$

$$\dot{V}_{ZH} = \dot{V}_{Z_b} + p\dot{V}_{Y_b} - qV_{X_b} + X_H\left(pr + \dot{q}\right) + Y_H\left(qr + \dot{p}\right) - Z_H\left(p^2 + q^2\right) + g_z \quad \textbf{(23)}$$

2.2.3.4 Translational Velocities at the Rotor Hub

In a similar way as the accelerations, the translational velocities have to be transformed from body axes to the main rotor hub, and normalized using the main rotor radius and nominal speed, that for the Blackhawk is 27 rad/s. This transformation and normalization is described in equations (24) to (26).

$$\mu_{X_H} = \frac{1}{\Omega_T R_T}\left\{V_{X_b} + qZ_H - rY_H\right\} \quad \textbf{(24)}$$

$$\mu_{Y_H} = \frac{1}{\Omega_T R_T}\left\{V_{Y_b} + rX_H - pZ_H\right\} \quad \textbf{(25)}$$

$$\mu_{Z_H} = \frac{1}{\Omega_T R_T}\left\{V_{Z_b} - qX_H + pY_H\right\} \quad \textbf{(26)}$$

2.2.3.5 Body to Shaft Axes Transformation Matrix

Given that the main rotor shaft is slightly tilted, the angle between the helicopter's waterline and the main rotor shaft is not 90 deg, an additional transformation is required to transform the accelerations and velocities (linear and angular) from the hub to the shaft. The matrix used for the transformation is described in equation (27).

$$[A_{BDSH}] = \begin{bmatrix} \cos i_\theta & 0 & -\sin i_\theta \\ \sin i_\theta \sin i_\phi & \cos i_\phi & \cos i_\theta \sin i_\phi \\ \sin i_\theta \cos i_\phi & -\sin i_\phi & \cos i_\theta \cos i_\phi \end{bmatrix} \quad \textbf{(27)}$$

Note: i_θ and i_ϕ are euler angles with positive rotation of i_θ about Y_H.

2.2.3.6 Body Translational and Rotational Accelerations/velocities at the Hub

Using the transformation matrix described in equation (27), the velocities and accelerations at the hub are transformed into velocities and accelerations at the shaft. These transformations are shown in equations (28) to (31).

$$\begin{bmatrix} \dot{V}_{XS} \\ \dot{V}_{YS} \\ \dot{V}_{ZS} \end{bmatrix} = [A_{BDSH}] \begin{bmatrix} \dot{V}_{XH} \\ \dot{V}_{YH} \\ \dot{V}_{ZH} \end{bmatrix} \quad \textbf{(28)}$$

$$\begin{bmatrix} \dot{p}_S \\ \dot{q}_S \\ \dot{r}_S \end{bmatrix} = [A_{BDSH}] \begin{bmatrix} \dot{p} \\ \dot{q} \\ \dot{r} \end{bmatrix} \quad \textbf{(29)}$$

$$\begin{bmatrix} \mu_{XS} \\ \mu_{YS} \\ \mu_{ZS} \end{bmatrix} = [A_{BDSH}] \begin{bmatrix} \mu_{XH} \\ \mu_{YH} \\ \mu_{ZH} \end{bmatrix} \quad \textbf{(30)}$$

$$\begin{bmatrix} p_S \\ q_S \\ r_S \end{bmatrix} = [A_{BDSH}] \begin{bmatrix} p \\ q \\ r \end{bmatrix} \quad \textbf{(31)}$$

2.2.3.7 Flapping and Lagging Rate and Displacement

The flapping and lagging motion of the blade is calculated from the accelerations using Fourier expansion instead of direct integration, given that this expansion, according to Howlett, has better overall performance. This integration can be found in equations (32) to (41). The first harmonic of the cosine of the flapping, shown in equation (35), displacement is used to calculate the wake skew angle, in order to compensate for the change in the inflow distribution by forward speed and aerodynamic pitching and rolling moment on the main rotor.

$$\dot{\beta}_{IB(t)} = \ddot{\beta}_{IB(t-1)} \frac{\sin \Delta\psi_R}{\Omega} + \dot{\beta}_{IB(t-1)} \cos \Delta\psi_R \quad IB = 1, N_{BS} \tag{32}$$

$$\beta_{IB(t)} = \beta_{IB(t-1)} + \dot{\beta}_{IB(t-1)} \frac{\sin \Delta\psi_R}{\Omega} + \ddot{\beta}_{IB(t-1)} \left(\frac{1 - \cos \Delta\psi_R}{\Omega^2} \right) \quad IB = 1, N_{BS} \tag{33}$$

$$A_{0FMR} = \frac{57.3}{bs} \sum_{IB=1}^{NBS} \beta_{IB} \tag{34}$$

$$A_{1FMR} = -2 \cdot \frac{57.3}{bs} \sum_{IB=1}^{NBS} \beta_{IB} \cos \psi_{IB} \tag{35}$$

$$B_{1FMR} = -2 \cdot \frac{57.3}{bs} \sum_{IB=1}^{NBS} \beta_{IB} \sin \psi_{IB} \tag{36}$$

$$\dot{\delta}_{IB(t)} = \ddot{\delta}_{IB(t-1)} \frac{\sin \Delta\psi_R}{\Omega} + \ddot{\delta}_{IB(t-1)} \cos \Delta\psi_R \quad IB = 1, N_{BS} \tag{37}$$

$$\delta_{IB(t)} = \delta_{IB(t-1)} + \dot{\delta}_{IB(t-1)} \frac{\sin \Delta\psi_R}{\Omega} + \ddot{\delta}_{IB(t-1)} \left(\frac{1 - \cos \Delta\psi_R}{\Omega^2} \right) \quad IB = 1, N_{BS} \tag{38}$$

$$A_{0LMR} = \frac{57.3}{bs} \sum_{IB=1}^{NBS} \delta_{IB} \tag{39}$$

$$A_{1LMR} = 2 \cdot \frac{57.3}{bs} \sum_{IB=1}^{NBS} \delta_{IB} \cos \psi_{IB} \tag{40}$$

$$B_{1LMR} = 2 \cdot \frac{57.3}{bs} \sum_{IB=1}^{NBS} \delta_{IB} \sin \psi_{IB} \tag{41}$$

2.2.3.8 Main rotor Airmass Degree of Freedom

The Glauert downwash factors are calculated in equations (42) to (44) where the total mass of air flowing through the actuator disk for the momentum analysis is performed.

$$\mu_{TOT} = \left({\mu_{XS}}^2 + {\mu_{YS}}^2 + {\mu_{ZS}}^2 \right)^{1/2} \tag{42}$$

$$K_{1X} = \frac{\left({\mu_{XS}}^2 + {\mu_{YS}}^2 \right)^{1/2} \mu_{ZS}}{\mu_{TOT}} \tag{43}$$

$$K_{1Y} = \frac{\left({\mu_{XS}}^2 + {\mu_{YS}}^2 \right)^{1/2} \mu_{YS}}{\mu_{TOT}} \tag{44}$$

Thrust and main rotor coefficients are calculated according to the equations presented in (45) to (47). For this case, values from the previous time step for thrust and moments are used.

$$C_{TA} = \frac{T_{HA}}{\rho \pi \Omega_T{}^2 R_T^4} \tag{45}$$

$$C_{MHA} = \frac{M_{HA}}{\rho \pi \Omega_T{}^2 R_T^5} \tag{46}$$

$$C_{LHA} = \frac{L_{HA}}{\rho \pi \Omega_T{}^2 R_T^5} \tag{47}$$

The downwash is passed through a first order transfer function, to compensate also for forward flight and main rotor loading. The transfer functions are presented in equations (48) to (50).

$$Dw_0(s) = \frac{K_{CT} C_{TA}}{2\mu_{TOT}} \left[\frac{1}{1 + \left(\frac{T_{DW0}}{\mu_{TOT}} \right) s} \right] \tag{48}$$

$$Dw_C(s) = \frac{K_{CM} C_{MHA}}{\mu_{TOT}} \left[\frac{1}{1 + \left(\frac{T_{DW0}}{\mu_{TOT}} \right) s} \right] \tag{49}$$

$$Dw_S(s) = \frac{K_{SM} C_{LHA}}{\mu_{TOT}} \left[\frac{1}{1 + \left(\frac{T_{DW0}}{\mu_{TOT}} \right) s} \right] \tag{50}$$

After the downwash is passed through the filter, the total downwash contribution at the main rotor can be determined using equations (51) to (53). Notice that the inflow contribution is calculated for each of the blade segments, thus the subscript "*I*".

$$\begin{aligned} UPDMR_I = & -Dw_0 \cos\beta_{IB} + \left(Dw_C - K_{1X} Dw_0 \right) \cos\beta_{IB} \left(\xi \cos\psi_{IB} + y_{2n_{IS}} \cos\left(\psi + \delta \right)_{IB} \right) \\ & + \left(Dw_S + K_{1Y} Dw_0 \right) \cos\beta_{IB} \left\{ \xi \sin\psi_{IB} + y_{2n_{IS}} \sin\left(\psi + \delta \right)_{IB} \right\} \end{aligned} \tag{51}$$

$$\begin{aligned} URDMR_I = & -Dw_0 \sin\beta_{IB} + \left(Dw_C - K_{1X} Dw_0 \right) \sin\beta_{IB} \left(\xi \cos\psi_{IB} + y_{2n_{IS}} \cos\left(\psi + \delta \right)_{IB} \right) \\ & + \left(Dw_S + K_{1Y} Dw_0 \right) \sin\beta_{IB} \left\{ \xi \sin\psi_{IB} + y_{2n_{IS}} \sin\left(\psi + \delta \right)_{IB} \right\} \end{aligned} \tag{52}$$

$$\lambda = \mu_{ZS} - Dw_0 + \mu_{AVGMR} \tag{53}$$

Interference air velocities can be generated given the shape of the airframe and gusts, therefore the total blade segment interference velocities are calculated in equations (54) to (56).

$$UPIMRI_I = UPDMR_I + UPGMR_I + UPGMR_I \quad \textbf{(54)}$$

$$UTIMRI_I = UTDMR_I + UTWMR_I + UTGMR_I \quad \textbf{(55)}$$

$$URIMRI_I = URDMR_I + URWMR_I + URGMR_I \quad \textbf{(56)}$$

The blade segment velocities in the different directions of the segment, along the blade, through the blade and in the same airfoil plane are calculated in equations (57) to (64).

$$\begin{aligned} UPAMR_{IB} = &-\mu_{XS} \sin\beta_{IB} \cos\left(\psi+\delta\right)_{IB} + \mu_{YS} \sin\beta_{IB} \sin\left(\psi+\delta\right)_{IB} + \mu_{ZS} \cos\beta_{IB} \\ &+ \frac{\xi}{\Omega_T}\left\{\cos\beta_{IB}\left(q_S \cos\psi_{IB} + p_S \sin\psi_{IB}\right) - \sin\beta_{IB} \sin\delta_{IB}\left(r_S - \Omega\right)\right\} \end{aligned} \quad \textbf{(57)}$$

$$UPBMR_{IB} = \left\{-\dot{\beta}_{IB} + q_S \cos\left(\psi+\delta\right)_{IB} + p_S \sin\left(\psi+\delta\right)_{IB}\right\} \quad \textbf{(58)}$$

$$UPMR_I = UPAMR_{IB} + \frac{y_{2n_{IS}}}{\Omega_T} UPBMR_{IB} + UPIMR_I \quad \textbf{(59)}$$

$$UTAMR_{IB} = \mu_{XS} \sin\left(\psi+\delta\right)_{IB} + \mu_{YS} \cos\left(\psi+\delta\right)_{IB} - \frac{\xi}{\Omega_T} \cos\delta_{IB}\left(r_S - \Omega\right) \quad \textbf{(60)}$$

$$UTBMR_{IB} = \dot{\delta} \cos\beta_{IB} + \sin\beta_{IB}\left(p_S \cos\left(\psi+\delta\right)_{IB} - q_S \sin\left(\psi+\delta\right)_{IB}\right) - \cos\beta_{IB}\left(r_S - \Omega\right) \quad \textbf{(61)}$$

$$UTMR_I = UTMR_{IB} + \frac{y_{2n_{IS}}}{\Omega_T} UTBMR_{IB} + UTIMR_I \quad \textbf{(62)}$$

$$\begin{aligned} URAMR_{IB} = &\mu_{XS} \cos\beta_{IB} \cos\left(\psi+\delta\right)_{IB} - \mu_{YS} \cos\beta_{IB} \sin\left(\psi+\delta\right)_{IB} + \mu_{ZS} \sin\beta_{IB} \\ &+ \frac{\xi}{\Omega_T}\left\{\sin\beta_{IB}\left(q_S \cos\psi_{IB} + p_S \sin\psi_{IB}\right) + \cos\beta_{IB} \sin\delta_{IB}\left(r_S - \Omega\right)\right\} \end{aligned} \quad \textbf{(63)}$$

$$URMR_I = URAMR_{IB} + URIMR_I \quad \textbf{(64)}$$

The resultant velocity at the blade segment can be calculated, using the components of velocity along the segment as shown in equation (65), to do the airfoil analysis and calculate the aerodynamic forces at the segment. Mach number calculation is done in equation (66) for proper table look-up calculation.

$$UYAWMR_I = \left(UTMR_I^{\,2} + UPMR_I^{\,2} + URMR_I^{\,2}\right)^{1/2} \quad \textbf{(65)}$$

$$MACHMR_I = \left(UTMR_I^{\,2} + UPMR_I^{\,2}\right)^{1/2} \frac{\Omega_T R_T}{a} \quad \textbf{(66)}$$

The yaw angle of flow on segment is calculated later in order to see how much of the flow over the blade segment is along the airfoil or the direction of the blade span. This calculation is shown in equation (67).

$$\cos\gamma_I = \frac{\left|UTMR_I\right|}{\left(UTMR_I^{\,2} + URMR_I^{\,2}\right)^{1/2}} \tag{67}$$

Given the elastic characteristics of the main rotor blade, which alters the blade pitch angle under loading, the blade segment dynamic twist requires to be calculated using Fourier's series as described in equations (68) to (74). This series is used to approximate the twist of each of the blade segments due to loading, which affects the angle of attack of the segments themselves.

$$FPDYMR_{IB} = \left[F_{PB_{IB}}^{\,2} + F_{TB_{IB}}^{\,2}\right]^{1/2} \tag{68}$$

$$F_{P0_{IB}} = \frac{1}{bs}\left(\frac{b}{bs}\right)\sum_{IB=1}^{N_{BS}} FPDYMR_{IB} \tag{69}$$

$$F_{PC_{IB}} = \frac{2}{bs}\left(\frac{b}{bs}\right)\sum_{IB=1}^{N_{BS}}\left(FPDYMR_{IB}\cos\left(\psi_R + \delta\right)\right) \tag{70}$$

$$F_{PS_{IB}} = \frac{2}{bs}\left(\frac{b}{bs}\right)\sum_{IB=1}^{N_{BS}}\left(FPDYMR_{IB}\sin\left(\psi_R + \delta\right)\right) \tag{71}$$

$$MODESP_{IS} = 0.28 + 0.72\sin\left[90\left(y_{2n_{IS}} + \xi\right)\right] \tag{72}$$

$$\theta_{DYTIP_{IB}} = K_{FPO}F_{P0} + K_{FPC}F_{PC_{IB}}\cos\left(\psi + \delta\right) + K_{FPS}F_{PS_{IB}}\sin\left(\psi + \delta\right) \tag{73}$$

$$THDYMR = \theta_{DYTIP}MODESP_{IS} \tag{74}$$

Additionally, the blade has a pre-formed twist, which affects the blade pitch angle of the blade with respect to the air. This preformed twist is calculated using the segment location (XESEGMR) as can be seen in equation (75).

Having determined the variables that affect the angle of attack of the blade with respect to the air, the actual blade pitch angle can be calculated using equation (76). This equation is where the failures for main rotor collective (θ_{CUFF}), lateral cyclic (A_{1s}) and longitudinal cyclic (B_{1s}) actuator failures can be induced, by using the model that will be described in the following section. Furthermore, in case that the IBC system is used instead of the classic approach, the value for the blade pitch angle will be calculated in the same way and will be considered as a virtual swashplate. This approach allows for the use of the same architecture of the Blackhawk's Stability Augmentation System, pilot controls (the same stick disposition can be used) and also allows for better comparison with the classic approach. Furthermore, when applying failures, the value for θ_I will be subjected to actuator failure in a similar way as the lateral and longitudinal

cyclic described above, however, in this case the failure will affect the whole blade instead of the periodic value of the lateral or longitudinal swashplate angle.

The term θ_{ft} represents the value for the additional input when the hybrid system (Swashplate + IBC) is used, and it will be determined according to the fault tolerant controller.

$$XSEGMR = y_{2n_{IS}} + \xi \tag{75}$$

$$\begin{aligned}\theta_{blade_I} = {} & \theta_0 - A_{1S}\cos\left(\psi_R + \Delta_{SP}\right)_{IB} - B_{1S}\sin\left(\psi_R + \Delta_{SP}\right)_{IB} - 57.3\beta_{IB}\tan\delta_3 + 57.3\delta_{IB}K_{\alpha 1} \\ & + \left(57.3\delta_{IB}\right)^2 K_{\alpha 2} + THDYMR_I + f\left(XSEGMR\right) + \theta_{ft_I}\end{aligned} \tag{76}$$

Having determined the blade pitch angle, the blade segment angle of attack can be calculated using the components of the airspeed around the segment calculated in previous steps. This calculation is shown in equation (77).

$$\alpha_{Y_I} = \tan^{-1}\left\{\frac{\left[UTMR_I\tan\theta_{blade_I} + UPMR_I\right]\left|\cos\gamma_I\right|}{\left[UTMR_I - UPMR_I\tan\theta_{blade_I}\right]\cos^2\gamma_I}\right\} \tag{77}$$

Given the value for the segment angle of attack, the segment aerodynamic coefficients can be calculated using the wind tunnel data available for the blade's airfoil. Which is a two dimensional map for the drag and lift coefficient depending on the angle of attack, and the Mach's number, in a similar way as it's done for the fixed wing counterpart. The representation of the calculation of the coefficients is shown in equations (78) and (79).

$$C_{LY_I} = f\left(\alpha'_{Y_I}, MACHMR_I\right) \tag{78}$$

$$C_{DY_I} = f\left(\alpha'_{Y_I}, MACHMR_I\right) - \Delta C_{DMR} \tag{79}$$

With the values for the aerodynamic coefficients, the appropriate blade segment forces, in blade span axes, can be found using equations (80) to (82), which represent the 3 dimensional forces for each of the blade segments.

$$Fp_I = \frac{1}{2}\rho{\Omega_T}^2 R_T^3\left(C_Y\Delta_Y\right)_{IS} u_{Y_I}\left\{C_{LY_I}\frac{UTMR_I}{\left|\cos\gamma_I\right|} + C_{DY_I}UPMR_I\right\} \tag{80}$$

$$Ft_I = \frac{1}{2}\rho{\Omega_T}^2 R_T^3\left(C_Y\Delta_Y\right)_{IS} u_{Y_I}\left\{C_{DY_I}UTMR_I + C_{LY_I}UPMR_I\left|\cos\gamma_I\right|\right\} \tag{81}$$

$$Fr_I = \frac{1}{2}\rho{\Omega_T}^2 R_T^3\left(C_Y\Delta_Y\right)_{IS} u_{Y_I}\left\{C_{DY_I} - \frac{C_{LY_I}UPMR_I\left|\cos\gamma_I\right|}{UTMR_I}\right\}URMR_I \tag{82}$$

Having previously determined the forces for each segment, integration along the blade can be done using plain summation, assuming uniform distribution of the aerodynamic force for

the segment. Thus, the aerodynamic shears per blade are solved, and aerodynamic moments around the hinge, in blade span axes, as shown in equations (83) to (87).

$$F_{PB_{IB}} = \sum_{IS=1}^{N_{SS}} Fp_I \tag{83}$$

$$F_{TB_{IB}} = \sum_{IS=1}^{N_{SS}} Ft_I \tag{84}$$

$$F_{RB_{IB}} = \sum_{IS=1}^{N_{SS}} Fr_I \tag{85}$$

$$M_{FAB_{IB}} = R_T \sum_{IS=1}^{N_{SS}} y_{2n_{IS}} Fp_I \tag{86}$$

$$M_{LAB_{IB}} = R_T \sum_{IS=1}^{N_{SS}} y_{2n_{IS}} Ft_I \tag{87}$$

In order to have the aerodynamic coefficients to calculate for the inflow for the next time step, the aerodynamic moments about the hinge, in fixed shaft axes and flapping component only are calculated in equations (88) and (89).

$$L_{HA} = -\frac{b}{bs} \sum_{IB=1}^{N_{BS}} M_{FAB} \sin\left(\psi + \delta\right)_{IB} \tag{88}$$

$$M_{HA} = -\frac{b}{bs} \sum_{IB=1}^{N_{BS}} M_{FAB} \cos\left(\psi + \delta\right)_{IB} \tag{89}$$

To calculate the actual forces for the blade, in shaft axes, the blade and lagging motion must be taken into account. Therefore, in equations (90) to (92) the aerodynamic shears per blade, in rotating shaft axes, are calculated by implementing the appropriate transformations due to blade lag and flapping.

$$F_{XA_{IB}} = F_{RB_{IB}} \cos\beta_{IB} \sin\delta_{IB} - F_{TB_{IB}} \cos\delta_{IB} - F_{PB_{IB}} \sin\beta_{IB} \sin\delta_{IB} \tag{90}$$

$$F_{YA_{IB}} = F_{RB_{IB}} \cos\beta_{IB} \cos\delta_{IB} + F_{TB_{IB}} \sin\delta_{IB} - F_{PB_{IB}} \sin\beta_{IB} \cos\delta_{IB} \tag{91}$$

$$F_{ZA_{IB}} = -\left(F_{RB_{IB}} \sin\beta_{IB} + F_{PB_{IB}} \cos\beta_{IB}\right) \tag{92}$$

Totals for the thrust direction can be calculated, using the previously determined values for the shears per blade, so they can be used for the uniform downwash in the next time step. This calculation is performed according to equation (93).

$$T_{HA} = -\frac{b}{bs}\sum_{IB=1}^{N_{BS}} F_{ZAB_{IB}} \tag{93}$$

2.2.3.9 Blade Lag Damper Kinematics

The Blackhawk helicopter is fitted with a lag damper that restrains the lagging motion. This non-linear actuator dynamics are represented in equations (94) to (107).

$$\theta_{LDMR_{IB}} = THOAMR_{IB} - \theta_{GEOMR} \tag{94}$$

$$\begin{aligned} X_{LDMR_{IB}} = {} & A_{LDMR}\sin\beta_{IB} + B_{LDMR}\cos\left(\delta+\delta_0\right)_{IB}\cos\beta_{IB} + C_{LDMR} \\ & + D_{LDMR}\sin\left(\delta+\delta_0\right)_{IB}\cos\beta_{IB} \end{aligned} \tag{95}$$

$$Y_{LDMR_{IB}} = -R_{LDMR}\cos\theta_{LDMR_{IB}} - B_{LDMR}\sin\left(\delta+\delta_0\right)_{IB} + D_{LDMR}\cos\left(\delta+\delta_0\right)_{IB} \tag{96}$$

$$\begin{aligned} Z_{LDMR_{IB}} = {} & A_{LDMR}\cos\beta_{IB} - R_{LDMR}\sin\theta_{LDMR} - B_{LDMR}\sin\beta_{IB}\cos\left(\delta+\delta_0\right)_{IB} \\ & -D_{LDMR}\sin\left(\delta+\delta_0\right)_{IB}\sin\beta_{IB} \end{aligned} \tag{97}$$

$$LDT_{IB} = \left(X_{LDMR}{}^2 + Y_{LDMR}{}^2 + Z_{LDMR}{}^2\right)^{1/2} \tag{98}$$

$$\dot{LDT}_{IB} = \frac{LDT_{(t)} - LDT_{(t-1)}}{\Delta t} \tag{99}$$

$$F_{\dot{\delta}_{IB}} = \frac{\dot{LDT}_{IB}}{\left|\dot{LDT}_{IB}\right|} f\left(\dot{LDT}_{IB}\right) \tag{100}$$

$$\begin{aligned} M_{LLD_{IB}} = {} & -F_{\dot{\delta}_{IB}}[R_{LDMR}\cos\theta_{LDMR}\left\{\frac{X_{LDMR}}{LDT}\cos\beta - \frac{Z_{LDMR}}{LDT}\sin\beta\right\} \\ & + \frac{Y_{LDMR}}{LDT}\left\{C_{LDMR}\cos\beta + R_{LDMR}\sin\theta_{LDMR}\sin\beta\right\}]_{IB} \end{aligned} \tag{101}$$

$$M_{FLD_{IB}} = -F_{\dot{\delta}_{IB}}\left[\frac{Z_{LDMR}}{LDT}C_{LDMR} + \frac{X_{LDMR}}{LDT}R_{LDMR}\sin\theta_{LDMR}\right]_{IB} \tag{102}$$

$$M_{FFD_{IB}} = -\left[k_\beta\beta + k_{\dot{\beta}}\dot{\beta}\right]_{IB} \tag{103}$$

$$M_{FLD_{IB}} = 0 \tag{104}$$

$$\Delta L_{HBC_{IB}} = \left(M_{FLD} + M_{FFD}\right)_{IB}\sin\left(\psi+\delta\right)_{IB} \tag{105}$$

$$\Delta M_{HBC_{IB}} = \left(M_{FLD} + M_{FFD}\right)_{IB}\cos\left(\psi+\delta\right)_{IB} \tag{106}$$

$$\Delta N_{HBC_{IB}} = M_{LLD} \tag{107}$$

Once the blade damper kinematics are solved, the blade lag and blade flap acceleration can be calculated as per equations (108) and (109).

$$\ddot{\delta}_{IB} = \frac{M_b}{I_b \cos\beta}\Big[\sin\delta_{IB}\left\{\dot{V}_{YS}\sin\psi_B - \dot{V}_{XS}\cos\psi_{IB} - e\left(r_S-\Omega\right)^2\right\} - \cos\delta_{IB}\left\{\dot{V}_{XS}\sin\psi_{IB} + \dot{V}_{YS}\cos\psi_{IB} + e\left(\dot{\Omega}-\dot{r}_S\right)\right\}\Big] + \frac{\sin\beta_{IB}}{\cos\beta_{IB}}\Big[2\dot{\beta}\left(\Omega+\dot{\delta}-r_S\right) + \dot{q}_S\sin\left(\psi+\delta\right)_{IB} - \dot{p}_S\cos\left(\psi+\delta\right)_{IB}\Big] + \left(\dot{r}_S-\dot{\Omega}\right) + 2\dot{\beta}_{IB}\Big[\cos\delta_{IB}\left(q_S\sin\psi_{IB} - p_S\sin\psi_{IB} + q_S\cos\psi_{IB}\right)\Big] + \left[\frac{M_{LLD}+M_{FLD}}{I_b\cos^2\beta}\right]_{IB} - \left[\frac{M_{LAB}}{I_b\cos\beta}\right]_{IB} \quad \textbf{(108)}$$

$$\ddot{\beta}_{IB} = \frac{M_b}{I_b}\Big[\cos\beta_{IB}\left\{\dot{V}_{ZS}\sin\psi_B + e\Big[2\Omega\left(p_S\cos\psi_{IB} - q_S\sin\psi_{IB}\right) + \dot{p}_S\sin\psi_{IB} + \dot{q}_S\cos\psi_{IB}\Big] - \sin\beta_{IB}\cos\delta_{IB}\left\{\dot{V}_{YS}\sin\psi_{IB} - \dot{V}_{XS}\cos\psi_{IB} + e\left(r_S-\Omega\right)^2\right\}\Big] + \cos^2\beta_{IB}\Big[\cos\delta_{IB}\left\{\dot{p}_S\sin\psi_{IB} + \dot{q}_S\cos\psi_{IB} - 2\left(\Omega+\dot{\delta}\right)\left(p_S\cos\psi_{IB} - q_S\sin\psi_{IB}\right)\right\} - 2\Omega\sin\delta_{IB}\left({}_S\sin\psi_{IB} + q_S\cos\psi_{IB}\right)\Big] + \cos\beta_{IB}\sin\beta_{IB}\Big[2\dot{\delta}\left(r_S-\Omega\right) - \left(r_S-\Omega\right)^2\Big] + \left[\frac{M_{FAB}+M_{FFD}+M_{FLD}}{I_b}\right]_{IB} \quad \textbf{(109)}$$

Before the total forces and moments are calculated, the loading at the hinge pins must be computed, thus, the inertia shears at the hinge per blade are accounted for by means of equations (110) to (112). Although previous time step and next time step values for flapping/lagging acceleration and displacement are being used for the calculation of the forces, it is assumed that the time step discretization is small enough so no numerical or dynamic issues could be of importance.

$$F_{XI_{IB}} = M_b\Big[\cos\beta_{IB}\cos\delta_{IB}\left(\dot{r}_S - \dot{\Omega} - \ddot{\delta}_{IB}\right) + 2\sin\beta_{IB}\cos\delta_{IB}\left\{\dot{\delta}\dot{\beta} - \left(r_S-\Omega\right)\dot{\beta}\right\} + \cos\beta_{IB}\sin\delta_{IB}\left\{\dot{\delta}_{IB}{}^2 + \dot{\beta}_{IB}{}^2 - 2\left(r_S-\Omega\right)\dot{\delta}_{IB} + \left(r_S-\Omega\right)^2\right\} 2\dot{\beta}\cos\beta_{IB}\left(p_S\cos\psi_{IB} - q_S\sin\psi_{IB}\right) + \sin\beta_{IB}\sin\delta_{IB}\ddot{\beta}_{IB}\Big] - \frac{w_b}{g}\Big[\dot{V}_{XS}\sin\psi_{IB} + \dot{V}_{YS}\cos\psi_{IB}\Big] \quad \textbf{(110)}$$

$$
\begin{aligned}
F_{YI_{IB}} = M_b \Big[& \cos\beta_{IB}\cos\delta_{IB}\left\{\dot{\delta}_{IB}^2 + \dot{\beta}_{IB}^2 - 2\left(r_S - \Omega\right)\dot{\delta}_{IB} + \left(r_S - \Omega\right)^2\right\} \\
& + \sin\beta_{IB}\cos\delta_{IB}\ddot{\beta}_{IB} + \cos\beta_{IB}\sin\delta_{IB}\ddot{\delta}_{IB} \\
& -2\dot{\beta}\cos\beta_{IB}\left(p_S\sin\psi_{IB} + q_S\cos\psi_{IB}\right) + \frac{w_b e}{g M_b}\left(r_S - \Omega\right)^2 \Big] \\
& + \frac{w_b}{g}\left[\dot{V}_{XS}\cos\psi_{IB} - \dot{V}_{YS}\sin\psi_{IB}\right]
\end{aligned}
\tag{111}
$$

$$
\begin{aligned}
F_{ZI_{IB}} = M_b \Big[& \ddot{\beta}_{IB}\cos\beta_{IB} - \dot{\beta}_{IB}^2\sin\beta_{IB} + 2\dot{\beta}_{IB}\left(p_S\sin\psi_{IB} + q_S\cos\psi_{IB}\right) \\
& + \cos\beta_{IB}\sin\delta_{IB}\left\{2\left(\Omega + \dot{\delta}_{IB}\right)\left(p_S\sin\psi_{IB} + q_S\cos\psi_{IB}\right) - \dot{p}_S\cos\psi_{IB} + \dot{q}_S\sin\psi_{IB}\right\} \\
& + \cos\beta_{IB}\cos\delta_{IB}\left\{2\left(\Omega + \dot{\delta}_{IB}\right)\left(p_S\cos\psi_{IB} - q_S\sin\psi_{IB}\right) + \dot{p}_S\sin\psi_{IB} + \dot{q}_S\cos\psi_{IB}\right\} \\
& - \frac{w_b e}{g M_b}\left\{2\Omega\left(p_S\cos\psi_{IB} - q_S\sin\psi_{IB}\right) + \dot{p}_S\sin\psi_{IB} + \dot{q}_S\cos\psi_{IB}\right\} \Big] \\
& - \frac{w_b}{g}\left[\dot{V}_{ZS}\right]
\end{aligned}
\tag{112}
$$

With the shear forces for each of the blades, the total shear force at the hinge can be computed as described by equations (113) to (115).

$$F_{XT_{IB}} = F_{XA_{IB}} + F_{XI_{IB}} \tag{113}$$

$$F_{YT_{IB}} = F_{YA_{IB}} + F_{YI_{IB}} \tag{114}$$

$$F_{ZT_{IB}} = F_{ZA_{IB}} + F_{ZI_{IB}} \tag{115}$$

Finally, the main rotor's total rotor forces and moments, in shaft axes, can be calculated, using the forces for each of the blades and each blade's azimuth position, shown in equations (116) to (121).

$$T_H = -\frac{b}{bs}\sum_{IB=1}^{NBS} F_{ZT_{IB}} \tag{116}$$

$$H_H = \frac{b}{bs}\sum_{IB=1}^{NBS}\left(F_{YT_{IB}}\cos\psi_{IB} - F_{XT_{IB}}\sin\psi_{IB}\right) \tag{117}$$

$$J_H = -\frac{b}{bs}\sum_{IB=1}^{NBS}\left(F_{XT_{IB}}\cos\psi_{IB} + F_{YT_{IB}}\sin\psi_{IB}\right) \tag{118}$$

$$M_H = \frac{b}{bs}\sum_{IB=1}^{NBS}\left(eF_{ZT_{IB}}\cos\psi_{IB} + \Delta M_{HB_{IB}}\right) \tag{119}$$

$$L_H = \frac{b}{bs}\sum_{IB=1}^{NBS}\left(eF_{ZT_{IB}}\sin\psi_{IB} + \Delta L_{HB_{IB}}\right) \tag{120}$$

$$Q_H = -\frac{b}{bs}\sum_{IB=1}^{NBS}\left(eF_{XT_{IB}} + \Delta N_{HB_{IB}}\right) \tag{121}$$

To prevent heavy oscillations due to numerical issues, a first order filter is used to placate the forces and moments, as shown in equation (122).

$$\begin{bmatrix} H_{HB} \\ J_{HB} \\ T_{HB} \\ L_{HB} \\ M_{HB} \\ Q_{HB} \end{bmatrix} = \frac{1}{(T_{FILMR}s+1)}\begin{bmatrix} H_H \\ J_H \\ T_H \\ L_H \\ M_H \\ Q_H \end{bmatrix} \tag{122}$$

Given that the forces and moments are still in shaft axes, an additional transformation to body axes is required so they can be used to calculate for acceleration, velocity, attitude, etc. This transformation is performed using the transpose of matrix A_{BDSH} as per equation (123), and forces as per equation (124). For the moments, not only the hub moments are transformed but also the addition of the body forces calculated previously with their respective distances from the hub to the location of the center of gravity. The computation of the moments is shown in equation (125).

$$[A_{SHBD}] = [A_{BDSH}]^T \tag{123}$$

$$\begin{bmatrix} X_{MR} \\ Y_{MR} \\ Z_{MR} \end{bmatrix} = [A_{SHBD}]\begin{bmatrix} -H_{HB} \\ -J_{HB} \\ -T_{HB} \end{bmatrix} \tag{124}$$

$$\begin{bmatrix} L_{MR} \\ M_{MR} \\ N_{MR} \end{bmatrix} = [A_{SHBD}]\begin{bmatrix} L_{HB} \\ M_{HB} \\ Q_E \end{bmatrix} + \begin{bmatrix} Y_H Z_{MR} - Z_H Y_{MR} \\ Z_H X_{MR} - X_H Z_{MR} \\ X_H Y_{MR} - Y_H X_{MR} \end{bmatrix} \tag{125}$$

As stated before, the inflow has to be adjusted according to the forward flight conditions and the rotor wake skew angle. Equation (192) describes how this value is computed for the next time step.

$$\chi_{PMR} = \tan^{-1}\left(\frac{\mu_{XS}}{|\lambda|}\right) + A_{1FMR} \tag{126}$$

To maintain the credibility of the results, the horsepower consumed by the main rotor is calculated as shown in equation (127). The value of this can be compared with the maximum

power available for the Blackhawk and a qualitative assessment can be done over the validity of the value.

$$HP_{MR} = \frac{Q_{HB}\Omega_{MR}}{550} \tag{127}$$

2.2.4 Fuselage Model

The aerodynamic characteristics of the fuselage model have been obtained directly from wind tunnel data and apply only to the Blackhawk helicopter. The model for the fuselage takes into account in a gross way the effects of the rotor wash for the airframe, this analysis is described in equations (128) to (135), where the adjustment factor depends on the rotor wake skew angle χ and the longitudinal flapping A_{1FMR}. The angles of attack and sideslip from the fuselage are calculated in a similar way as it is done for fixed wing aircraft, as shown in equations (136) to (138), using the body axes velocities and compensating for the main rotor wash. Forces and moments are calculated using the body axes velocities and aerodynamic angles, which are then used to calculate corresponding coefficients. These coefficients are based on wind tunnel data using a look up table, which in turn is a function of the angle of attack of the fuselage, which is in wind axes. These forces are then transformed to body axes so they can be added together in the motion module.

$$V_{XIWF} = EKXWF \cdot \left(Dw_0 \Omega_T R_T \right) \tag{128}$$

$$V_{YIWF} = 0 \tag{129}$$

$$V_{ZIWF} = -EKZWF \cdot \left(Dw_0 \Omega_T R_T \right) \tag{130}$$

$$EKXWF = f\left(\chi, A_{1FMR}\right) \tag{131}$$

$$EKZWF = f\left(\chi, A_{1FMR}\right) \tag{132}$$

$$V_{XWF} = V_{X_b} + V_{XIWF} \tag{133}$$

$$V_{YWF} = V_{Y_b} \tag{134}$$

$$V_{ZWF} = V_{Z_b} + V_{ZIWF} \tag{135}$$

$$\alpha_{WF} = \tan^{-1}\left(\frac{V_{ZWF}}{|V_{XWF}|}\right) \quad \textbf{(136)}$$

$$\beta_{WF} = \tan^{-1}\left(\frac{V_{YWF}}{|V_{XWF}{}^2 + V_{ZWF}{}^2|}\right) \quad \textbf{(137)}$$

$$\psi_{WF} = \beta_{WF} \quad \textbf{(138)}$$

2.2.5 Empennage Model

This model includes the action of the horizontal and vertical tail fitted to the Blackhawk helicopter. It must be noted that the horizontal tail, for which the model is shown in equations (139) to (157), has an actuator that allows for rotation and it is used as an additional control surface, its input is generated at the control module and is represented by i_{H1} and is added to the resultant angle of attack, as can be seen in equation (155). In both cases, the aerodynamic forces are computed in the local flow wind axes system and later transformed to body axes to the aircraft's center of gravity. The mathematical model for the vertical tail follows the same logic as the horizontal plane, with little adjustments to the look up tables and velocity components.

The interference between the tail and the tail rotor and main rotor is included in this model, as shown in equations (139) to (143), thus the tail dynamic pressure blockage and downwash from the aircraft body are developed as a function of the angle of attack and sideslip, as described by equations (144) to (146). The interference is calculated using a look up table for which the inputs are the rotor wake skew angle and the rotor longitudinal flapping.

$$V_{XMRH1} = EKXH1 \cdot \left(Dw_0 \Omega_T R_T\right) \quad \textbf{(139)}$$

$$V_{YMRH1} = 0 \quad \textbf{(140)}$$

$$V_{ZMRH1} = -EKZH1 \cdot \left(Dw_0 \Omega_T R_T\right) \quad \textbf{(141)}$$

$$EKXH1 = f\left(\chi, A_{1FMR}\right) \quad \textbf{(142)}$$

$$EKZH1 = f\left(\chi, A_{1FMR}\right) \quad \textbf{(143)}$$

$$Q_{H1QWF} = f\left(\alpha_{WF}\right) \quad \textbf{(144)}$$

$$K_{QH1} = Q_{H1QWF}{}^{1/2} \quad \textbf{(145)}$$

$$E_{PSH1} = f\left(\alpha_{WF}\right) \quad \textbf{(146)}$$

$$V_{ZWFH1} = -\frac{V_{X_b}}{57.3} E_{PSH1} K_{QH1} \quad \textbf{(147)}$$

$$V_{XIH1} = V_{XMRH1} \quad \textbf{(148)}$$

$$V_{YIH1} = V_{YMRH1} \quad \textbf{(149)}$$

$$V_{ZIH1} = V_{ZMRH1} + V_{ZWFH1} \quad \textbf{(150)}$$

$$V_{XH1} = V_{X_b} K_{QH1} - qW_{HT1} + rB_{HT1} + V_{XIH1} \quad \textbf{(151)}$$

$$V_{YH1} = V_{Y_b} K_{QH1} + pW_{HT1} - rF_{HT1} + V_{YIH1} \quad \textbf{(152)}$$

$$V_{ZH1} = V_{Z_b} K_{QH1} + qF_{HT1} - pB_{HT1} + V_{ZIH1} \quad \textbf{(153)}$$

$$Q_{H1} = \frac{1}{2}\rho\left(V_{XH1}{}^2 + V_{YH1}{}^2 + V_{ZH1}{}^2\right) \quad \textbf{(154)}$$

$$\alpha_{H1} = \tan^{-1}\left(\frac{V_{ZH1}}{|V_{XH1}|}\right) \quad \textbf{(155)}$$

$$\alpha_{HH1} = i_{H1} + \alpha_{H1} \quad \textbf{(156)}$$

$$\beta_{H1} = \tan^{-1}\left(\frac{V_{YH1}}{\left|V_{XH1}{}^2 + V_{ZH!}{}^2\right|}\right) \quad \textbf{(157)}$$

The components of the velocities are solved using the body axes translational and angular velocities, rotor wash, fuselage downwash and sidewash, as shown in equations (147) to (153). The actual dynamic pressure at the tail is calculated from the resultant velocity vector (including pressure loss due to the components of the free stream flow), as described in equation (154). Based on wind tunnel data, which depends on the horizontal (and vertical) angle of attack (calculated in equation (156)), the coefficients for the forces and moments are computed. Using the coefficients and the dynamic pressure, the forces and moments can be finally calculated for the horizontal and vertical plane.

Once the aerodynamic forces and moments are calculated at the tail, proper transformation is done so they can be added up to the other forces at the helicopter's center of gravity.

2.2.6 Flight Control System Model

The flight control model described here is the one fitted to every Blackhawk helicopter and does not include the fault tolerant component, which is an important contribution of this work. In a general way, this system is designed to provide stability to the helicopter by means of analog and digital controllers fitted to a 3 axis gyro and a lateral accelerometer. The sensor failure model will be described further in this work. It also includes the models and gains for the servo actuators that drive the helicopter's swashplate and collective action. The failure model for these actuators will be described later.

2.2.7 Engine Model

A simplified engine model was developed based on the assumption that the engine delivers the power required without any dynamics. Furthermore, the values for total power consumption will be monitored so the values are kept within the power ratings given for the real engines.

2.2.8 Tail Rotor Model

The tail rotor forces and moments are calculated next, as described by equations (158) to (171). These forces and moments are computed at the center of the tilted rotor and are represented by a simplified closed form Bailey solution as per the NACA report by Bailey[37]. The airflow generated by the tail rotor is originated from the free stream and, similarly to the empennage, terms from the rotor wash and fuselage sidewash are included, as shown in equations (158) to (160). An additional step is required to transform the velocities from the location of the tail rotor to the shaft axes, given the orientation of the tail rotor, which is slightly tilted upwards around the longitudinal axis of the helicopter. After the velocities are calculated, they are normalized as shown in equations (161) to (164). The Bailey solution, shown in equations (165) to (168), has been modified from the original to fit the demands of stability and accuracy for this particular application.

The tail rotor collective is calculated by adding the value generated by the SAS command and the one generated in the previous time step as a solution to the thrust, as shown in equation (169). The downwash for the tail rotor is then computed, as described in equation (170), using the solution to the Bayley equations, which in turn is then used to calculate the thrust.

Given the proximity of the vertical tail, a blockage factor is included in the model to account for loss of thrust due to the position of the vertical tail. Similarly to other force-generating elements of the helicopter, once the forces and moments are calculated at the center of rotation of the rotor, appropriate transformations are performed so they can be added to the helicopter's center of gravity.

$$V_{XTR} = V_{XTRB} \tag{158}$$

$$V_{YTR} = V_{YTRB}\cos\Gamma_{TR} + V_{ZTRB}\sin\Gamma_{TR} \tag{159}$$

$$V_{ZTR} = -V_{YTRB}\sin\Gamma_{TR} + V_{ZTRB}\cos\Gamma_{TR} \tag{160}$$

$$\mu_{XTR} = \frac{V_{XTR}}{\Omega_{TR} R_{TR}} \tag{161}$$

$$\mu_{YTR} = \frac{V_{YTR}}{\Omega_{TR} R_{TR}} \tag{162}$$

$$\mu_{ZTR} = \frac{V_{ZTR}}{\Omega_{TR} R_{TR}} \tag{163}$$

$$\mu_{TR} = \left(\mu_{XTR}{}^2 + \mu_{YTR}{}^2\right)^{1/2} \tag{164}$$

$$t_{31} = \frac{B^2}{2} + \frac{\mu_{TR}{}^2}{4} \tag{165}$$

$$t_{32} = \frac{B^3}{3} + \frac{B\mu_{TR}{}^2}{2} \tag{166}$$

$$t_{33} = \frac{B^4}{4} + \frac{B^2\mu_{TR}{}^2}{4} \tag{167}$$

$$G = \frac{A_{TR}}{2}\left[\frac{bC}{\pi R}\right]_{TR} \tag{168}$$

$$\theta_{TR} = \frac{1}{57.3}\left[\theta_{TTR} - T_{TR_{t-1}}\left(\frac{\partial a_0}{\partial T_{TR}}\right)\tan\delta_3 + B_{1ASTR}\right] \tag{169}$$

$$D_{WSHTR_t} = \frac{G\left(\mu_{ZTR}t_{31} + \theta_{TR}t_{32} + \dfrac{TWST_{TR}}{57.3}t_{33}\right)}{2\left(\mu_{TR}{}^2 + \lambda_{TR_{t-1}}{}^2\right)^{1/2} + Gt_{31}} \tag{170}$$

$$T_{TR} = 2\rho\pi R_{TR}{}^4 DWSH_{TR}\left(\mu_{TR}{}^2 + \lambda_{TR}{}^2\right)^{1/2}\Omega_{TR}{}^2\left(\frac{\Omega_{MR}}{\Omega_T}\right)^2 KBLKTR \tag{171}$$

2.2.9 Turbulence Model

A turbulence model was implemented based on the work by McFarland et al[38]. This work describes a turbulence model adequate for a blade element model, and was successfully tested with a full 6 DOF UH-60 simulator with positive feedback from helicopter pilots, who gave a better evaluation over the realistic aspect of this new model over the previously implemented.

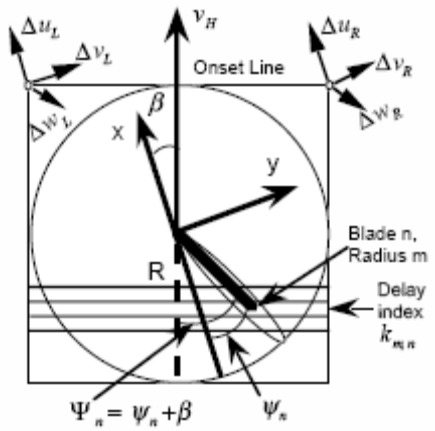

Figure 6 Rotor geometry for turbulence model[38]

This model uses a temporal and geometrical distribution algorithm that preserves the statistical characteristics of the turbulence spectra over the rotor disk, while providing velocity components to each of the segment of each blade, the geometric distribution and the increments on the each of the velocity axis are shown in Figure 6. In this case only the vertical component of stochastic turbulence was used, however this effect provides motion in all axes of the helicopter, not only translational but also rotational, given that is not applied at a single point but over a grid located externally to the helicopter's center of gravity.

$$\gamma_u = \frac{v_{uv}\Delta t}{L_u} \tag{172}$$

$$f_1 = e^{-\gamma_u} \tag{173}$$

$$f_2 = \sigma_u \left(1 - f_1\right)\sqrt{\frac{2}{\gamma_u}} \tag{174}$$

$$\gamma_v = \frac{v_{uv}\Delta t}{L_v} \tag{175}$$

$$g_1 = 2e^{-\gamma_v} \tag{176}$$

$$g_2 = -e^{-2\gamma_v} \tag{177}$$

$$g_3 = \left(\frac{\sigma_v}{\sqrt{\gamma_v}}\right)\left[1 - e^{-\gamma_v} + \left(\sqrt{3} - 1\right)e^{-\gamma_v}\gamma_v\right] \tag{178}$$

$$g_4 = -\left(\frac{\sigma_v e^{-\gamma_v}}{\sqrt{\gamma_v}}\right)\left[1 - e^{-\gamma_v} + \left(\sqrt{3}-1\right)\gamma_v\right] \quad \textbf{(179)}$$

$$\gamma_w = \frac{v_{uv}\Delta t}{L_w} \quad \textbf{(180)}$$

$$h_1 = 2e^{-\gamma_w} \quad \textbf{(181)}$$

$$h_2 = -2e^{-2\gamma_w} \quad \textbf{(182)}$$

$$h_3 = \left(\frac{\sigma_w}{\sqrt{\gamma_w}}\right)\left[1 - e^{-\gamma_w} + \left(\sqrt{3}-1\right)e^{-\gamma_w}\gamma_w\right] \quad \textbf{(183)}$$

$$h_4 = -\left(\frac{\sigma_w e^{-\gamma_w}}{\sqrt{\gamma_w}}\right)\left[1 - e^{-\gamma_w} + \left(\sqrt{3}-1\right)\gamma_w\right] \quad \textbf{(184)}$$

In a similar way as the Dryden model, the vertical turbulence scale length and the in-plane components are calculated as a function of altitude. The process by which the Dryden model is discretized is explained in reference 38. The calculation for the Dryden coefficients can be shown in equations (172) to (184). Once the coefficients are calculated, the increments for the blade segment velocities can be calculated as shown in equations (185) to (190).

$$\Delta u_L(k) = f_1 \Delta u_L(k-1) + f_2 \eta_1(k) \quad \textbf{(185)}$$

$$\Delta u_R(k) = f_1 \Delta u_R(k-1) + f_2 \eta_2(k) \quad \textbf{(186)}$$

$$\Delta v_L(k) = g_1 \Delta v_L(k-1) + g_2 \Delta v_L(k-2) + g_3 \eta_3(k) + g_4 \eta_3(k-1) \quad \textbf{(187)}$$

$$\Delta v_R(k) = g_1 \Delta v_R(k-1) + g_2 \Delta v_R(k-2) + g_3 \eta_1(k) + g_4 \eta_4(k-1) \quad \textbf{(188)}$$

$$\Delta w_L(k) = h_1 \Delta w_L(k-1) + h_2 \Delta w_L(k-2) + h_3 \eta_5(k) + h_4 \eta_5(k-1) \quad \textbf{(189)}$$

$$\Delta w_R(k) = h_1 \Delta w_R(k-1) + h_2 \Delta w_R(k-2) + h_3 \eta_6(k) + h_4 \eta_6(k-1) \quad \textbf{(190)}$$

2.2.10 Subsystem Failure Model

Modeling of actuator and sensor failures, as well as blade structural damage, are included in this simulation environment. The actuator failures modeled include abnormal operation of the lateral and longitudinal cyclic, main rotor collective, tail rotor collective, and the IBC actuators, for the architecture with the redundant system. Similarly, for the architecture where the IBC has full authority, failure can be simulated for each individual blade actuator. The failed actuator can be either locked at the position reached at the moment of failure occurrence t_f, or it can transition to a specified fixed position where it remains locked. For the first situation, the position of the failed actuator (u_f) is determined by the position of the actuator (u) as produced by the pilot input

and the control system under normal conditions at the failure time t_f, according to the following equation.

$$u_f(t) = \begin{cases} u(t) & \text{if } t < t_f \\ u(t_f) & \text{if } t \geq t_f \end{cases} \quad \textbf{(191)}$$

For the second type of actuator failure, a first order transfer function is used to model the transition to the final failed position as described by the following equation:

$$u_f(t) = \begin{cases} u(t) & \text{if } t < t_f \\ u(t_f) + \dfrac{1}{\tau_f s + 1}(u_{fail} - u(t_f)) & \text{if } t \geq t_f \end{cases} \quad \textbf{(192)}$$

where u_{fail} is the value at which the actuator will be stationary for the failure, u_f is the signal of the failed actuator and τ_f is the time constant for the transition motion of the actuator.

Three different types of sensor failures have been modeled. The first type is the additive sensor failure or the biased sensors. In this case a bias b is added to the output of the sensor after the failure occurrence time, as expressed in equation (193). Change notation for the sensors, use actual value and measured value.

$$u_f(t) = \begin{cases} u(t) & \text{if } t < t_f \\ u(t) + b & \text{if } t \geq t_f \end{cases} \quad \textbf{(193)}$$

A multiplicative sensor failure can be modeled by multiplying the nominal sensor output by a constant factor (1+k) as formulated in equation (194).

$$u_f(t) = \begin{cases} u(t) & \text{if } t < t_f \\ (1+k)u(t) & \text{if } t \geq t_f \end{cases} \quad \textbf{(194)}$$

Finally, the third type of sensor failure consists of a sensor producing a constant output. This model is expressed as equation (195).

$$u_f(t) = \begin{cases} u(t) & \text{if } t < t_f \\ r & \text{if } t \geq t_f \end{cases} \quad \textbf{(195)}$$

The blade surface damage, which can be assimilated to blade delamination or destruction produced by collision with a hard body, is simulated by decreasing the surface area (S) of the blade station which is affected by the failure by a failure factor (FF) ranging from 0 to 1, where 1 represents nominal conditions and 0 a total destruction of surface[19]. The stations are given by the number of segments simulated, at the given value of r/R. The model for this failure is described by equation (196).

$$S_f(t) = \begin{cases} S & \text{if } t < t_f \\ S * FF & \text{if } t \geq t_f \end{cases} \tag{196}$$

The total loss of surface at any station is extended to the tip, based on the assumption that the blade would break at the failed station. Mass changes due to the loss of blade surface are not considered. It should be noted that structural analysis on the damaged surface, or the changes of other physical properties of the blade due to the failure are beyond the scope of this work.

3 Individual Blade Control System

3.1 Overview of Classical Helicopter Configuration

A helicopter, as its fixed-wing cousin, relies on the lift generated by an aerodynamic airfoil accelerated through a mass of air. In the case of the fixed wing, the airfoil stays fixed to the frame of the aircraft and the aircraft moves relatively to the mass of air by means of thrust generated either by a rotary or a jet engine. In the case of a helicopter, the aerodynamic profile rotates with respect to the aircraft frame. The power is produced by a rotary engine inside the helicopter itself.

In the most classic example, the attitude of the helicopter is governed by the orientation of the main rotor, or rotors. This is achieved by means of a swashplate. The swashplate is a mechanical device that consists of a fixed and a rotary portion, as can be seen in Figure 7, where the static and static swashplate are shown, and its connecting rods to the helicopter's blades. The fixed portion is marked in blue, and hydraulic actuators work together to change the orientation of the swashplate with respect to the helicopter. This motion is generated by the pilot in the cockpit by the cyclic command, and since the swashplate can be oriented forwards-backwards and side to side, the command is called longitudinal and lateral cyclic respectively.

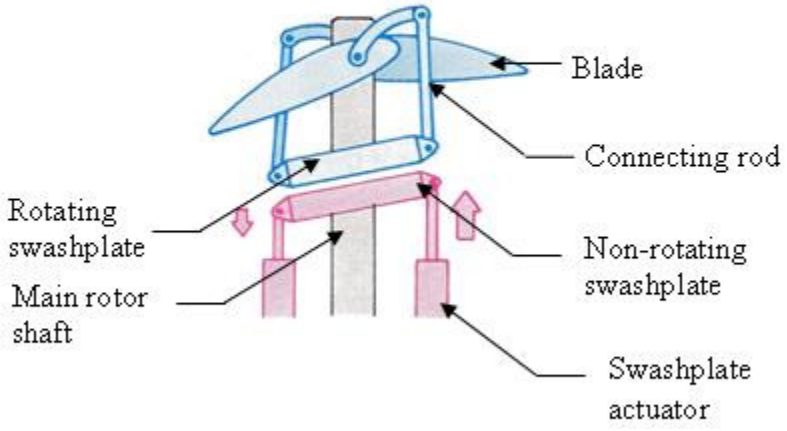

Figure 7 Swashplate schematic[39]

The top part of the swashplate has the same orientation as the one in the bottom; however, this one rotates with the main rotor providing the right orientation corresponding to the azimuth angle of the blade, which is connected to the rotating swashplate through rigid connecting rods, such that the tip of the blade generates a plane parallel to the surface of the

swashplate. The thrust of the main rotor is perpendicular to this plane, which is called the tip path plane. A representation of this plane is shown in Figure 8.

Figure 8 Tip path plane schematic[39]

The collective, which is operated by the pilot's left hand, controls how much lift is generated by increasing the average blade pitch angle over the azimuth angle. This is done by moving the whole swashplate assembly (static and rotating) up and down, without affecting the orientation of the swashplate itself. If more lift is required, the swashplate will move up, if less, the swashplate assembly will go down.

Once lift is generated, drag is also produced in the plane perpendicular to the rotor axis resulting in an increase of motor torque. A counter torque has to be generated so that the body of the helicopter does not start rotating in the opposite direction of the rotor. Several solutions have been developed over the years to solve this problem, and are discussed next.

3.1.1 Single Main Rotor

The single main rotor helicopter is the most common configuration. It relies on counteracting the torque of the motor by placing a rotating blade offset from the main rotor, called tail rotor. This rotor generates a force in the tail of the helicopter in a similar way as the main rotor does by generating lift. A clear example of this type of configuration can be seen in Figure 9. The amount of torque, generated by the tail, is changed by changing the collective pitch of the tail rotor, given that its speed is a constant multiple of the speed of the main rotor, since they are physically connected through a gearbox. The collective pitch of the tail rotor is controlled by pedals in the cockpit, which gives the ability to the aircraft of performing the yawing motion.

In some cases the tail rotor is replaced by a nozzle that pushes low pressure air using a fan, in the same direction as the air would be in the tail rotor configuration.

Figure 9 Single main rotor configuration[40]

Now, the roll and pitch are achieved by tilting the tip path plane, where the main rotor blades are located, forward or backwards, for the pitch, and left or right, for the roll. The thrust, in general terms, is assumed to be perpendicular to the rotor plane. In hover, the plane is parallel to the surface of the earth, and the thrust counteracts the action of gravity only, but once this plane is tilted, the thrust is divided in two components, one which counteracts the weight and the other, which is in the direction of the tilting, generates the roll or pitch. The change in orientation is obtained mechanically by tilting a swashplate, which allows for the main blades to rotate and change their angle as they are turning around. This movement, which is called lateral and longitudinal cyclic, is controlled by the stick in the cockpit.

Forward flight is achieved by tilting the plane forwards, thus creating a component of thrust in the same direction, as explained before, however a phenomenon of asymmetry of the lift is generated given that the advancing blade will have more airspeed than the retreating blade, given the adding effect of the rotation with the forward motion, generating in some cases transonic speeds in the advancing blade and almost stall on the retreating blade.

3.1.2 Coaxial

In this case to counteract the torque, another rotor is located on the same axis as the original one, rotating in the opposite direction, usually one is located on top of the other with such a distance that limited aerodynamic interference occurs. An example of this configuration can be seen in Figure 10. Yaw is obtained by changing the collective pitch on one or both of the rotors. Pitch and roll are generated in a similar way as the main rotor, by tilting both planes at the same time. In forward flight the asymmetry in lift no longer occurs given that the shortness of lift generated by the retreating side is counteracted by the lift generated by the other rotor in the

same position above or under it, which is in turn the advancing blade. This system has a higher mechanical complexity given the fact that dual swashplates must be used, and the linkages going to the top rotor have to go through the low rotor first.

Figure 10 Coaxial rotor configuration[41]

3.1.3 Tandem

In this case to counteract the torque, two rotors are located one in front of the other (one slightly higher than the other) rotating in different directions, as can be seen in Figure 11. To generate yaw, the front rotor tilts to one side and the rear one tilts to the opposite side. To generate pitch, the collective pitch on one of the rotors is increased while the other is decreased. Roll is generated in a similar way as with the single rotor, given that in this case both rotors tilt to the right or to the left.

Figure 11 Tandem rotor configuration[42]

3.1.4 Side by Side

This configuration is also called intermeshing rotors. In this case two counter rotating rotors are located one by the other slightly tilted to the side where they are located at, as seen in Figure 12, and turn in such a way that the blades do not colide with each other. Roll and yaw are obtained by changing the collective pitch on one rotor and going the opposite way in the other. Pitch is obtained with the collaboration of the two rotors working together by tilting forwards.

Figure 12 Side by side rotor configuration[43]

3.2 Overview of the Individual Blade Control

Several different techniques to achieve individual blade control are discussed next.

3.2.1 Blade Camber Control

This system is based on the variation of the blade's camber by mechanical means[44] or by attaching a piezoelectric material on each side of the skin of the blade, which in turn is operated through voltage application[45]. The voltage is applied differentially so the force applied to the top of the blade is different from the one on the bottom; therefore a torsion effect is applied on the blade causing the blade camber to change.

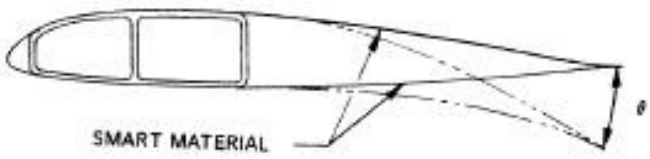

Figure 13 Blade camber control schematic[44]

3.2.2 Blade Twist Control

In this case, the twist of the blade is controlled by attaching piezoelectric materials to the spar of the blade[46]. The spar of the blade, which is usually rectangular, has a disposition of piezoelectric actuators that generates torsion once the force is applied thus, changing the blade twist.

3.2.3 Active Servo Flaps

This concept, developed by Kaman[47], relies on the fitting of a trailing edge flap operated by a servo embedded in the blade. The trailing edge is operated by means of a tiny rod that connects it with the servo, and it's operated depending on the required flying conditions.

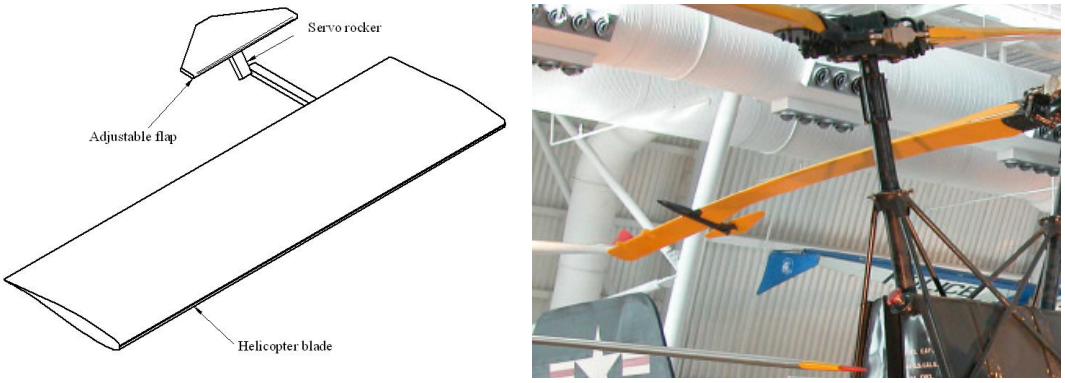

Figure 14 Active servo flaps schematic and application on the K 225 helicopter[48]

3.2.4 Active Plain Trail Edge Flaps

This solution implements either mechanical means[49] or strips of piezoelectric materials fitted to the trailing edge of the blade[50]. The trailing edge moves when the voltage is applied, therefore changing the aerodynamic conditions of the blade very much like a mechanical trailing edge flap would do it for a fixed wing aircraft.

Figure 15 Active plain trail edge flaps on the SMART rotor[54]

3.2.5 Circulation or Boundary Layer Control

This method is based on changing the circulation around the blade to achieve desired aerodynamic characteristics. Compressed air is blown through a series of conveniently located orifices on the airfoil[51]. Thus, pressure around the airfoil changes, generating more or less lift depending on the operating conditions.

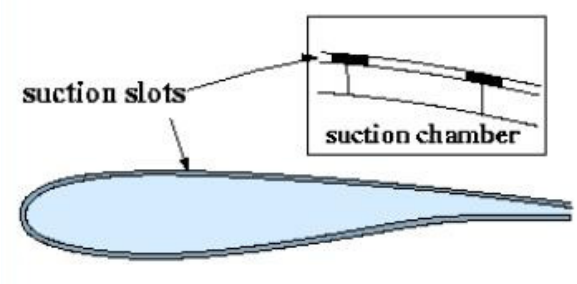

Figure 16 Schematic for boundary layer control[52]

3.2.6 Blade Pitch Control

This approach is based on the usage of hydraulic actuators that vary the angle of attack of the blade, replacing the connecting rods between the swashplate and the pitch horn of the blade by placing rotary hydraulic or electric actuators at the blade root[53].

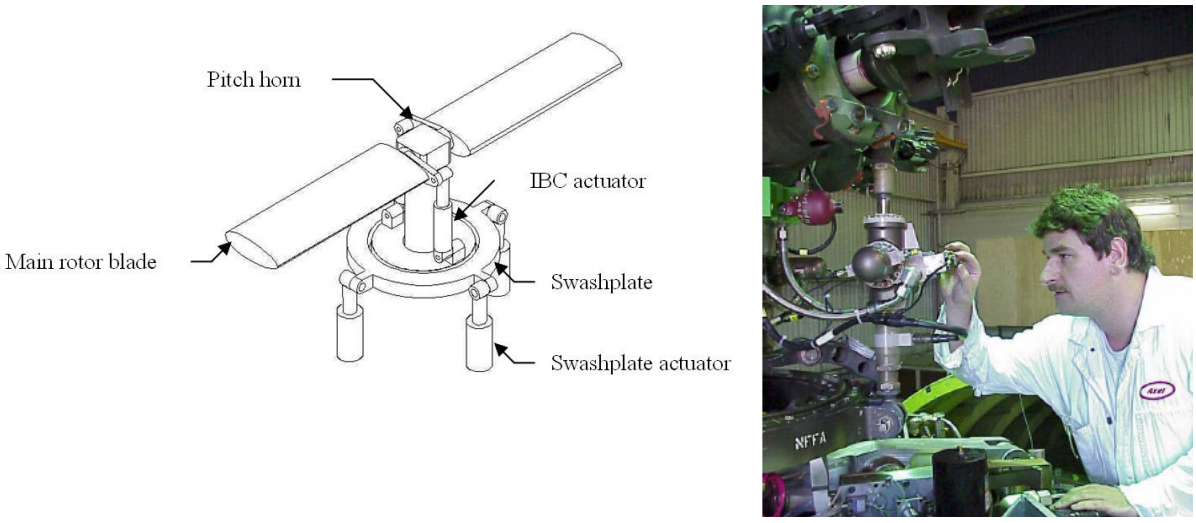

Figure 17 Blade pitch control schematic[21]

Out of the different methods for individual blade control, it was decided to focus on the blade pitch control method. The reason for that was primarily the fact that this technology was tested full-scale, is the focus of sustained current research[54], and appears to be more promising and mature for practical implementation. Additionally, the reliability of hydraulic actuators is greater than the reliability of piezoelectric actuators (given the loads involved) and more likely to ensure a higher level of control redundancy.

For the purpose of this work, different configurations will be analyzed and compared. The first configuration includes the classic swashplate configuration, for single main rotor. The second is an architecture as shown in Figure 17, where the rigid connecting rods of the cklassic swashplate are replaced by hydraulic actuators, generating the pitch angle of the blade as a function of the orientation of the swashplate, the position of the swashplate along the shaft, the azimuth angle and the position of each of the blade actuators. Finally, the third architecture is a full authority individual blade control, also called “swashplateless”. Although a swashplate may stil be present, its orientation does not change, it is just a fixed base for the actuators attached to each of the blades. The motion of the blade is thus dictated solely by the position of the blade pitch actuator. A schematic of this architecture is shown in Figure 18.

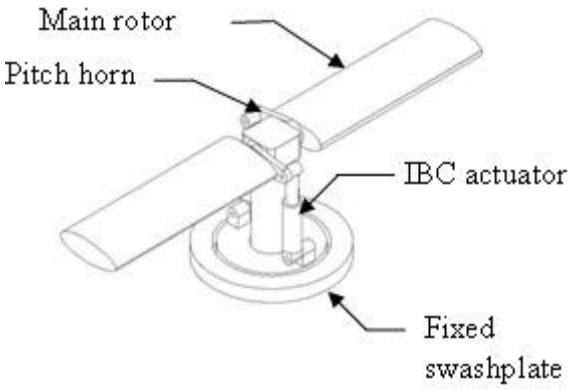

Figure 18 Swashplateless architecture schematic

4 Simulation Environment

A simulation environment was developed[55] for the investigation of the IBC potential for fault tolerance and the design, testing, and analysis of fault tolerant control laws. A detailed description of the simulation is presented next.

4.1 General Architecture of the Simulation Environment

The simulation environment is divided in 3 main modules: Input Module, Output Module, and Simulation Nucleus, as presented in Figure 19.

The input module provides the inputs to the general simulation through appropriate joystick or recorded data and allows the general setup of the simulation scenario and parameters. The joystick control option is used to allow for performance evaluation by an experienced pilot and the pre-recorded input alternative, to ensure repeatability of the tests.

The Simulation Nucleus consists of the following sub-modules:

Failure Module. It consists of the failure models for the actuators, for the three previously defined architectures, the sensors, and the blade structure. The type, magnitude, and moment of occurrence of these abnormal conditions are setup by the user. It affects directly the performance of the main rotor, and in turn, the engine that has to cope with the additional load of the stuck actuator or the missing blade surface. Furthermore, if a sensor in the control feedback loop fails, this will affect the operation of the control laws.

Control Module. This module includes the stability augmentation system and the fault tolerant control laws.

Sum of Forces and Moments / Equations of Motion. This module performs the collection of all forces and moments, reference frames transformation, and the integration of the non-linear dynamic equations.

Helicopter Module. This module include the models of all vehicle components, such as the main rotor, which calculates all the forces and moments that provide control and lift for the helicopter, the fuselage module, the tail rotor, and the vertical and horizontal tail module.

The Output Module gathers the results generated by the simulation and provides the output interface with the user. It is divided into 3 different sub-modules. A visualization environment using Matlab® Virtual Reality Toolbox was developed in order to allow a general view of the motion of the helicopter. A set of output data selected by the user is saved to the

computer disk and time histories of relevant parameters may be monitored during the simulation or generated after.

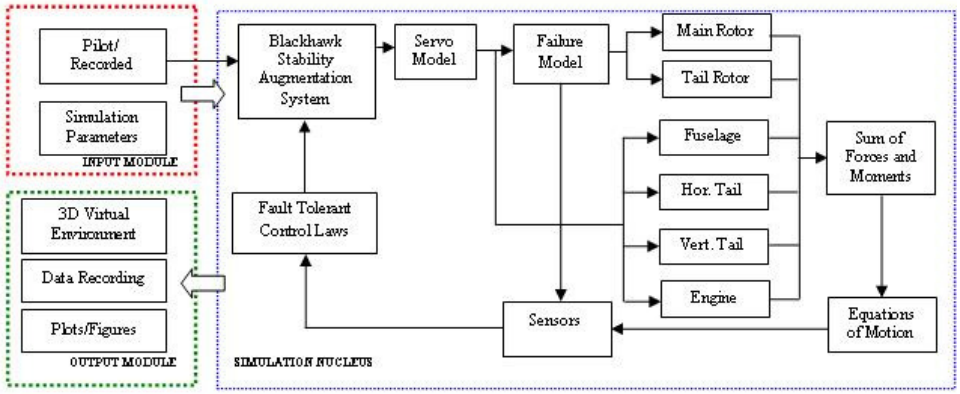

Figure 19 General diagram of the different modules of the simulation environment

The Simulink model follows a similar disposition as the previously described diagram, as shown in Figure 20, with the inputs on the left, the different modules (control, in light blue; main rotor, in yellow; empennage, in bright green; fuselage, in dark green; turbulence, in light blue; and motion , in red), and the outputs on the right, with the virtual reality module and the different scopes for the different variables of interest.

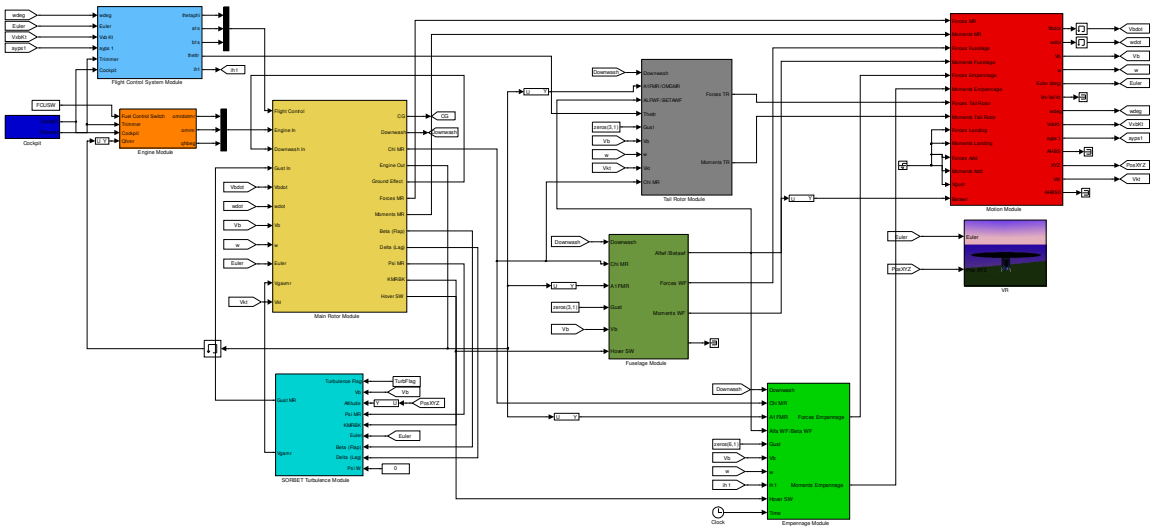

Figure 20 Simulink diagram for the simulator

The main rotor subsystem, as shown in Figure 21, includes the calculations for the main rotor and it includes the failure models for the swashplate and the individual blade actuators. This model includes two level 2 S-functions to calculate for the main rotor forces and moments (shown in yellow), which are divided by the IBC failure module (shown in blue), which is activated according to the user. Furthermore, it includes the ground effect module (shown in

orange) and an additional filter to compensate for numerical issues for the output forces and moments (shown in dark green). Additionally, the swashplate actuator failure (shown in light green) is located between the SAS and the first S-function, since it directly affects the orientation of the whole disk.

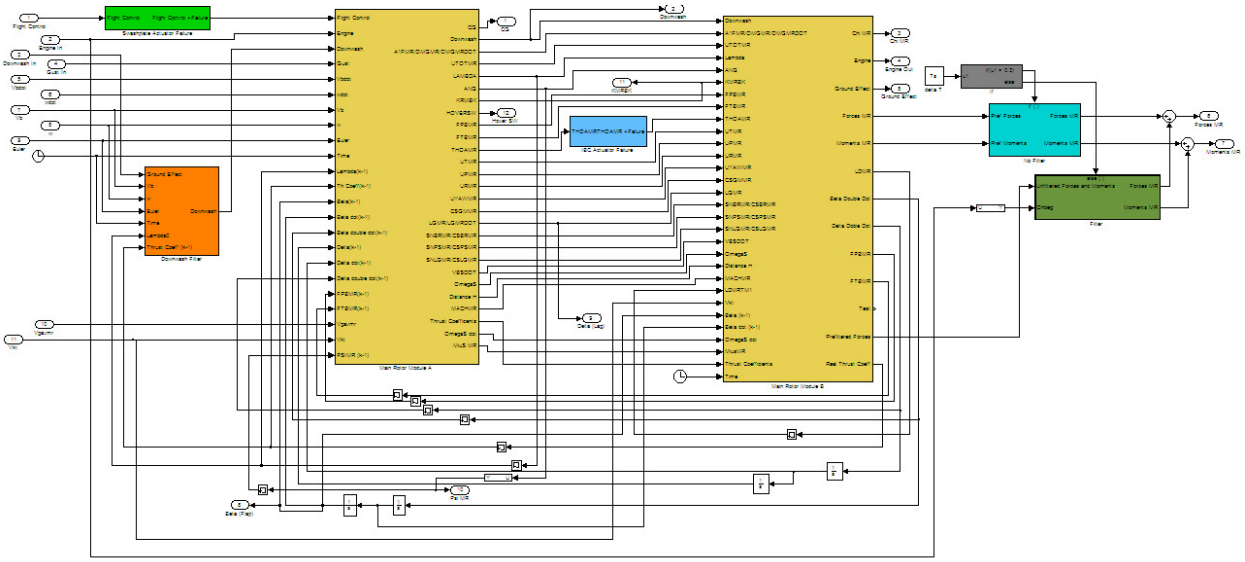

Figure 21 Main rotor Simulink model

The control or stability augmentation system is shown in Figure 22. The sensor failure modules, affecting all three gyros and the lateral accelerometer are included and shown in yellow. The helicopter's Stability Augmentation System (SAS), is shown in orange, affecting the lateral, longitudinal and tail rotor collective controls. The pitch bias actuator is shown in light blue under the SAS, affecting the longitudinal control system. The FPS channel for the lateral, longitudinal and tail rotor control are shown in green, affecting their corresponding control systems. The collective control, only affected by the pilot input, is shown in brown. The stabilator control is shown in light purple, used to control the pitch angle of the aforesaid control surface. Finally, the modules for the lateral, longitudinal and tail rotor collective are shown in red, cyan and gray respectively. The outputs of these modules directly affect the orientation of the swashplate and tail rotor blade pitch. All the outputs are constrained to physical dimensions and geometry to prevent outputs that would not match the actual motion of the actuators.

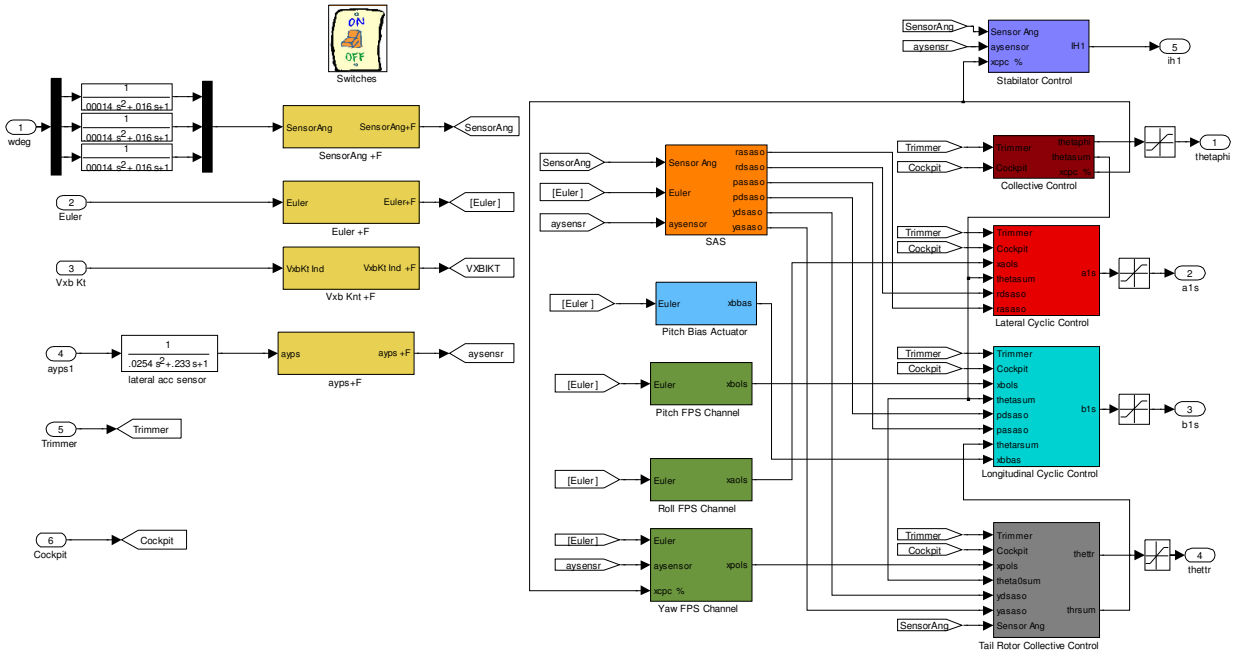

Figure 22 Helicopter control and stability augmentation system

4.2 Helicopter Control Architectures

The architectures considered for this study include:

- Classic swashplate configuration for single main rotor.
- Classic swashplate fitted with individual blade control pitch blade actuators.
- A full authority individual blade control system operated solely by blade pitch actuators.

This testing arrangement was selected given that a comparison with the existent technologies and IBC is required in order to show the improvements in fault tolerance for this novel and emerging technology.

In the case of the classic swashplate architecture, inputs from the pilot are collected for the lateral and longitudinal cyclic, collective and pedals, then those inputs are filtered through the Blackhawk SAS system, and then transferred to the tail rotor collective, and swashplate actuators, and finally the latter generates a mechanical mixing that results in the definitive angle of each of the main rotor blades.

Since more work has been done over the second architecture, with a full scale model flown and positive results for vibration and cockpit noise attenuation, this setup was the more natural choice to first evaluating the improvement in flight safety. Besides it proves to be the intermediate step between a full authority IBC and the classic swashplate setup. In this case, the

pilot inputs are assembled and filtered in the exact same way as in the classic configuration, only that an additional input after the swashplate mechanical mixing is added by the inclusion of the IBC actuators, which can increase or decrease the blade pitch angle depending on the flying conditions. If the flying conditions are healthy (without failure) this input can be used to decrease the main rotor vibrations and cockpit noise attenuation, in case of failure, this input will be used to operate the blade pitch angle such that nominal or close to nominal conditions of the general behavior of the helicopter are obtained. It is to be noted that vibration alleviation is beyond the scope of this research, thus in nominal conditions the IBC input is set to zero.

Finally, a swashplateless architecture will be analyzed to assess its potential as the final phase in the full implementation of this novel technology. In this case, the inputs are collected in the same way as in the previous architectures to prevent that new training is required for pilots and establish a good comparison with the other architectures. These inputs are then filtered through the same Blackhawk stability augmentation system and then instead of using a mechanical mix as the previous configurations, a virtual one is used. This "virtual swashplate", implemented via software, combines the inputs of the lateral and longitudinal cyclic and the collective to obtain the equivalent blade pitch angle for a conventional approach, and then the vibration alleviation input can be added (if the system is healthy) or a reconfiguration input (if the system is under failure). As was the case with the previous architecture, the vibration alleviation and cockpit noise reduction use of the IBC is beyond the scope of this work, and will not be analyzed nor implemented.

4.3 Simulation Scenarios and Graphic User Interface

The simulation environment is based on the Matlab® and Simulink® computational packages. A series of graphical user interface (GUI) menus allow for the simulation scenario setup as described next.

Main Menu. This is the portal to the simulation environment (Figure 23). It allows the selection of the specific helicopter model to be analyzed. Several models are implemented. The Blackhawk (presented in this dissertation), an equivalent linear model of the Blackhawk helicopter, and the Bergen Industrial Twin (for future UAV analysis) are available. Different simulation scenarios can be chosen depending on the characteristics of the analysis, such as hover and forward flight (for which the forward flight speed can be selected). Furthermore,

nominal conditions or failure conditions can be selected affecting actuators, sensors, or the structure of the blade

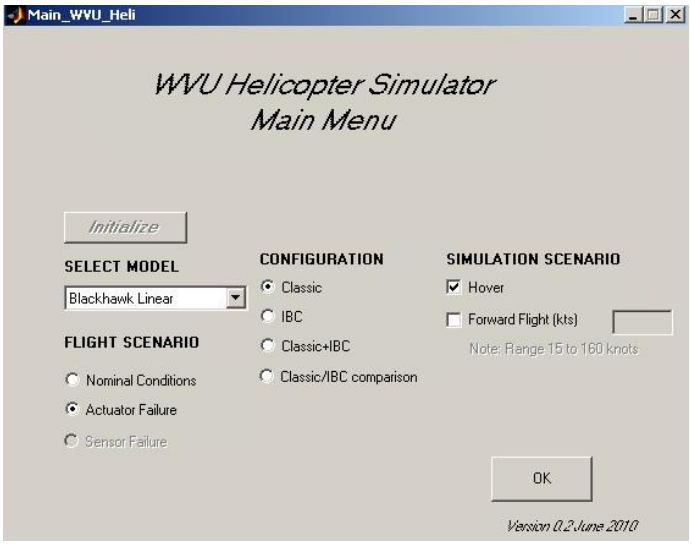

Figure 23 Main menu for general simulation conditions

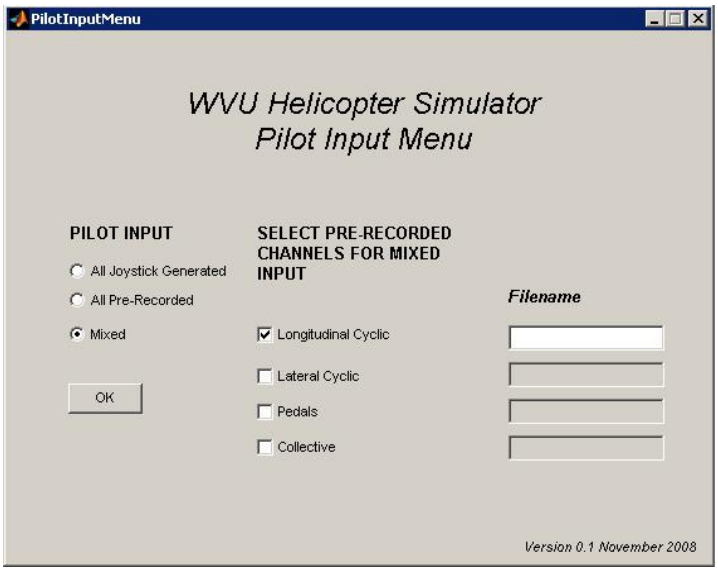

Figure 24 Interface for pilot input selection

Pilot Input Menu. The pilot input can be selected to be produced interactively from a joystick, or from a pre-recorded file or mixed. The pre-recorded option allows for repeatability given a set of conditions and to test the performance of a given control scheme when the input is the same. The panel can be seen in Figure 24.

Failure Menu. This panel determines the failure scenario that will be applied to the helicopter. Actuator failure, surface failure and a mix of both can be chosen from a list-box. If an actuator is chosen, several different parameters must be defined, such as the conditions

(locked at imposed or current deflection), the actuator that will fail (which can be either a swashplate or an IBC actuator), the simulation time at which the failure will occur and in case that a specific deflection is chosen, the parameters for the imposed deflection and time constant must be specified. If a missing surface is chosen, parameters such as the location of the missing surface (by specifying the r/R value) and the blade that will suffer the failure, must be specified. Furthermore, weather conditions such as wind shear and turbulence models can be added in order to evaluate the failure under different weather conditions. A snapshot of the menu can be seen in Figure 25.

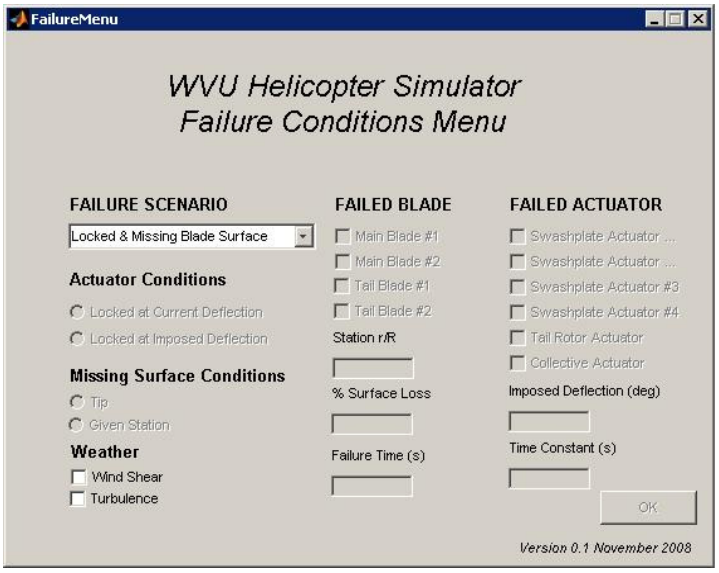

Figure 25 Failure scenario setup menu

Figure 26 Virtual reality interface

Once all the parameters are specified, the simulation loads an additional window to select different plots for real time analysis of the different state variables. In order to allow for first

glance evaluation of the behavior of the helicopter, a virtual world with the helicopter was built using Matlab® Virtual Reality Toolbox (Figure 26).

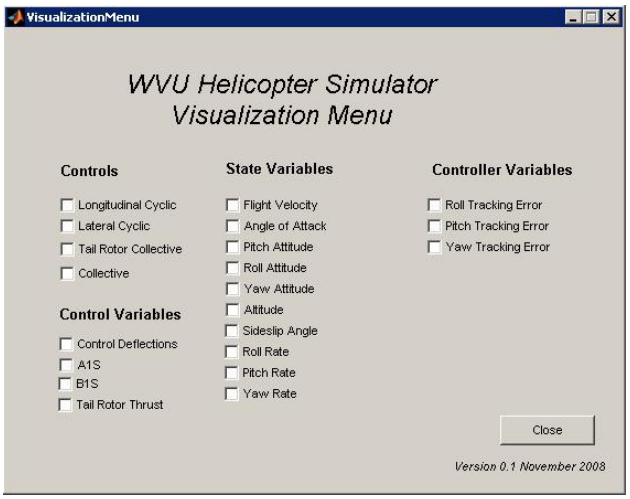

Figure 27 Graph selection menu

For performance evaluation, a GUI is generated so different variables can be selected and perform the constitutive analysis. An example of this GUI is shown in Figure 27.

4.4 Simulation Examples

A forward flight condition at 20 ft/s was considered for the simulation examples and results presented next. Figure 28 through Figure 35 show some of the most important parameters at nominal conditions. This test is carried out in open loop, using only the stability augmentation system of the helicopter to illustrate the general operation of the simulation model. Step pilot control input at the initial moment is provided. After a transition of approximately 80 seconds, the aircraft reaches a steady state.

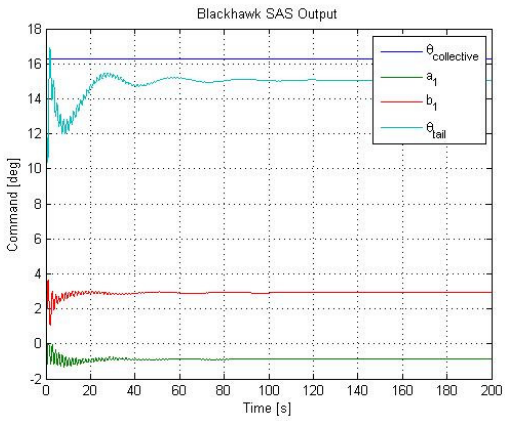

Figure 28 Blackhawk SAS output for forward flight

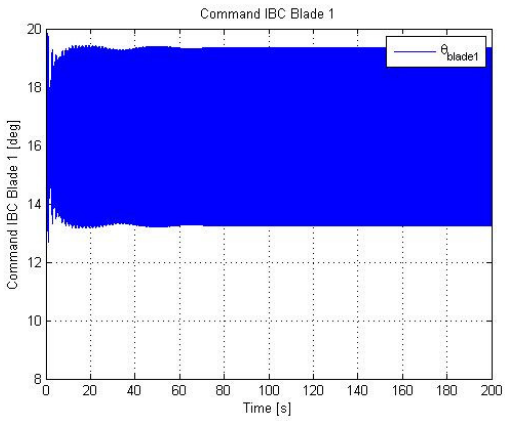

Figure 29 Blade pitch angle for blade #1

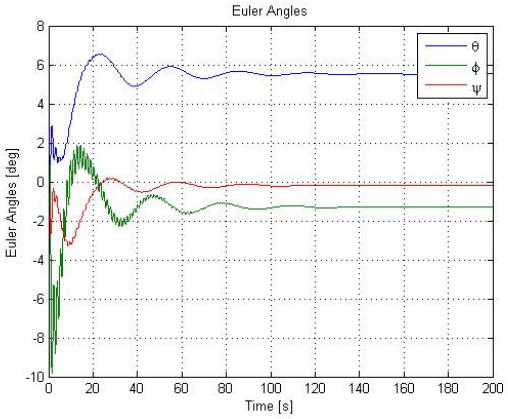

Figure 30 Helicopter Euler angles

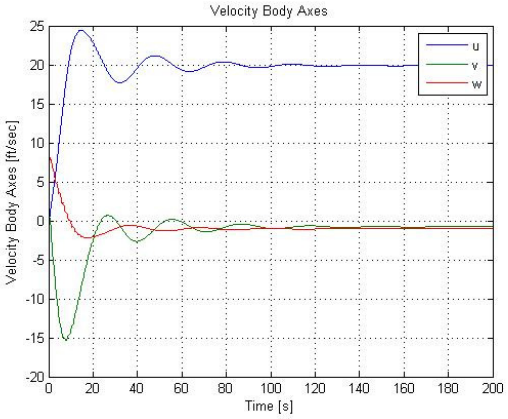

Figure 31 Helicopter linear velocity in body axis

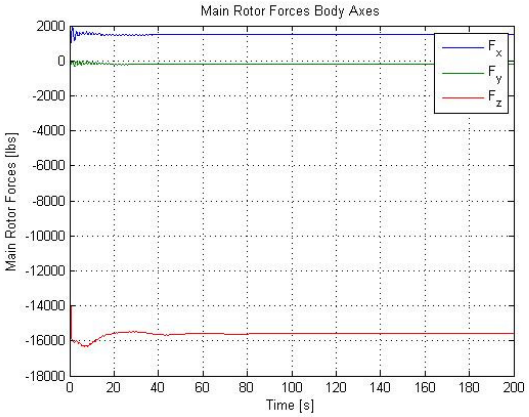

Figure 32 Main rotor forces in body axis

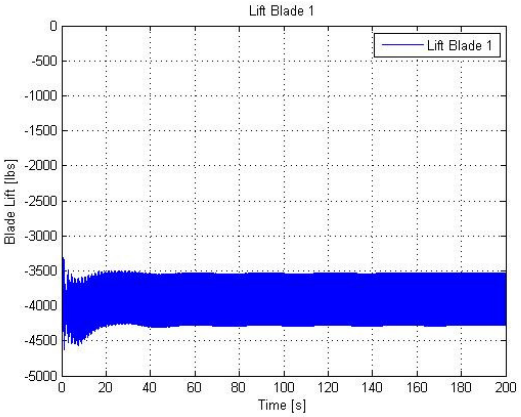

Figure 33 Lift generated by Blade#1

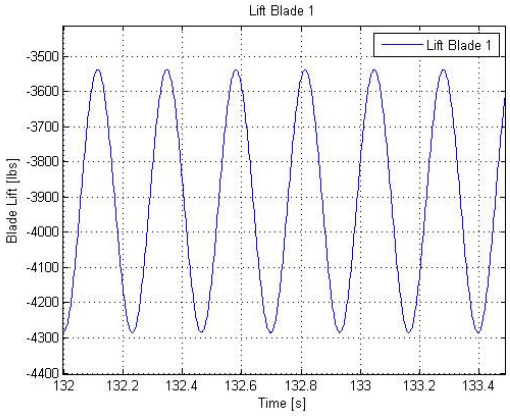

Figure 34 Lift generated by blade #1 (zoom)

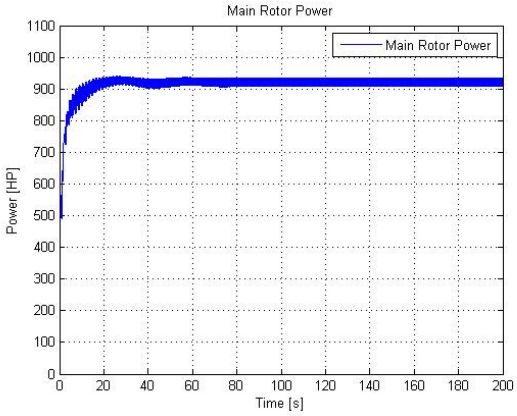

Figure 35 Main rotor power

Steady state conditions for the attitude of the helicopter can be determined in Figure 30, for which the helicopter has a steady state pitch angle close to 5.8 deg, which means a nose up condition, it is to be cleared that sometimes this behavior can occur in forward flight, given that the orientation of the main rotor is the one that provides for the forward force. Additionally, this behavior is reinforced by the fact that the main rotor is tilted with respect to the waterline of the

helicopter by a magnitude of 7 degrees. Furthermore, when analyzing the values of the roll angle, a value of around -1.7 deg is reached for the steady state condition. This is caused by the need to compensate, with the main rotor, the side force generated by the tail rotor and keep the helicopter flying close to a straight line.

On the other hand for the speed, as had been stated before, a value of u equal to 20 ft/s is reached as a steady state condition for the forward flight, and although there are nonzero values for v and w, as can be seen in Figure 31, these values cause a minor sideslip but are not so determinant to affect the forward flight condition.

Given that the weight of the helicopter is 16638 lbs, the average of the lift force generated by blade #1 is approximately 3900 lbs, as shown in Figure 34, the sign is attributed to the fact that the axis are located such that the z axes is pointing downwards in body axis, causing the weight to be positive. The frequency at which the lift varies, which can be seen in Figure 34, is the same as the main rotor angular velocity (4.3 Hz). Furthermore, additional lift is produced by the fuselage, a horizontal control surface located close to the tail rotor and the tail rotor itself. The latter one has an angle of 70 degrees with respect to the vertical plane thus, generating not only a side force for to compensate for the main rotor torque but also a lift force. From Figure 35 it can be seen that for the steady state conditions, a power consumption of around 920 hp is required by the main rotor. This value does not include the losses by the gearbox nor the tail rotor, but given that each engine for a Blackhawk is rated at 1890 hp, it can be assumed that, qualitatively, the simulation closely matches the real counterpart.

A swashplate failure is simulated and presented next. A failure of the lateral cyclic – locked at -2 degrees - was injected at 120 seconds after any initial transient effects have vanished. The failure can be identified as a first order transition between the steady state value and the final value for the plot of the main rotor command in Figure 36. Although the Blackhawk architecture includes one actuator on each side of the swashplate to obtain the lateral tilt of the swashplate, in this example it was considered that both actuators are locked at the same time, given that a locked actuator on one side and a fully functional on the other would require a substantial gap between the swashplate and the shaft to keep on moving the swashplate. The failure was introduced using a time constant of 1 second. The effects of this failure on the main dynamic variables of the helicopter are presented in Figure 36 through Figure 39. The lateral cyclic failure exhibits an immediate effect on the Euler angles, as can be seen in Figure 38,

where it is clear that within a couple of seconds of the failure, the roll angle goes slowly out of control, within the first 5 seconds, with a angular rate close to 14 deg/s. The stability augmentation system tries to compensate this effect by decreasing the tail rotor collective, given that by the position of the tail rotor, above the location of the main rotor, it produces a moment around the x axis of the aircraft. However, compensation is effective only for a limited interval of time, until the tail rotor collective actuator saturates (Figure 36), once this happens, the other euler angles (θ and ψ) start to oscillate in an unstable manner. In a similar way the velocity of the helicopter changes too once the failure is introduced, although in this case, v and w have a more immediate effect than on u, caused by the action of the tail rotor as described before. The control of the helicopter by a human pilot, after this swashplate actuator failure, appears to be very difficult if at all possible.

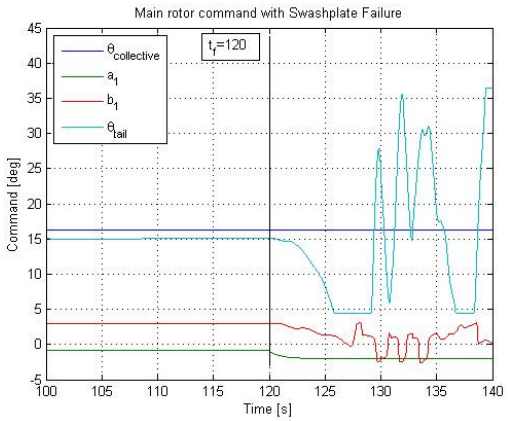

Figure 36 Command with swashplate failure

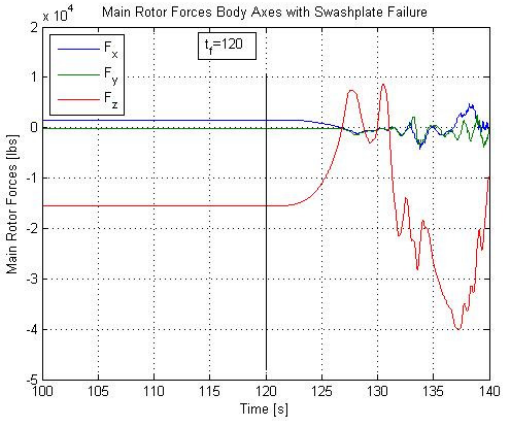

Figure 37 Main rotor forces with swashplate failure

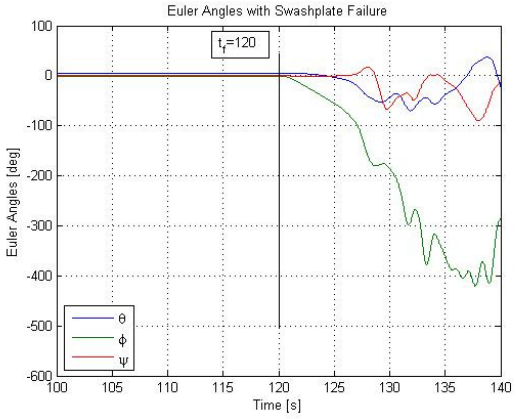

Figure 38 Euler angles with swashplate failure

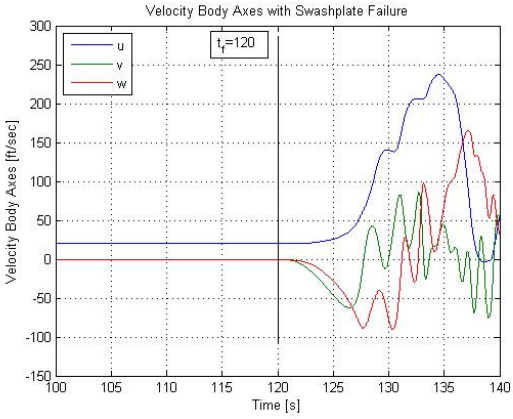

Figure 39 Velocity with swashplate failure

A failure of one actuator of the IBC configuration is analyzed next. The failure is injected at t = 120 s and consists of locking the blade pitch angle of blade #1 at 18.5 degrees

(Figure 40). Note that the behavior of any of the four blades is equivalent. The variations of the main dynamic variables for this failure scenario are presented in Figure 40 through Figure 45. The failed blade pitch angle is larger than the average in normal operation; therefore, the total lift produced increases as shown in Figure 41. The Euler angles are perturbed (Figure 42); however, the general stability of the system is preserved, as can be determined by the attenuating oscillations on Figure 42 and Figure 43. The additional lift produces a motion upwards and a decrease of the forward velocity (Figure 43). The non-symmetry induced by the failed blade produces substantial oscillations of the main rotor forces and moments as shown in Figure 44 and Figure 45, the structural consequences of the lack of balance is not evaluated. It can be seen that, in this failure scenario, the dynamic effects on the system are less dramatic and the SAS can maintain stable flight. However, it should be noted that for a valid analysis and a comparison of the two configurations, failures of similar severity from all points of view must be considered.

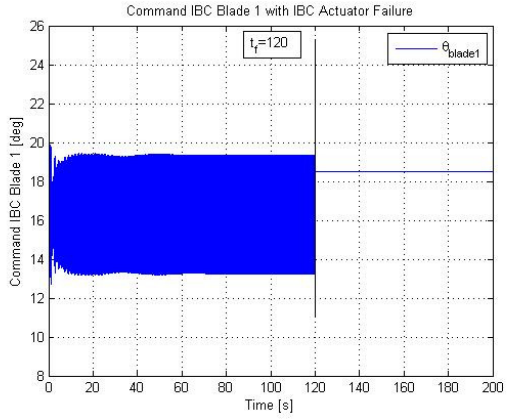

Figure 40 IBC command with actuator failure

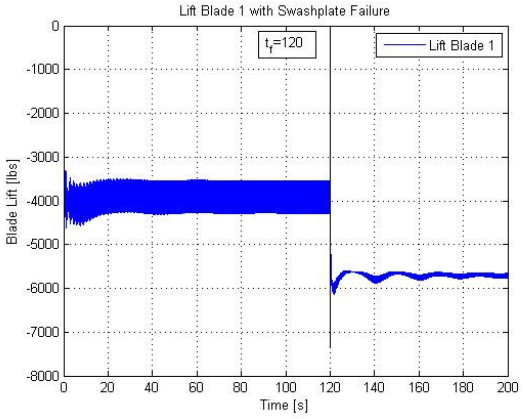

Figure 41 Lift produced by blade #1

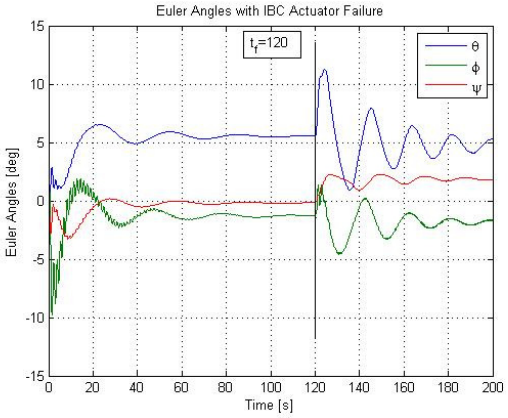

Figure 42 Euler angles with IBC actuator failure

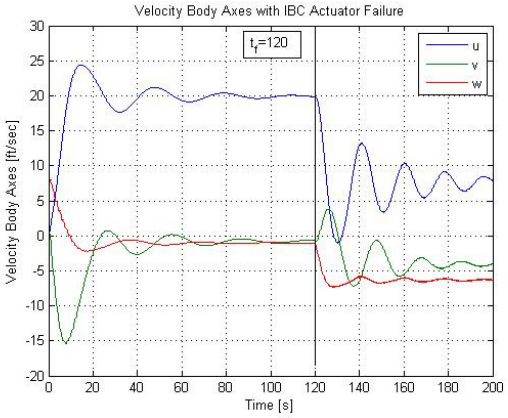

Figure 43 Velocity with IBC actuator failure

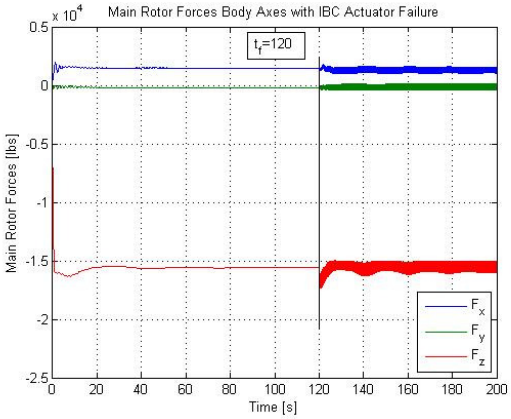

Figure 44 Main rotor forces with IBC failure

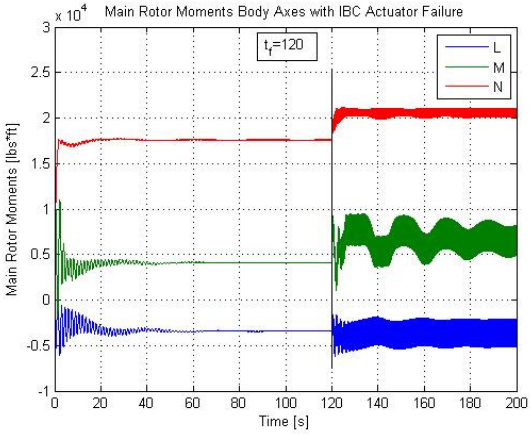

Figure 45 Main rotor moments with IBC failure

4.5 Model Comparison

Even though the validation with flight test data for the full individual blade controlled helicopter can not be possible since the actual helicopter, with the specifications for the IBC actuators does not exist, a quantitative analysis can be performed using the available data for validation of the UH60 Blackhawk helicopter in its classic swashplate configuration. Validation data for the specific weight, center of gravity, inertias, etc., of the helicopter presented in this work was not found, however, linear models for the same helicopter in different configuration were found, in the work by Takahashi[56]. This model, was linearized around a flight condition of 1 knot in forward flight, is shown in equation (197). The states for this particular model are shown in equation (198) and represented as the model F_T.

$$F_T = \begin{bmatrix} -0.021 & 0.0123 & 2.0151 & -32.0656 & -0.0132 & -1.2081 & -0.0365 & -0.2816 \\ 0.0005 & -0.2356 & 1.9317 & -1.4828 & -0.0005 & -0.0977 & 1.6168 & 2.2755 \\ 0.0038 & 0.0011 & -0.9094 & 0 & 0.0067 & 0.1532 & 0.0130 & -0.0185 \\ 0 & 0 & 0.9987 & 0 & 0 & 0 & 0 & 0.0505 \\ 0.0048 & 0 & -0.8659 & 0.075 & -0.0207 & -0.2552 & 32.0278 & -1.3799 \\ 0.0368 & 0.0023 & -1.6579 & 0 & -0.0312 & -5.7728 & 0.0455 & 0.1431 \\ 0 & 0 & -0.0023 & 0 & 0 & 1 & 0 & 0.0462 \\ 0.0006 & 0 & -0.1125 & 0 & 0.0041 & -0.0368 & 0.001 & -0.2238 \end{bmatrix} \quad \textbf{(197)}$$

$$x = \begin{bmatrix} u & w & q & \theta & v & p & \phi & r \end{bmatrix}^T \quad \textbf{(198)}$$

Since the nature of the simulation environment is nonlinear, a linearization process was conducted for the hover conditions[57]. The linearization process consisted in freezing both the control and the body states integrators, and each of the states was disturbed with a normalized excitation. The accelerations for each state were measured and using a numerical differentiation

process, each of the derivatives was calculated. The result of this differentiation process can be observed in equation (199) and represented as the model F_M.

$$F_M = \begin{bmatrix} -0.012 & 0.021 & 1.56 & -32.03 & 0.001 & -1.17 & -8.36e-7 & -0.32 \\ 0.0312 & -0.29 & 0.2123 & -3.2 & -0.0064 & -0.33 & 0.42 & 1.98 \\ 0.0032 & 0.002 & -0.53 & 0 & 0.0016 & 0.19 & -4.69e-9 & -0.06 \\ 0 & 0 & 0.99 & 0 & 0 & 0 & 0 & 0.02 \\ -0.0039 & 0.0003 & -0.747 & 0.0866 & -0.022 & -0.65 & 32.07 & 0.34 \\ 0.0003 & -0.0002 & -1.403 & 0 & -0.187 & -3.42 & 1.17e-10 & -0.06 \\ 0 & 0 & -0.0023 & 0 & 0 & 1 & -9.76e-8 & 0.086 \\ 0.0017 & -0.003 & -0.147 & 0 & 0.005 & -0.1911 & 9.11e-12 & -0.191 \end{bmatrix} \quad \textbf{(199)}$$

As can be observed, there are some differences between the two models; therefore, in order to make a more proper assessment of the differences in the dynamic response of the helicopter, a modal analysis of both models was carried out by calculating the eigenvalues of the state matrices. These eigenvalues are shown in Table 3. Values for the physical properties of both helicopters are shown in Table 4.

Table 3 Eigenvalues for the model used and the model found in the literature

Dynamics	Eigenvalues F_M	Eigenvalues F_T	ζ_M	ωn_M	τ_M	ζ_T	ωn_T	τ_T
Longitudinal	-0.8367	-1.1611	N/A	N/A	1.2 s	N/A	N/A	1.2 s
	0.0665+0.35i	0.2137+0.41i	1.05	0.06	N/A	1.07	0.19	N/A
	0.0665-0.35i	0.2137-0.41i	1.05	0.06	N/A	1.07	0.19	N/A
Long/Lat	-0.2087+0.018i	-0.2183+0.025i	1.01	0.21	N/A	1.01	0.21	N/A
Lateral	-3.3805	-5.74	N/A	N/A	0.29 s	N/A	N/A	0.17s
	0.0117+0.42i	-0.1332+0.49i	1.08	0.01	N/A	1.11	0.11	N/A
	0.0117-0.42i	-0.1332-0.49i	1.08	0.01	N/A	1.11	0.11	N/A
Lat/Long	-0.2097-0.018i	-0.2183-0.025i	1.01	0.21	N/A	1.01	0.21	N/A

Table 4 Model configuration properties for UH60

Properties	F_M	F_T
Mass [lb]	16638	15007
Ixx [slug/ft^2]	4659	5629
Iyy [slug/ft^2]	38512	40000
Izz [slug/ft^2]	36796	40000
Ixz [slug/ft^2]	1882	1670

As it can be observed in Table 3, the disposition of the longitudinal eigenvalues of the model described in this work matches in stability and in frequency with the model described by Takahashi in his work, with a few discrepancies in the real part. With unstable phugoid modes and slow decoupled heave mode.

For the lateral dynamics, it can be seen that the eigenvalues differ in stability for the dutch roll. This can be attributed to the differences already stated in Table 4 for the differences in

the configuration used for each model. In certain occasions this mode can be unstable, as can be seen in Figure 46, where the location of the poles for a linearized model of a Puma helicopter are shown. Even though the Puma is a smaller helicopter with different characteristics, it can be used as a benchmark for the location of the poles. Furthermore, in the case of the Takahashi model, the center of gravity is not specified in the properties. This is a crucial value that can affect the dynamics dramatically.

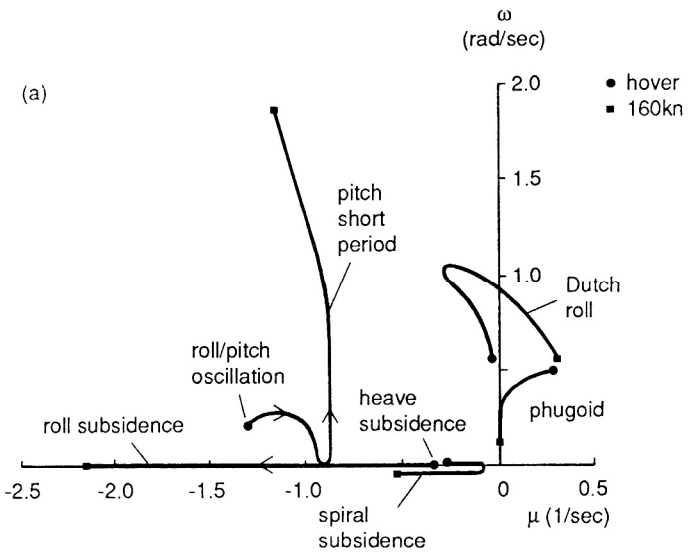

Figure 46 Loci of Puma helicopter eigenvalues[58]

Analysis of the trim conditions for hover were performed, showing small differences, as it is to be expected, given the contrast between the helicopter physical configurations. For the Takahashi model, the pitch and roll Euler angles in hover are around 2 degrees and -3 degrees respectively (estimated from Figure 47). As for the model proposed in this dissertation, values are 4 degrees for the pitch and -1.5 for the roll. Again these differences can be accounted not only to the different configurations but also to the characteristics of the atmosphere at which both models were calculated.

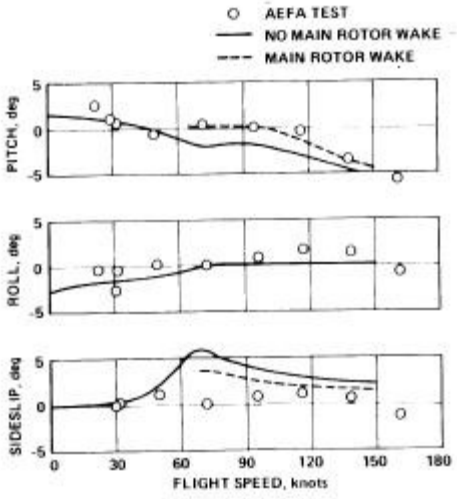

Figure 47 Trim conditions for UH60[56]

Additional trim values for several forward flight conditions were found and are shown in Figure 48 and Figure 49. As can be seen the performance of the helicopter is very similar for the roll attitude angle, however, the pitch has a small difference, due to the differences in the helicopter weight distribution and general inertias. Furthermore, key control factors such as the position of the pitch bias actuator in the data gathered in the paper by Takahashi, are not explained. The pitch bias actuator compensates for the longitudinal orientation of the swashplate for a certain range of forward speeds, increasing the pitch attitude angle as forward speeds increase.

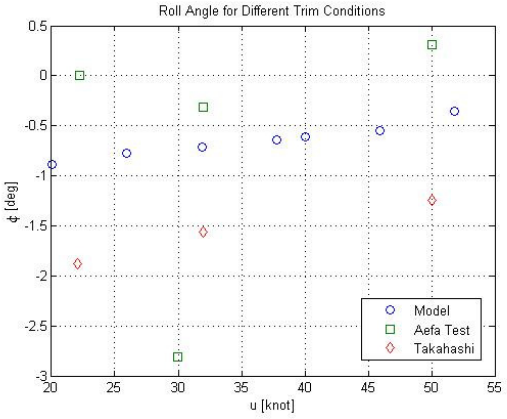

Figure 48 Roll angle in trim for several flight conditions

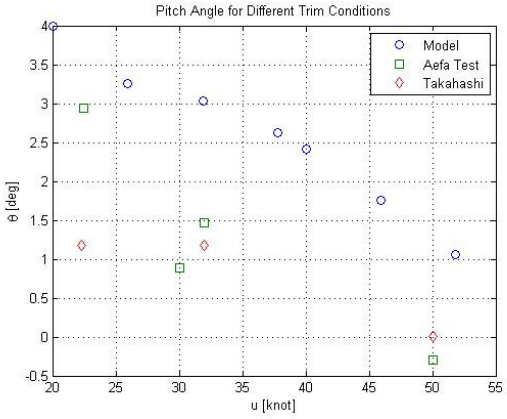

Figure 49 Pitch angle in trim for several flight conditions

5 Fault Tolerant Controller Design

It has been shown that nonlinear dynamic inversion with the addition of neural networks is an excellent tool for adaptive control of highly nonlinear systems[59]. This technique, in general, is based on the principle of a direct linear inversion of the plant for a given operation point, and the addition of an adaptive input - for example generated by a set of neural networks - to compensate for the errors generated by modeling uncertainties, linearization, and abnormal subsystem operation. This architecture allows not only for stabilization and control of the nonlinear plant in nominal conditions, but it has also been proven as an option for those models for which fault tolerant capabilities are required[2,60]. Furthermore, the application of this technique for helicopters has already been proven to perform attitude stabilization and trajectory tracking. In this case, Leitner et al[61], created separate adaptive inputs, each with its own neural network to stabilize the angular rates of the helicopter, thus providing stability to the helicopter's attitude.

With regards to actuator failure, Drozeski[5] implemented the same architecture using an additional output to control the helicopter's rotor angular speed to compensate for the loss of maneuverability. In that effort, a conventional swashplate configuration with 3 actuators was used as a testing platform for the NLDI+NN architecture. At nominal conditions, the main rotor speed is set to a particular value and only the blade pitch angle is changed, to increment the average lift generated by the main rotor. Thus, the inclusion of this additional degree of freedom proved to be useful to obtain the positive results, however given the rotary nature of the lift, an increase of the airspeed will increase the chances of the blade to hit transonic or even supersonic aerodynamic behavior at the blade tip, generating not only vibrations but also possible blade delamination, decreasing then the helicopter's health even more. Thus, the range of operation for which the throttle can be used as a valid input, is quite small in comparison with other techniques such as individual blade control, as it will be discussed later. Furthermore, in his work, Drozeski[5] used actuator stuck values close to the hover position, which allowed not only to relieve the stress over the throttle operation, but also not risking a force imbalance or tendency of the helicopter to turn in a certain direction. Another issue that should be taken into account is the fact that the swashplate configuration used for these tests included only 3 actuators, which still allowed for some swashplate motion even if one of the actuators got stuck. As a consequence,

the others two health actuators can partially compensate the failure effects (as in the work by Enns et al[6]); however, this configuration is not very common in commercial nor military helicopters.

5.1 Actuator Failure Analysis

Since the objective of this research is to accommodate actuator failures for an individual blade control helicopter, an analysis of the repercussions of such failure on the dynamics of the vehicle is necessary for a successful controller design. Firstly, a helicopter with classic swashplate architecture will be discussed, then a classic swashplate fitted with individual blade control actuators, and finally, a swashplateless architecture will be analyzed.

5.1.1 Classic Swashplate Architecture

This architecture, based on the single main rotor, has been investigated over the years, and considering the highly nonlinear behavior, coupling of the control surfaces, and lack of degrees of freedom for the same surfaces, results -where in some cases stability is obtained for a particular set of flying and failure conditions- have been shown relative success given the circumstances[6]. The Blackhawk nominal configuration includes 4 swashplate actuators, two for each channel, longitudinal and lateral. For instance, if the pilot wants to tilt or move the vehicle laterally, to the right, he/she will have to move the stick to the right and this will cause that the two lateral actuators work at unison (one moving upwards, and the other downwards) on both sides (left and right) of the main rotor shaft, tilting the swashplate assembly to the right. In a similar way. a tilt or move on the longitudinal channel can be commanded and executed. The two longitudinal actuators will move the swashplate and cause the helicopter to tilt in the same way. However, if one of these actuators locks up, then the other will be instantly disabled given the tight fit of the swashplate around the shaft. Thus, preventing the swashplate to tilt in the desired direction and removing the ability of the pilot to go forwards-backwards or side to side as in nominal conditions. Simulated results of the actuator failure have been shown in this dissertation in section 4.4, demonstrating the catastrophic reaction of the helicopter to a swashplate actuator failure.

5.1.2 Swashplate and IBC Architecture

In this case, research has been performed in a general way[25], by analyzing failures of IBC actuators by affecting the efficiency of each of the contributions of the collective, lateral and longitudinal cyclic, but no work on a specific technology for individual blade control has been found up until the development of this research. Thus, a specific architecture, using blade pitch actuators has been chosen and the effects of actuator failure will be discussed[62].

For nominal conditions the geometric blade pitch angle will be as follows:

$$\theta_i = \theta_0 - A_1 \cos\psi_i - B_1 \sin\psi_i + \theta ft_i \quad \text{with } i = 1..N_{BS} \tag{200}$$

$$\theta ft = \theta_{noise} + \theta_{vibration} + \theta_{failure} \tag{201}$$

Terms describing the change of the blade pitch due to flapping and aerodynamic loads are neglected for simplicity. The term describing the IBC is included as θft is composed of three terms, as shown in equation (201). These terms account for vibration alleviation, noise reduction and failure. The first two terms can help to improve the performance of the helicopter in nominal conditions by reducing vibration and cockpit noise, but are not the objective of this research and will be neglected. The term remaining term will be used in this research to account for failures in the helicopter, hence in nominal conditions it has no purpose, and its value is zero. Thus, it can be interpreted that with θft=0, the equation can be rewritten as:

$$\theta_{i_{nom}} = \theta_{0_{nom}} - A_{1_{nom}} \cos\psi_i - B_{1_{nom}} \sin\psi_i \quad \text{with } i = 1..N_{BS} \tag{202}$$

In case of a swashplate actuator failure, it will be assumed that the actuator will be stuck in a specific position and there will be no change in this position as time increases. Furthermore, given that the swashplate configuration for the Blackhawk includes 4 actuators (2 for each channel, lateral and longitudinal), it will be assumed that if one of the channels, longitudinal or lateral, is affected by the failure, its accompanying actuator will not be able to change the orientation of the swashplate. Unfortunately the gap between the main rotor shaft and the swashplate is very small, thus impeding the upward motion of the accompanying actuator, if one gets stuck.

Since the objective of this research is to obtain nominal conditions in case of actuator failure through helicopter control reconfiguration, equation (203) can be used to find the values of θ_{ft} for which the nominal conditions can be preserved. For example, for a lateral swashplate actuator failure:

$$\theta_{i_{fail}} = \theta_{0_{nom}} - A_{1_{fail}} \cos\psi_i - B_{1_{nom}} \sin\psi_i + \theta ft_i \quad \textbf{(203)}$$

$$\theta_{i_{fail}} = \theta_{i_{nom}} \quad \textbf{(204)}$$

$$\theta_{0_{nom}} - A_{1_{fail}} \cos\psi_i - B_{1_{nom}} \sin\psi_i + \theta ft_i = \theta_{0_{nom}} - A_{1_{nom}} \cos\psi_i - B_{1_{nom}} \sin\psi_i \quad \textbf{(205)}$$

$$\theta ft_i = \left(A_{1_{fail}} - A_{1_{nom}} \right) \cos\psi_i \quad \textbf{(206)}$$

In a similar way, the values for the individual blade control of the blade if the affected actuator is the longitudinal channel, as described in equation (207).

$$\theta ft_i = \left(B_{1_{fail}} - B_{1_{nom}} \right) \sin\psi_i \quad \textbf{(207)}$$

If both the swashplate's lateral and longitudinal actuators suffer failure, the individual blade control can still perform corrections so that the performance under failure can be as similar to nominal conditions, as can be shown in equation (208).

$$\theta ft_i = \left(A_{1_{fail}} - A_{1_{nom}} \right) \cos\psi_i + \left(B_{1_{fail}} - B_{1_{nom}} \right) \sin\psi_i \quad \textbf{(208)}$$

In all cases, it is assumed that the range of action of the individual blade control actuators is large enough to reach the required extentions.

5.1.2.1 Sensitivity Analysis

From the previous analysis it is clear that a fault detection and evaluation scheme is required for a successful failure accommodation through individual blade control with this configuration, since not only an appropriate detection of the failure in time is required but also the deflection of the swashplate under failure conditions. A failure detection and evaluation scheme is typically affected by a detection delay, an evaluation delay, and an evaluation bias. Hence, a sensitivity analysis was carried out to evaluate the impact of both the total time delay (between the actual occurrence of the failure and the time when the fault tolerant controller starts to operate, which is assumed to coincide with the moment of failure evaluation) and swashplate deflection evaluation/measurement bias under failure conditions. Analysis values for the swashplate bias were set to 0 degrees (no bias), 0.2, 0.5 and 1 degree, and time delays were set form 0 to 6 seconds in one second increments and 10 seconds. This analysis using the Blackhawk's stability augmentation system and the IBC controller, in order to provide a baseline of the helicopter towards failure.

A simulation example, using the control technique described in the previous section is shown as follows. In this case, a lateral swashplate actuator failure is induced after all transient

variations of the helicopter have ceased, at the 120 sec mark. The failure is induced such that the swashplate is oriented at -2 deg with a time constant of 1 sec.

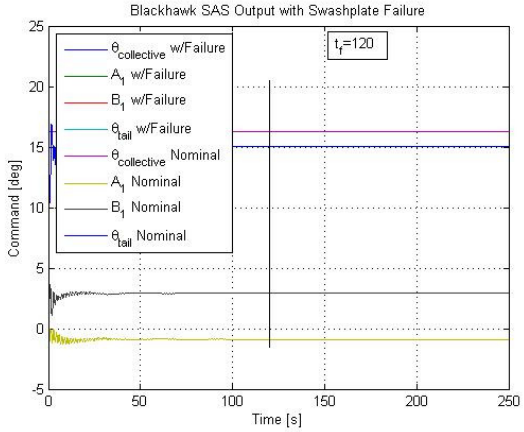

Figure 50 SAS Output for failure conditions

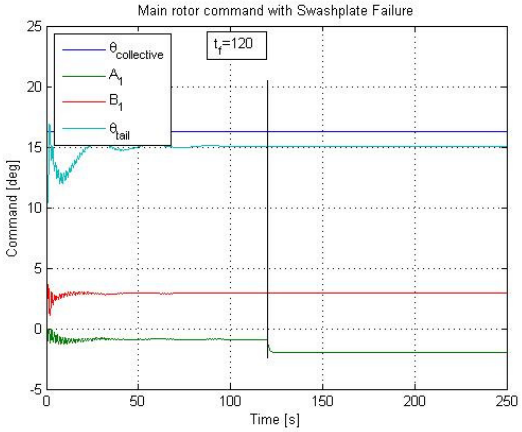

Figure 51 Actual main rotor command with failure

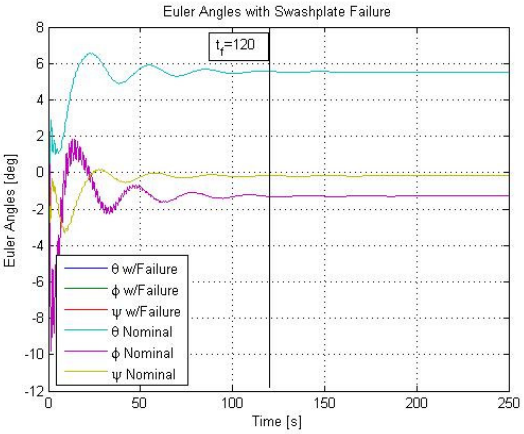

Figure 52 Euler angles under failure

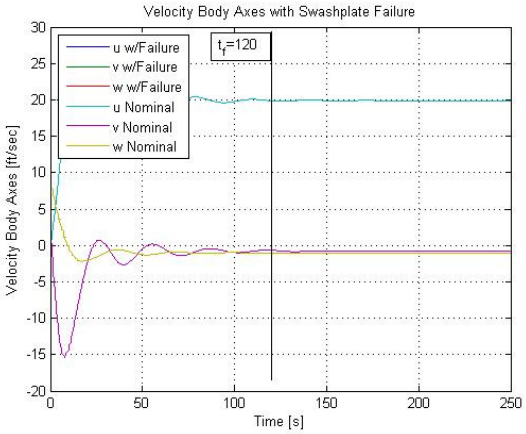

Figure 53 Body axes velocity under failure

As expected, it can be seen in Figure 54 that the IBC controller immediately takes action replacing the input that is required for the helicopter to overcome the lateral actuator failure and obtaining not only complete stabilization of the helicopter, but also avoiding any changes in the nominal flight conditions, as shown in Figure 52 (Euler angles) and Figure 53 (body axes velocity components). Figure 54 shows the output of the IBC controller for each of the blade pitch actuators of the helicopter corresponding for the compensation of the lateral swashplate actuator failure, and the compound output for the actual blade pitch angle is shown in Figure 55. Similar behavior can be recorded for the other 3 blades, which are only shifted in phase as compared to blade #1. The latter one shows how the blade pitch angle does not change and looks exactly as the one shown in Figure 28 for nominal conditions, hence obtaining the same flight conditions without additional pilot input.

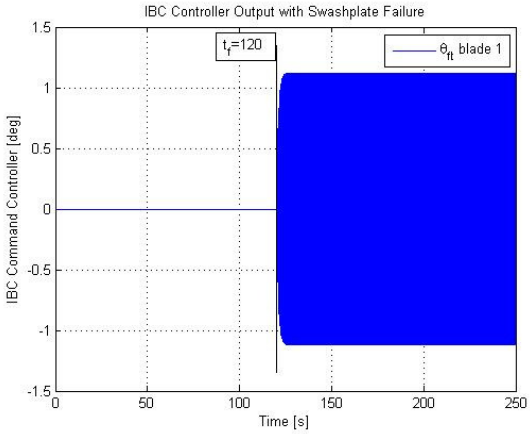

Figure 54 IBC controller output

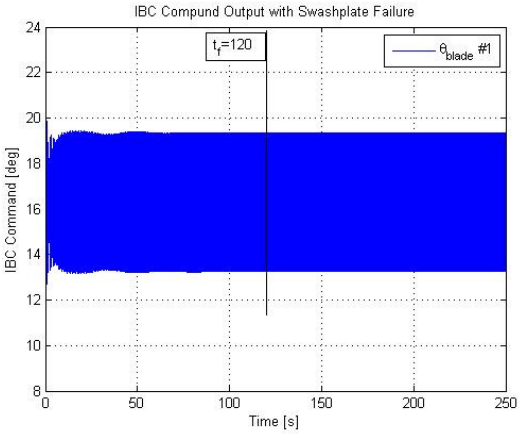

Figure 55 Actual blade orientation blade #1

A test using the same nominal conditions as previously described, but with a time delay of three seconds between the fault injection and the start of the IBC controller is shown in Figure 56 through Figure 61. As can be seen in Figure 58 and Figure 59, the body axes velocities and Euler angles are immediately affected by the lateral failure, however after 3 seconds the IBC controller starts to perform its duty and stabilizes the helicopter, and achieves close to nominal flight conditions after a 80 sec period.

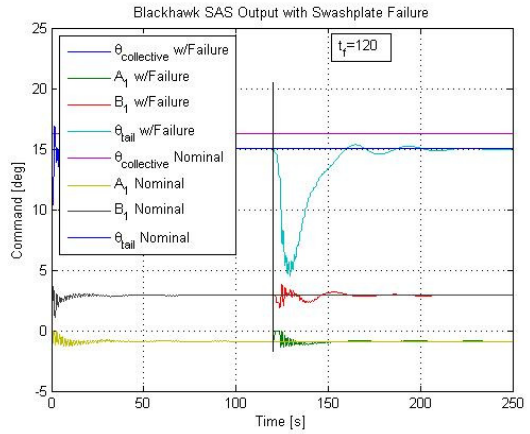

Figure 56 SAS output with failure

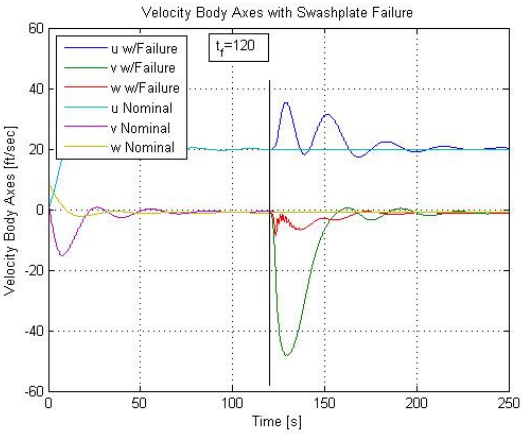

Figure 57 Actual main rotor command with failure

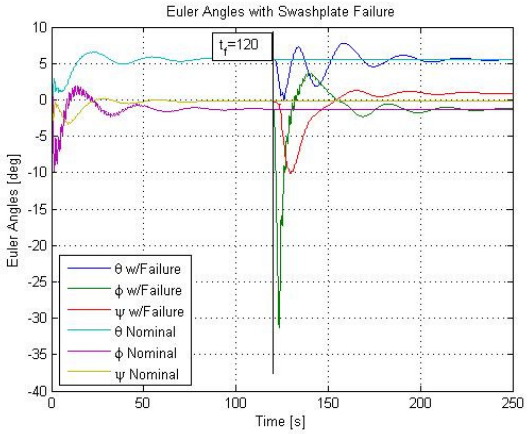

Figure 58 Euler angles under failure

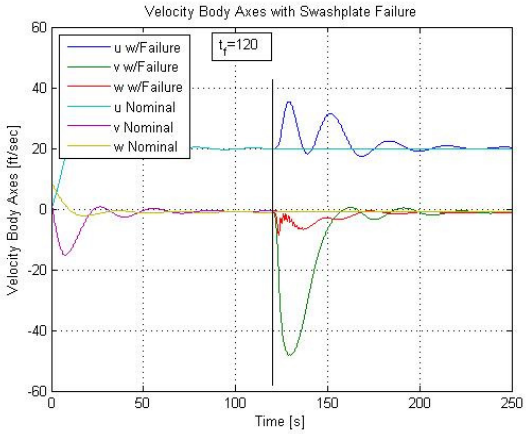

Figure 59 Body axes velocity under failure

From Figure 60 it can be seen that in comparison with the "no delay" scenario, shown in Figure 54, the IBC controller has to overcome bigger differences from the nominal conditions, hence having a higher amplitude response for the stabilizing period, and then fading away once the nominal conditions are reached.

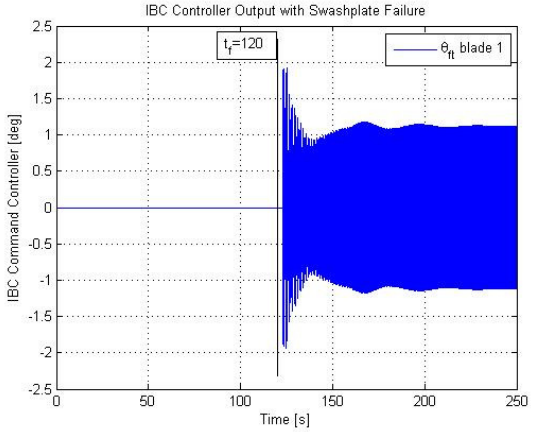

Figure 60 IBC controller output

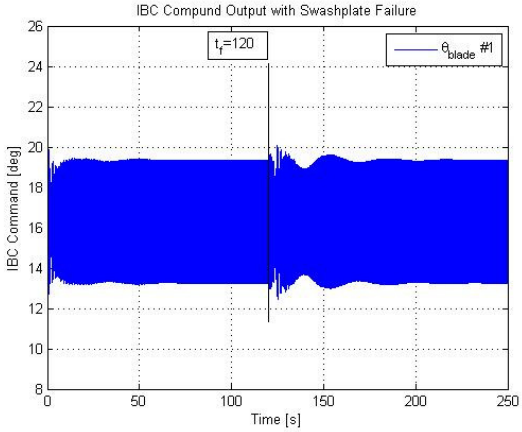

Figure 61 Actual blade orientation blade #1

A time delay of 10 seconds is tested next and the simulation results are shown in Figure 62 through Figure 68. In this case, although the IBC controller manages to eventually stabilize and obtain close to nominal conditions after a period, it can be seen in Figure 64 and in Figure 65 that the velocities and Euler angles get in an area that, eventually, the controller can stabilize; however, blade loads to achieve this state could overcome the structural capability of the blades or the hub, as can be seen in Figure 68.

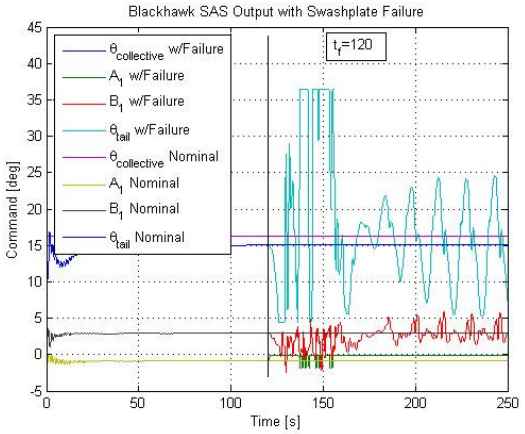

Figure 62 SAS output with failure

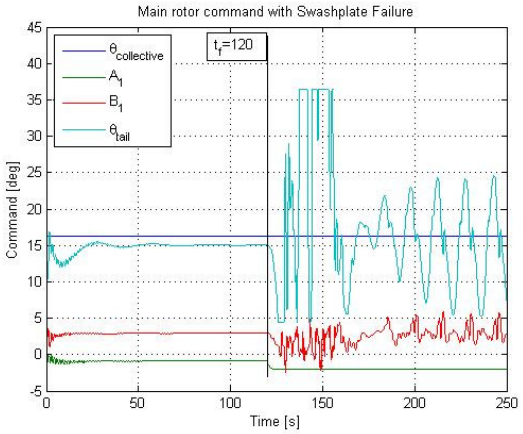

Figure 63 Actual main rotor command with failure

It can be seen from Figure 63 that the tail rotor is subjected to saturation trying to overcome the rolling moment generated by the lack of control of the lateral swashplate. Furthermore it can be inferred from Figure 65 that even if the blade structure holds, the helicopter starts to oscillate in unstable manner.

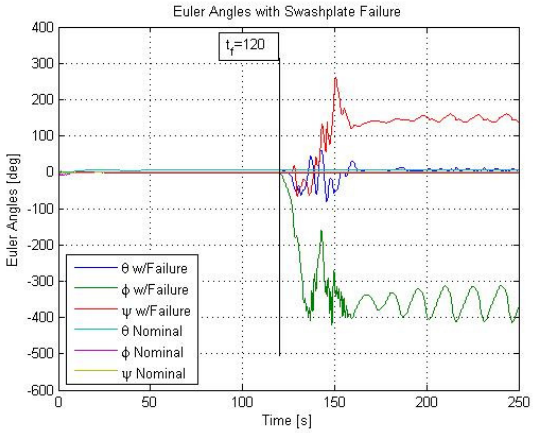

Figure 64 Euler angles under failure

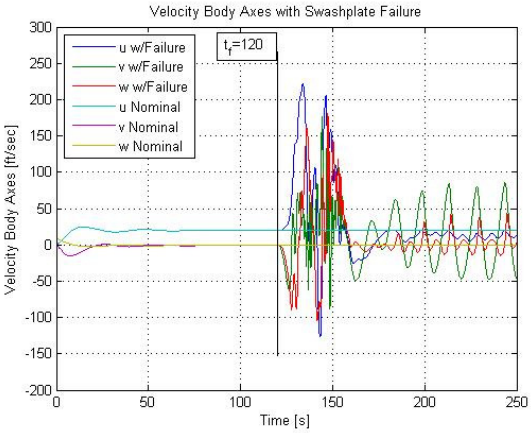

Figure 65 Body axes velocity under failure

Several tests were performed with different detection delays between 0 and 10 seconds in order to establish a range over which the accommodation is adequate. The metrics used in the analysis are steady state error, settling time, and maximum and minimum values during transients for the vehicle attitude angles and velocity vector components in body axes. Simulations were run for a window of 250 sec and, in some cases, 2% steady state values could not be reached. In order to evaluate the steady state value, an approximation to a second order system was performed. Table 5 shows the results obtained for steady state error for the helicopter's velocity in body axes and Euler angles. In this table, except for 6 second delay (for which the simulation is unstable) and the 10 second delay, the values seem acceptable.

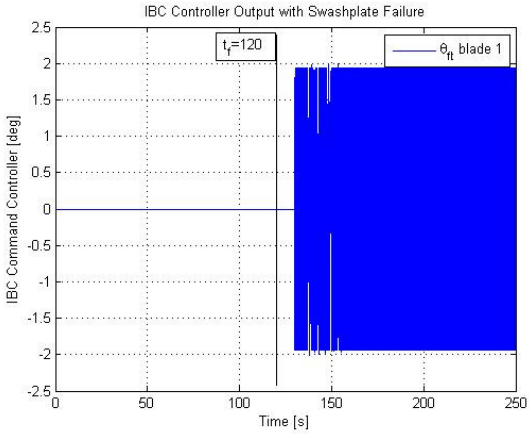

Figure 66 IBC controller output

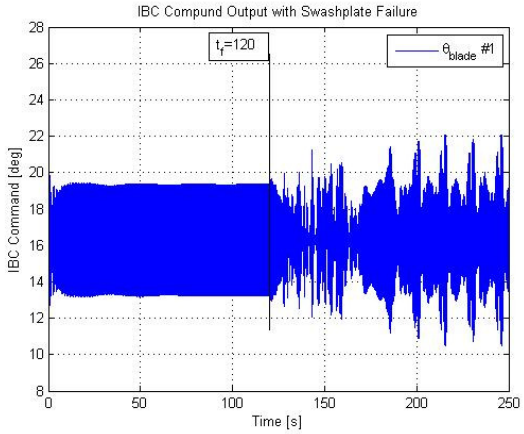

Figure 67 Actual blade orientation blade #1

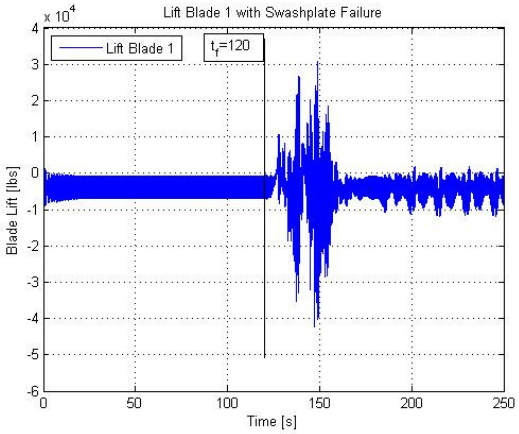

Figure 68 Lift load for blade #1

Table 5 Steady state error for different delay times (no bias)

Delay [s]	Steady State Error [ft/s] or [deg]					
	u	v	w	Θ	Φ	Ψ
0	-0.01	0	0	-0.01	0	0
1	0.01	0.02	-0.01	0.01	0.01	0.05
2	-0.29	0.33	0.11	-0.02	0.02	-0.35
3	-0.43	0.41	0.11	-0.05	-0.05	-1.11
4	-1.93	2.26	0.68	-0.09	0.14	-7.06
5	14.02	-5.42	-22.73	-16.88	-5.42	473.72
6	N/A	N/A	N/A	N/A	N/A	N/A
10	6.75	-18.51	-13.91	-1.01	360.81	-149.38

Table 6 shows the settling time for the simulations that were performed with different detection delays. A range of +/-2% of the steady state value was used to define settling time, and was measured from the start of the failure at 120 seconds. Table 7 presents the maximum and minimum values reached by each of the Euler angles and velocity in body axes of the helicopter during the transient. Using these two tables in conjunction it can be inferred that, for no pilot input, the fault detection/evaluation scheme must achieve a total delay of 3 seconds or less

without evaluation bias. This is supported by the fact that up to that specific value, the maximum and minimum values are within a safe operating range. Proper stabilization can then be achieved without excessive oscillations, structural loads, or accelerations.

Table 6 Settling time for different delay times (no bias)

Delay [s]	Settling Time [s]					
	u	v	w	Θ	Φ	Ψ
0	0.00	62.35	11.63	0.00	21.73	50.69
1	50.61	126.84	89.35	57.85	113.94	126.19
2	90.21	124.16	116.49	85.90	126.28	127.25
3	115.88	132.89	126.23	123.21	127.59	127.94
4	126.03	128.30	128.70	118.30	128.59	119.57
5	74.61	34.42	76.17	162.25	1634.10	122.79
6	N/A	N/A	N/A	N/A	N/A	N/A
10	287.29	1106.00	1308.70	164.37	8011.80	6197.20

Up until this point, it has been assumed that the fault evaluation provides an accurate reading of the position of the swashplate under failure conditions. However, in most instances this is not possible due to the difficulties associated to the evaluation and/or measurement of the position of the failed actuator. Therefore, it is important to use the simulation environment for the assessment of the robustness of the fault tolerant control scheme with respect to possible inaccuracies of the evaluation and/or measurement of the position of the failed actuator. Tests using a bias in the estimation of the position of the swashplate were performed for this purpose.

For the following analysis, a constant bias of 0.5 degrees was added to the actual position of the swashplate. For the first case, no delay time between the occurrence of the failure and the controller start was induced; all other flight conditions are the same as the ones described for nominal operation. The results for this test are shown in Figure 69 through Figure 74. As expected, the controller output, shown in Figure 73, is shifted by 0.5 degrees, which has an immediate effect in the compound output of the IBC command, shown in Figure 74, and in the behavior of the helicopter.

Table 7 Maximum and minimum values for different time delays(no bias)

Delay [s]	Maximum value in transient [ft/s] or [deg]						Minimum value in transient [ft/s] or [deg]					
	u	v	w	Θ	Φ	Ψ	u	v	w	Θ	Φ	Ψ
0	20.0	-0.7	-1.0	5.6	-1.3	-0.2	19.8	-0.9	-1.1	5.5	-1.3	-0.2
1	21.5	0.4	-0.9	6.0	0.9	0.1	19.2	-4.8	-1.4	4.8	-6.6	-1.1
2	26.7	1.2	-0.8	6.5	2.4	0.5	18.7	-22.3	-4.0	2.7	-18.7	-5.0
3	35.4	0.5	-0.6	7.8	3.7	1.3	17.3	-48.3	-8.6	0.0	-31.3	-10.2
4	96.2	13.0	15.8	38.1	7.3	17.2	-60.5	-66.3	-22.9	-19.6	-44.7	-75.4
5	172.3	66.8	119.7	83.3	49.2	0.0	-51.7	-98.6	-37.7	-47.0	-69.7	-1833.2
6	N/A	N/A	N/A	N/A	N/A	N/A	N/A	N/A	N/A	N/A	N/A	N/A
10	221.9	176.2	180.7	63.4	-1.3	260.4	-126.9	-88.6	-104.4	-82.4	-421.6	-67.4

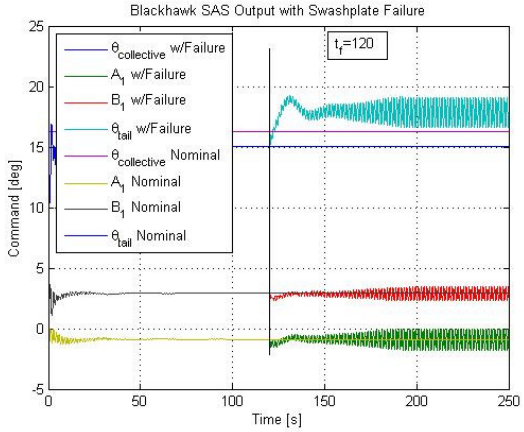

Figure 69 SAS output with failure

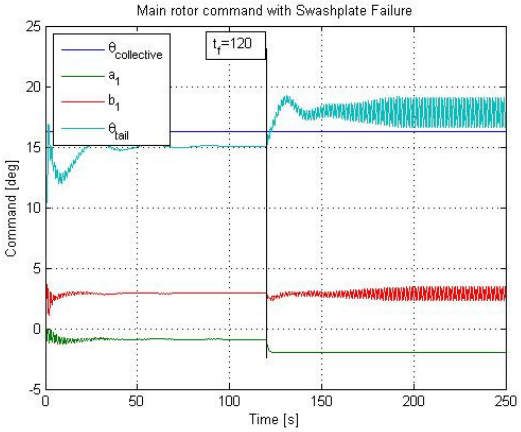

Figure 70 Actual main rotor command with failure

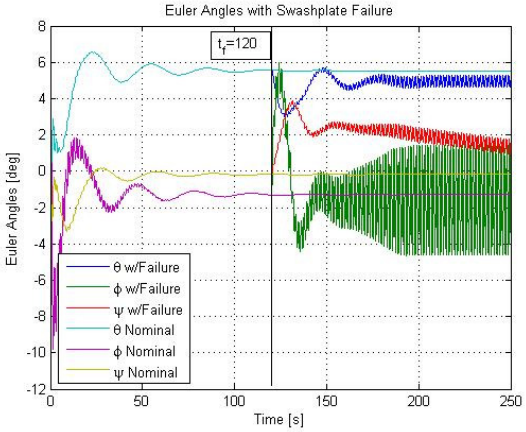

Figure 71 Euler angles under failure

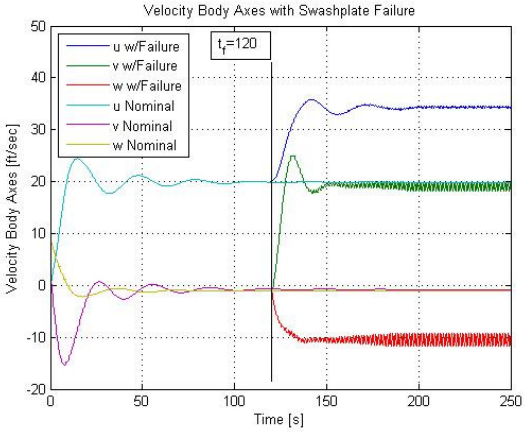

Figure 72 Body axes velocity under failure

The steady state for the Euler angles Θ, Φ, and Ψ are found to be 5, -2, and 1 degrees respectively. The high frequency variation, is caused by the lateral/longitudinal coupling and the bias of the swashplate estimation in conjunction with the effect of the tail rotor. Body axes velocities consequently have the same high frequency variations but then a perceptible new steady state for conditions after failure can be found for u, v, and w at 34, 19, and -10 ft/s, respectively. The difference between the steady state under failure, is due to the absence of closing the control loop using the states, hence for future controller design it is suggested that the states are used for feedback.

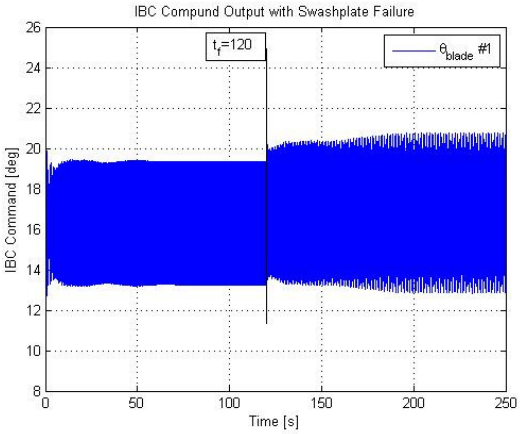

Figure 73 IBC controller output

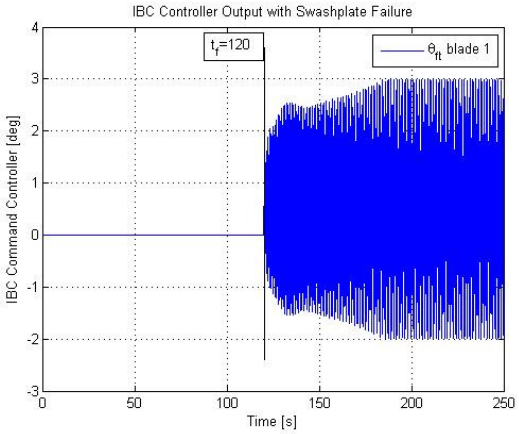

Figure 74 Actual blade orientation blade #1

The case, in which a delay of one second is added, is discussed next. This is an estimate of the time delay needed for the fault identification scheme to work, with the addition of the bias in the estimation of the swashplate orientation. The results for this test are shown in Figure 75 through Figure 80. In this case, the effect of the delay does not have a destabilizing effect. Furthermore, it seems to slightly decrease the instability as observed from Figure 77 comparing the roll attitude angle with the one shown in Figure 71. The effect of the bias in the IBC controller and compound output for the delayed response is very similar to the one in which no delay is used, showing a biased output by 0.5 degrees in Figure 79 and Figure 80. In a similar way, Euler angles and body velocity are not very different from the case with no delay. Furthermore, this shows that at least for this particular combination of bias and delay, there are not repercussions of the delay in the performance of the IBC controller including a bias in the swashplate orientation estimation

In a similar way as for the delay previous case, a sensitivity analysis using different delays and including lateral biases were performed. The results are shown in Table 8 through Table 10. The first set of tables describes the performance of the helicopter for different delay times and a bias of 0.5 deg.

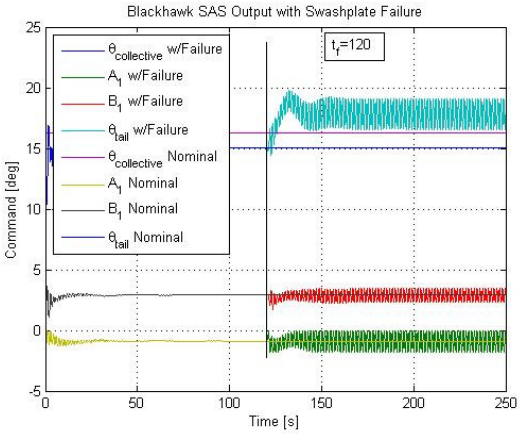

Figure 75 SAS output with failure

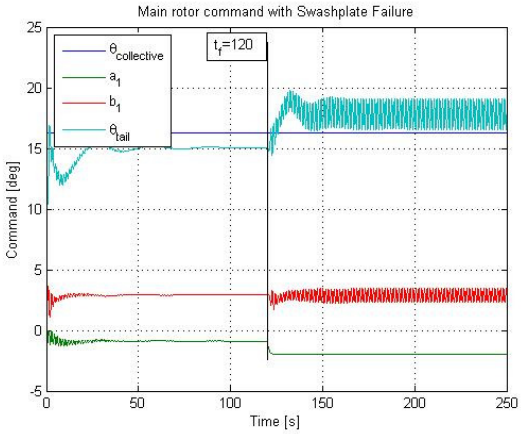

Figure 76 Actual main rotor command with failure

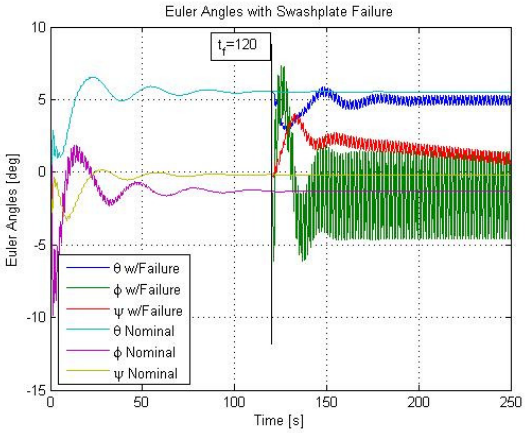

Figure 77 Euler angles under failure

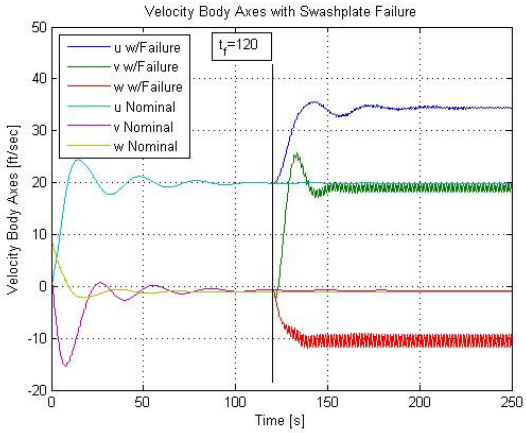

Figure 78 Body axes velocity under failure

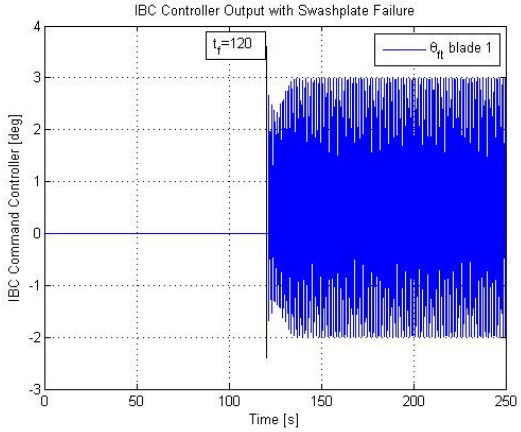

Figure 79 IBC controller output

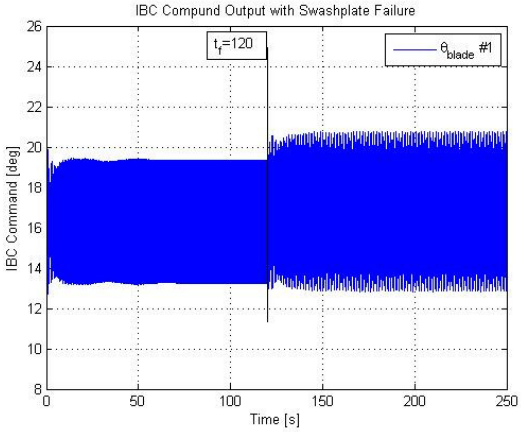

Figure 80 Actual blade orientation blade #1

Table 8 Steady state error for different delay times with a bias of 0.5 degrees

Delay [s]	Steady State Error [ft/s] or [deg]					
	u	v	w	Θ	Φ	Ψ
0	-14.35	-19.86	9.51	0.57	0.61	-2.77
1	-14.51	-19.53	9.45	0.56	0.47	-2.65
2	-13.78	-21.94	9.71	0.61	0.54	-3.94
3	-13.78	-21.21	9.62	0.68	0.67	-5.65
4	-13.67	-21.48	9.72	0.35	0.61	-4.87
5	-14.61	-20.17	9.25	0.86	0.66	9.86
6	-14.69	-20.42	9.33	0.81	-1.21	34.17
10	-17.11	-56.67	-36.74	-0.52	350.61	-70.44

Table 9 Settling time for different delay times with a bias of 0.5 degrees

Delay [s]	Settling Time [s]					
	u	v	w	Θ	Φ	Ψ
0	161.62	1884	8181.9	9350.8	271.13	340.46
1	164.07	1547.8	19081	7126.8	317.58	277.73
2	161.99	4245.4	28736	3597.7	852.98	550.11
3	177.51	3011.4	1734.8	1911.5	402.41	756.30
4	204.16	683.54	6457.5	330.28	164.73	633.39
5	204.74	578.38	1945.9	419.73	860.39	1036.84
6	208.16	436.94	8779.7	813.22	163.53	204.32
10	2123.5	968.92	737.21	1121.9	22931	340.46

Table 10 Maximum and minimum transient values for different delays (Bias=0.5deg)

Delay [s]	Maximum value in transient [ft/s] or [deg]						Minimum value in transient [ft/s] or [deg]					
	u	v	w	Θ	Φ	Ψ	u	v	w	Θ	Φ	Ψ
0	35.8	25.1	-1.1	5.7	6.0	3.9	19.9	-0.7	-11.8	3.0	-4.6	-0.2
1	35.6	25.7	-1.1	5.9	7.3	4.0	19.8	-2.7	-11.8	2.8	-6.1	-0.3
2	38.5	27.4	-1.1	6.1	9.3	4.7	19.8	-14.4	-12.2	2.0	-18.3	-1.5
3	42.2	26.8	-1.1	6.9	10.8	6.2	19.8	-36.3	-12.0	-0.2	-30.9	-5.7
4	74.4	30.5	2.9	17.5	18.5	6.4	13.8	-60.9	-18.7	-4.9	-44.2	-38.0
5	106.7	82.7	35.5	78.0	36.6	47.8	-35.6	-83.1	-32.2	-33.6	-57.8	-81.5
6	154.6	95.1	86.6	71.6	79.5	26.8	-23.5	-96.3	-53.0	-46.2	-77.3	-91.5
10	225.6	155.6	164.7	46.4	-1.3	108.8	-67.6	-62.4	-89.1	-74.5	-415.4	-67.4

From the previous analysis, it is clear that the architecture for individual blade control under failure demonstrates a stabilizing effect in most cases (as long as the delay of the failure and the bias of the swashplate reading are not too big). However, a bias in the swashplate incurs a bias in the selected body axes velocity, an issue that also needs to be addressed by the controller architecture. Furthermore, if there is a failure for the individual blade actuator, the swashplate will have to compensate to account for the loss of the actuator. In this case the solution is not straightforward, since there is not a clear relationship between the angles of each of the blades with the forces and moments to preserve nominal behavior of the helicopter, therefore in this particular case, techniques such as neural networks can potentially prove useful.

5.1.2.2 Definition of Composed Error Metric

Since the comparison of different architectures and failures requires the evaluation of many different variables at the same time, an innovative composed error metric was defined using different parameters form the classic control approach in order to characterize control laws performance. First, the components in body axes (u, v, and w) of the vehicle velocity and the attitude angles (Θ, Φ, Ψ) are selected as primary states for performance evaluation. The velocity components are normalized using the product of the main rotor nominal angular speed and rotor radius. The steady state error is defined in equation (209) as the difference between the steady state value at nominal conditions and the steady state value under failure conditions

$$e_{ss} = X_{ss_{nom}} - X_{ss_{fail}} \tag{209}$$

To measure the transient error, the sum of the difference between the value of the state in nominal and failure conditions minus the steady state error is calculated as shown in equation (210). The value of the steady state is subtracted so the transient is not penalized for mismatch of steady state conditions. This effect will be later added to the composed metric itself.

$$e_{abs} = \sum_{t=t_f}^{t_o} \left| X_{t_{nom}} - X_{t_{fail}} - e_{ss} \right| \tag{210}$$

To measure the effect of minimum and maximum values of each of the states, the difference between the maximum and minimum values of each of the states under failure is calculated as shown in equation (211).

$$\Delta_{\max} = \max\left(X_{fail}\right) - \min\left(X_{fail}\right) \tag{211}$$

Finally, the composed error metric is then defined as described in equation (212), for which the steady state error, the transient behavior, and the difference between the maximum and minimum values are combined in one single parameter *E*, which is expected to condense information and capture the essence of all components. The evaluation parameter E is formulated such that, if the dynamic response at failure conditions is identical to the one at nominal conditions, the value becomes 0. As conditions deteriorate from the nominal case, the parameter E gets closer to one.

$$E = 1 - \frac{\left(1 - \frac{e_{ss}}{\max\left(e_{ss}\right)}\right) + \left(1 - \frac{e_{abs}}{\max\left(e_{abs}\right)}\right) + \left(1 - \frac{\Delta_{\max}}{\max\left(\Delta_{\max}\right)}\right)}{3} \tag{212}$$

Each parameter is normalized using the maximum value from the different values calculated for the same parameter. For instance, if an analysis is performed to different time

delays, for each time delay there is a value of steady state error for a particular variable; hence the normalizing factor will be the maximum value of steady state error for all the time delays analysed. This approach guarantees that each parameter varies from 0 to 1 in that specific test batch. This also shows the relative nature of the compound error metrics, it is intended to compare the performance of several tests with different parameters varying at the same time, not as an abosolute performance value.

The formulation of this composed error metric allows for more parameters to be added, if deemed important in the sensitivity analysis, and selective weights can be considered if some components are more important than others. A general formulation for this compound error metric can be found in equation (213) for n parameters. Each parameter m varies from 0 to 1 (with values close to zero, as flying conditions close to nominal and 1 for really degraded states) and is multiplied by relative weights k. These weights also vary from 0 to 1.

$$E = 1 - \frac{1}{n}\sum_{i=1}^{n} k_i m_i \tag{213}$$

Using the metric defined in equation (212), the results presented in Table 11 through Table 14 were obtained, respectively, for the lateral failure case for the no bias and a bias equal to 0.5 deg, and for a longitudinal failure with a bias of 0.2 deg.

Table 11 Error metrics for lateral failure (Bias = 0 deg)

Delay [s]	E						
	u	v	w	Θ	Φ	Ψ	ΣE
0	3.35E-05	3.72E-05	7.46E-06	1.35E-05	1.31E-05	7.24E-06	1.12E-04
1	4.34E-04	9.85E-04	1.08E-04	2.48E-04	1.46E-03	3.02E-04	3.53E-03
2	1.72E-03	4.59E-03	6.62E-04	8.23E-04	4.14E-03	1.55E-03	1.35E-02
3	3.68E-03	9.36E-03	1.57E-03	1.76E-03	6.97E-03	3.65E-03	2.70E-02
4	3.03E-02	1.64E-02	7.60E-03	1.26E-02	1.07E-02	2.67E-02	1.04E-01
5	5.22E-02	3.46E-02	4.54E-02	4.47E-02	3.76E-02	1.00E+00	1.21E+00
6	N/A	N/A	N/A	N/A	N/A	N/A	N/A
10	6.91E-02	6.39E-02	6.23E-02	3.11E-02	4.64E-01	2.20E-01	9.11E-01

Table 12 Error metrics for longitudinal failure (Bias = 0 deg)

Delay [s]	E						
	u	v	w	Θ	Φ	Ψ	ΣE
0	3.12E-05	3.72E-05	7.46E-06	1.30E-05	1.31E-05	7.24E-06	1.09E-04
1	4.53E-04	3.62E-04	9.67E-05	3.36E-04	2.77E-04	9.95E-05	1.62E-03
2	2.29E-03	1.82E-03	4.43E-04	1.49E-03	1.05E-03	7.02E-04	7.80E-03
3	4.70E-03	2.97E-03	7.20E-04	3.28E-03	1.89E-03	1.81E-03	1.54E-02
4	8.51E-03	2.81E-03	1.09E-03	6.11E-03	2.03E-03	2.78E-03	2.33E-02
5	1.33E-02	5.10E-03	1.37E-03	8.49E-03	2.56E-03	5.59E-03	3.64E-02
6	1.57E-02	6.72E-03	1.67E-03	8.96E-03	2.96E-03	8.20E-03	4.42E-02
10	1.65E-02	8.31E-03	1.83E-03	8.03E-03	3.29E-03	8.41E-03	4.64E-02

These results show that a natural progression of the evaluation parameter E occurs for all of the different failure cases, lateral and longitudinal, for increasing failure detection and evaluation delay. This confirms the error-reducing and stabilizing capability of the control laws. This trend was observed in all the tables for which the error metric is minimum when no delay is applied to the system and no bias is used either. For the no bias case, a threshold of acceptable performance for the lateral dynamics was set at 4 seconds, since for 5 seconds, maximum and minimum values of the roll and pitch angles made the performance somewhat dangerous (with pitch angles going up to -83 deg). Hence, a threshold value of the no bias case of ΣE would be 1.4E-01, which summarizes acceptable helicopter performance with a small safety margin. This is the value of the sum of the compound error metrics for lateral failure for the 3 second delay.

If the value for the compound error for the lateral case is used as a benchmark, for the longitudinal case, it can be seen that the value of ΣE does not overcome this particular threshold. Furthermore, the values for the delta, the accumulation of the error and the steady state error for this particular case can be considered as acceptable.

Table 13 Error metrics for lateral failure (Bias = 0.5 deg)

Delay [s]	E						
	u	v	W	Θ	Φ	Ψ	ΣE
0	1.34E-02	1.92E-02	8.89E-03	1.18E-03	3.82E-03	3.42E-03	4.99E-02
1	1.35E-02	1.95E-02	8.85E-03	1.21E-03	4.91E-03	3.28E-03	5.12E-02
2	1.35E-02	2.37E-02	9.15E-03	1.56E-03	7.07E-03	5.06E-03	6.00E-02
3	1.41E-02	2.71E-02	9.02E-03	2.18E-03	9.29E-03	7.97E-03	6.97E-02
4	2.11E-02	3.25E-02	1.10E-02	5.09E-03	1.45E-02	1.37E-02	9.80E-02
5	3.67E-02	4.51E-02	1.92E-02	2.27E-02	2.05E-02	3.49E-02	1.79E-01
6	4.33E-02	5.00E-02	3.24E-02	2.35E-02	3.26E-02	5.82E-02	2.40E-01
10	6.68E-02	8.14E-02	7.46E-02	2.66E-02	4.61E-01	1.07E-01	8.17E-01

Taking the same value (ΣE=1.4E-01) as a benchmark for the case in which a bias of 0.5 deg is induced for the lateral failure, it can be observed from Table 13 that the acceptable threshold is between 4 and 5 seconds. This threshold is confirmed by the fact that between these particular set of time delays in Table 10, the roll and pitch angles have barely acceptable values.

Table 14 Error metrics for longitudinal failure (Bias = 0.2 deg)

Delay [s]	E						
	u	v	w	Θ	Φ	Ψ	ΣE
0	2.60E-03	1.04E-02	3.81E-03	3.18E-04	8.55E-04	2.14E-03	2.01E-02
1	2.70E-03	1.03E-02	3.80E-03	5.11E-04	8.89E-04	2.09E-03	2.03E-02
2	4.01E-03	1.05E-02	4.08E-03	1.58E-03	9.77E-04	2.18E-03	2.33E-02
3	6.81E-03	1.13E-02	4.43E-03	3.39E-03	1.79E-03	2.94E-03	3.06E-02
4	1.18E-02	1.07E-02	4.58E-03	6.79E-03	2.21E-03	3.79E-03	3.99E-02
5	1.62E-02	1.28E-02	4.64E-03	9.03E-03	2.36E-03	6.34E-03	5.14E-02
6	1.82E-02	1.44E-02	4.80E-03	9.69E-03	2.65E-03	9.85E-03	5.96E-02
10	1.97E-02	1.69E-02	4.74E-03	8.15E-03	3.70E-03	1.11E-02	6.43E-02

Similar tables were calculated for a bias of 0, 0.2, 0.5, and 1 deg for lateral and longitudinal failures. Further concentration of the evaluation parameter was performed by summing up the error metrics for all the variables for each of the delay times and biases. These values are presented in Table 11 through Table 14 as ΣE. The loci of failure detection delays and biases for constant values of ΣE are presented in Figure 81, for the lateral failure, and in Figure 82, for the longitudinal failure. As expected, for a desired value of ΣE the acceptable values of the delay and bias are slightly smaller for the lateral failure than for the longitudinal failure. This fact confirms the increased sensitivity of the helicopter to a lateral failure. Furthermore, unstable simulations occurred only for the lateral case with a rather large area of instability for large detection delays. This zone is limited by large values of the error metrics, hence providing a good qualitative assessment on the natural abilities of the IBC controller scheme and the performance characteristics that a future detection scheme must have in order to effectively support failure accommodation.

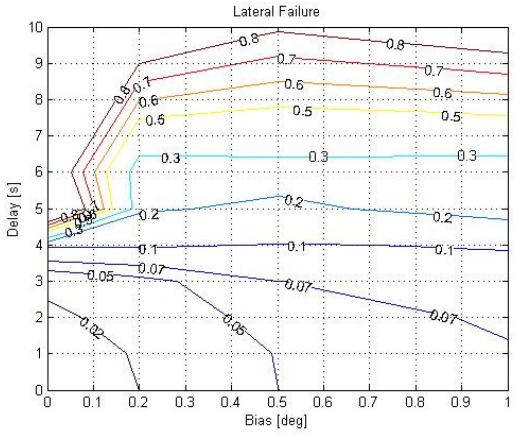

Figure 81 Error metrics with respect to bias and delay for lateral failures

For the lateral failure, it can be inferred from Figure 81 that there is a steady progression of the error metrics in both delay and bias from 0 to 3 seconds and from 0 to 0.2 deg respectively. This trend seems to stop after the 5 second mark, at which the increase in bias does not seem to affect the error metric, especially since the unstable behavior occurs at low bias and long delays.

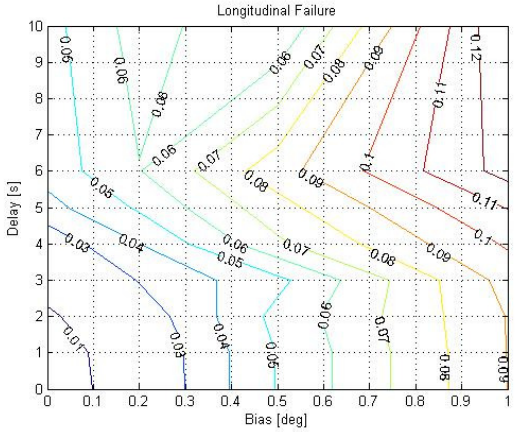

Figure 82 Error metrics with respect to bias and delay for longitudinal failure

In the case of the longitudinal failure, a different pattern is presented in Figure 82. The bias appears to have a larger impact on the error metric than the delay for the 0 to 3 sec range. After the 3 second mark, from the 3 to the 6 second delay period, there is a larger impact of the delay on the error metric. This result seems to support the requirement that the failure detection and evaluation method be rather fast than accurate. For longer delays, the bias tends to exhibit a more significant effect; however, the delay remains the primary factor in the increase of the error metric. It should be noted that the values of the longitudinal metric are lower than the lateral ones, for the same pairs of delay/bias. This behavior shows that the system is more sensitive to lateral abnormal conditions and could potentially handle more severe longitudinal failures than lateral ones.

From both charts it can be inferred that for no time delay in the failure, the compound error metrics values are fairly low, which shows an acceptable performance of the helicopter for the analyzed range of the bias. If a threshold of bias is required, for which the helicopter performance is not acceptable, with no delay, a wider range of bias values need to be simulated to avoid extrapolation issues.

The charts were calculated using equal weights for steady state error, the absolute value between the maximum and minimum values and the accumulation of the error in the transitory; hence a small value for ΣE will in turn determine good performance in all three variables on average. Taking that into account, the charts can be used as a design tool for the development of the fault detection scheme. For instance, in the case where a fault detection scheme is being designed for the lateral failure, and it is required that the compound error can not be bigger than 0.05, and an admissible error for the bias is 0.3 deg. Then, from the charts, it can be observed that a threshold for the period of time required by the same fault detection scheme is 2.8 seconds.

As another example, if a detection scheme is implemented in such a way that, for the longitudinal failure, the best performance occurs for a bias of 0.6 deg and 3 seconds delay, then, from the chart in Figure 82, it can be inferred that the compound error metrics will be 0.06, which is similar to what the helicopter would suffer for a failure with a bias of 0.2 deg and 10 seconds delay, and estimates of the steady state error, sum of the error in the transitory, and absolute value of the maximum and minimum values can be made.

5.1.3 Swashplateless Architecture

Mathematically, there is no difference between the architecture of classic swashplate with IBC actuators and a full IBC system that uses a virtual swashplate at nominal conditions. Hence, the nonlinear relationship that exists between the blade pitch angle and the forces and moments of the rotor is the same for the second case as it is for the first one. Thus, in order to keep nominal conditions under failure for a swashplateless architecture, recursive techniques such as neural networks can prove a good solution.

The virtual swashplate is intended to mimic the performance of each of the blades as if a real mechanical swashplate, existed. Even though that the virtual swashplate concept limits the almost limitless capabilities of the individual blade control concept, exploiting only the redundancy, it is the first stepping stone in the understanding of how this technology improves the performance of a helicopter under failure conditions since it is easier to implement and requires classic control approaches. Furthermore, there are some differences with the classic + IBC architecture in the sense that the swashplateless architecture does not necessarily require a fault detection scheme, since it has intrinsic fault tolerant capabilities. These intrinsic capabilities lay in the fact that if even if one of the blade actuator fail, the nominal controller is still capable

of generating the required forces and moments, in a reduced percomance state, without any reconfiguration. That does not necessarily mean that some reconfiguration still might not be useful.

5.1.4 Main Rotor Mechanical Degrees of Freedom (DOF)

In a general way, the degrees of freedom of a mechanical system are the set of independent displacements and/or rotations that specify completely the displaced or deformed position and orientation of each of the mechanical elelments of the given system[63]. For instance, to determine the location of all the bars and pivots of a 4 bar plane mechanism, with one bar being the ground, only one bar position is required to solve for the location and orientation of the rest, since it is a mechanical system with a single degree of freedom. If the main rotor of a helicopter is assumed as a similar system, in order to know the position and orientation of all the mechanical parts that form the mechanism itself, the collective cyclic, the lateral and longitudinal cyclic, and the blade azimuth angle must be known. Thus, the system has 4 degrees of freedom - one for each channel - and these interact to generate the forces and moments required to control the helicopter. It is to be noted that most of the times the azimuth angle is not included as a control variable, since the main rotor headspeed is kept constant so issues regarding compressibility are kept under control. Thus, in practical terms there are only 3 DOF for a classic swashplate approach. It is to be noted that each of this degrees of freedom are linked to the production of forces and moments: the lateral cyclic generates a roll moment, the longitudinal cyclic generates a pitching moment, and the collective changes the amount of lift created by the main rotor itself. Even though there are coupling effects between the lateral and longitudinal dynamics, diplacements in one direction must have certain specific characteristics, in terms of amplitude and frequency, to be able to control the coupled direction, which is not very common for the whole envelope. Hence, there is almost no redundancy for the production of forces and moments in the classic swashplate architecture.

In the case where blade pitch actuators or any other mechanism for IBC is added to the system, an additional degree of freedom is summed up to the entire system, with each of these degrees of freedom able to generate lift, lateral and longitudinal moments, increasing the redundancy of the main rotor. Therefore, if a 4 bladed helicopter as the Blackhawk is fitted with IBC actuators, the redundancy would be more than double the original one.

In the case that a swashplateless architecture is analyzed, the main rotor system will have as many degrees of freedom as blades, therefore a 3 bladed-rotor will have the same degrees of freedom, however it will not have the same redundancy, since cyclic and collective inputs, for the swashplateless case, can still be composed to obtain close to nominal behavior on the remaining blades if one actuator failure occurs. Thus, for the case of this study, the Blackhawk helicopter, a 4 DOF is analyzed using swashplateless architecture and compared against the classic swashplate architecture.

When an actuator failure occurs, as defined in this dissertation, the capability to specify the displacement or velocity for that particular input is lost, thus, the degree of freedom associated with that specific input or actuator is lost too, and the overall system will have at least one degree of freedom less than in healthy conditions. Having discussed the impact of the loss of degrees of freedom for a mechanical system, the consequences of this loss on the handling qualities of a helicopter is discussed next.

In the case of the classic approach, the loss of this particular degree of freedom will have different effects depending on which actuator fails. If the affected actuator is the one that changes the orientation of the swashplate, either lateral on longitudinal, this will prevent the helicopter itself to generate most of the moments in that particular direction (given that moments can be still generated due to the coupling of the lateral and longitudinal dynamics and some are generated by the tail rotor). Furthermore, if the failed actuator is the one that controls the main rotor collective, the impact will be a little less catastrophic given that moments in the lateral and longitudinal axis can still be generated by the swashplate, and these can be used in conjunction to dissipate (or generate in case of autorotation) the lift energy produced by the collective and descend with certain safety.

In case that the failed actuator occurs in either the swashplate or the collective actuator, when using a classic swashplate architecture fitted with IBC actuators, the degrees of freedom of the system will allow to compensate for the failed actuator.

Finally, if the actuator failure occurs when using a swashplateless architecture, although the mechanical system will have less degrees of freedom, the remaining blade(s) will be able to generate moments in the lateral and longitudinal directions and forces to generate thrust since the mixing occurs not mechanically but using software.

5.1.5 Probability Analysis

A probability analysis of the different architectures for actuator failure is performed next. It is assumed that the probability of a failure for a swashplate actuator and an individual blade control actuator is the same, and will be represented by the letter "p".

- Classic Swashplate

If the probability of an actuator to fail is associated with the degrees of freedom of the system itself, the cumulative probability for one actuator to fail can be calculated as can be observed in equation (214). In that particular case the probability of failure is 3p, and if it is assumed that each actuator is associated with a degree of freedom, then if the lateral or longitudinal swashplate actuator is affected by a failure, the forces and moments associated with the failed actuator can not be generated or changed. Furthermore, the survivability of the aircraft can be heavily compromised, as has been proven already in section 4.4 of this dissertation. However, if the failure affects the collective actuator only, the cyclics can be manipulated so safe flying is still possible but in a degraded performance state.

$$P_{fail} = p * DOF_{swashplate} = 3p \tag{214}$$

-Classic Swashplate + IBC

In this case, as observed in equation (215), the probability of failure is 7p, which makes it the highest of all three architectures, however if one of the swashplate actuator fails, the IBC actuator can compensate for said failure. If one of the IBC actuator fails, forces and moments can still be generated in all axes.

$$P_{fail} = \left(DOF_{swashplate} + DOF_{IBC} \right) p = 7p \tag{215}$$

- Swashplateless

This architecture, which is also referred as the full authority IBC, has a probability slightly bigger than the classic swashplate, as seen in equation (216), however if one of the actuators is affected by a failure, forces and moments can still be generated in all axes, allowing for safe flying even in a degraded state.

$$P_{fail} = DOF_{IBC} * p = 4p \quad \textbf{(216)}$$

5.2 Controller Architecture

In order to test the influence of individual blade control as a feasible option for survivability increase in case of actuator failure for the main rotor (either swashplate or collective), a similar architecture will be designed for all the configurations to be tested, classic swashplate, swashplateless (IBC with full authority), and swashplate with individual blade control. The controller and its reconfiguration will be modified according to each of the architectures in order to exploit the inherent fault tolerant characteristics of that particular setup.

5.2.1 Classic Control Architecture

A classic control architecture was implemented in order to guarantee a stable hover, and forward flight for analysis. Furthermore, the development of the NLDI augmented with neural networks requires the stabilization of the translational dynamics. A linear controller was used to stabilize the helicopter for hover and a forward speed of 20 ft/s. A proportional and integral approach was used for all three velocity axis. The performance parameters for the design of each loop are listed in Table 15.

Table 15 Performance parameters

Variable	ζ	ω_n	τ [s]
u	0.34	0.18	N/A
v	0.12	0.42	N/A
w	0.26	0.4	N/A
Ψ	N/A	N/A	43.1

Considering the parameters, primary controls were included in each loop to counteract for the error, and for each controlled variable, proportional and integral gains were found as shown in Table 16. Also an additional loop was added in order to cancel for any error in the heading angle.

Table 16 Classic control characteristics

Variable	Primary Control	Kp	Ki
u	Longitudinal Cyclic	0.08	0.002
v	Lateral Cyclic	0.08	0.002
w	Collective	0.0001	0.04
Ψ	Pedals	1	0.03

Using these gains, a linearization process was performed for hover and forward flight. The poles for such linearized models are listed in Table 17 and Table 18. As can be observed in both tables, all the eigenvalues are located either at zero or are on the left hand side of the s-plane, which guarantees stability of the model.

Table 17 Eigenvalues for the classic control model in hover

0	-0.2108	-2.3809	-17.5043	-56.9082 + 35.1887i
0	-0.0477 - 0.295i	-2.5125	-24.1	-48.9973- 49.9896i
0	-0.0477 + 0.295i	-0.9290 - 2.5035i	-24.1	-48.9973+ 49.9896i
0	-0.1418 - 0.4361i	-0.9290 + 2.5035i	-24.1	-51.6253 - 49.8672i
0	-0.1418 + 0.43615i	-4.2978	-44.9729	-51.6253 + 49.8672i
0	-0.0473 - 0.5544i	-4.5866 - 4.2817i	-36.5144 - 41.9851i	-56.5291 - 48.3283i
0	-0.0473 + 0.5544i	-4.5866 + 4.2817i	-36.5144 + 41.9851i	-56.5290 + 48.3283i
0	-0.4369 - 0.3757i	-4.3897 - 4.4833i	-34.2752 - 46.3228i	-56.5586 - 62.2972i
0	-0.4369 + 0.3757i	-4.3897 + 4.4833i	-34.2752 + 46.3228i	-56.5586+ 62.2972i
2.053e-14	-1	-7.3002	-59.3402	-55.7879 - 63.2971i
-0.0204	-1	-9.944	-37.4396 - 53.4979i	-55.7879 + 63.2971i
-0.0301	-1.1919 - 0.0425i	-15.4785 - 5.12306i	-37.4396 + 53.4979i	-58.6931 - 64.5771i
-0.1138	-1.1919 + 0.0425i	-15.4785 + 5.12306i	-56.9082 - 35.1887i	-58.6931 + 64.5771i

Table 18 Eigenvalues for the classic control model in forward flight

0	-0.0049 – 0.0668i	-2.3809	-17.1561	-56.9098 + 35.1753i
0	-0.0049 + 0.0668i	-1.0203 – 2.5575i	-24.1	-48.9973 – 49.9896i
0	-0.0786 - 0,.101i	-1.0203 + 2.5575i	-24.1	-48.9973 + 49.9896i
0	-0.0786 + 0.1101i	-2.8735	-24.1	-51.6535 – 49.8642i
0	-0.2441	-5.8118 – 1.2067i	-45.0395	-51.6535 + 49.8642i
0	-0.1761 – 0.4059i	-5.8118 + 1.2067i	-36.4935 – 42.0099i	-56.7458 – 48.3308i
0	-0.1761 + 0.4059i	-4.3897 – 4.4833i	-36.4935 + 42.0099i	-56.7458 + 48.3308i
-4.8094e-08	-0.4328 – 0.3492i	-4.3897 + 4.4833i	-34.1334 – 46.4465i	-56.5518 – 62.2991i
-1.4028e-06	-0.4328 + 0.3492i	-4.5866 – 4.2817i	-34.1334 + 46.4465i	-56.5518 + 62.2991i
-5.3341e-05	-1	-4.5866 + 4.2817i	-59.6065	-55.7481 – 63.3495i
-0.0045	-1	-9.9116	-37.4471 – 53.5041i	-55.7481 + 63.3495i
-0.0294	-1.2674 – 0.0982i	-15.5164 – 5.3716i	-37.4471 + 53.5041i	-58.6951 – 64.5756i
-0.0531	-1.2674 + 0.0982i	-15.5164 + 5.3716i	-56.9098 – 35.1753i	-58.6951 + 64.5756i

5.2.2 NLDI+NN Architecture

The nonlinear dynamic inversion augmented with neural networks is based on the inversion of a linear model for a specific trim condition, obtaining the inputs to the system given the outputs, or in this case, the desired behavior of the helicopter. The inversion process can induce some errors. These errors can have different sources, such as modeling errors, uncertainties, external perturbation, or subsystem abnormal operation. An additional neural network is fitted to the system to correct for those errors. A detailed description of this technique is based on the work by Leitner et al[7] and is shown as follows.

5.2.2.1 Two Time Scale Control

In his work, Leitner found that the decoupling action of the heave mode with respect to the roll and pitch modes, therefore a two time scale linearizing control was the best option for the

design of the NLDI scheme. In this scheme an outer loop inversion calculates the increase in the collective, controlling the altitude and its derivative, and an inner loop inversion accounts for stabilization of the rotational states.

Thus, the outer loop pseudocontrols are calculated as shown in equation (217), where A is the gain matrix of the error for the translational states, which were calculated to match the requirements stated in Table 19 x_I is the state vector in inertial coordinates North-East-Down, as shown in equation (218), and υ are the pseudocontrols for the outer loop. The values for the A matrix that were used for this design are found in equation (219).

$$\upsilon = \dot{x}_{I_{com}} + A\left(x_{I_{com}} - x_I\right) \tag{217}$$

$$x_I = \begin{bmatrix} \dot{X} & \dot{Y} & \dot{Z} & \dot{\phi} & \dot{\theta} & \dot{\psi} & X & Y & Z & \phi & \theta & \psi \end{bmatrix}^T \tag{218}$$

$$A = \begin{bmatrix} 0.8 & 0 & 0 & & \\ 0 & 0.8 & 0 & & 0_{3x9} \\ 0 & 0 & 0.8 & & \\ & & & & \\ & 0_{9x3} & & & 0_{9x9} \\ & & & & \end{bmatrix} \tag{219}$$

Table 19 Performance parameters control scheme

Variable	ζ	ω_n	τ [s]
u	0.02	2.93	N/A
v	0.38	0.13	N/A
w	N/A	N/A	5.5

Based on the previously calculated pseudocontrols, a new orientation of the main rotor is calculated, as shown in equation (220) using increments on the roll and pitch angles from trim.

$$\begin{aligned} \bar{\phi} &= \arctan\left(\frac{\upsilon_1 \sin\psi_{com} - \upsilon_2 \cos\psi_{com}}{\upsilon_3 - g}\right) + \phi_{trim} \\ \bar{\theta} &= \arctan\left(\frac{\upsilon_1 \cos\psi_{com} + \upsilon_2 \sin\psi_{com}}{\upsilon_3 - g}\right) + \theta_{trim} \end{aligned} \tag{220}$$

The non-dimensional state vector in body frame is defined as shown in equation (221). Where x_B, shown in equation (222), is the state vector in body reference frame and S is a state scaling matrix used in order to remove the dimensions from the state vector in body reference frame.

$$x = S^{-1}\left(x_B - x_{B_{trim}}\right) \tag{221}$$

$$x_B = \begin{bmatrix} u & v & w & p & q & r & X & Y & Z & \phi & \theta & \psi \end{bmatrix}^T \tag{222}$$

Then, based on the definition of the linear approximation for the nonlinear model, a inertial frame dynamics field is defined, as shown in equation (223). Where L_{IB} is the transformation matrix from body axes to inertial axes, in this case calculated using the pseudocommand angles calculated in equation (220). F is the stability derivative matrix of the helicopter for the flight condition. The F matrices for both flying conditions were the result of a linearization process for hover and a forward flight condition of 20 ft/s.

$$f\left(\bar{x}\right) = \left[\dot{L}_{IB}\left(\bar{x}\right)S + L_{IB}\left(\bar{x}\right)SF\right]x + \dot{L}_{IB}\left(\bar{x}\right)x_{B_{trim}} \tag{223}$$

The inertial frame control matrix is defined as shown in equation (224), where G is the control derivative matrix. In a similar way as for the F matrix, G matrices for each flying condition were obtained by linearizing the nonlinear helicopter model.

$$g\left(\bar{x}\right) = L_{IB}\left(\bar{x}\right)SG \tag{224}$$

Then, the increase over the trim value for the collective can be calculated using terms from the inertial frame dynamics field and the inertial frame control matrix as shown in equation (225); where the subscripts indicate the vector or matrix position of the element in the dynamics and control field respectively.

$$\delta_{coll} = \frac{\upsilon_3 - f_3\left(\bar{x}\right)}{g_{33}\left(\bar{x}\right)} \tag{225}$$

Now that the outer loop has been calculated, the inner loop is next. First, the inner loop dynamic field $f_I(x)$ is calculated as follows:

$$f_I\left(x\right) = \begin{bmatrix} f_4\left(x\right) + g_{43}\left(x\right)\delta_{coll} \\ f_5\left(x\right) + g_{53}\left(x\right)\delta_{coll} \\ f_6\left(x\right) + g_{63}\left(x\right)\delta_{coll} \end{bmatrix} \tag{226}$$

and the inner control loop matrix is defined as:

$$g_I\left(x\right) = \begin{bmatrix} g_{41}\left(x\right) & g_{42}\left(x\right) & g_{44}\left(x\right) \\ g_{51}\left(x\right) & g_{52}\left(x\right) & g_{54}\left(x\right) \\ g_{61}\left(x\right) & g_{62}\left(x\right) & g_{64}\left(x\right) \end{bmatrix} \tag{227}$$

Hence, the inner loop pseudocontrol can be calculated as shown in equation (228).

$$\upsilon_I = \begin{bmatrix} 1 & \sin\phi\tan\theta & \cos\phi\tan\theta \\ 0 & \cos\phi & -\sin\phi \\ 0 & \sin\phi\sec\theta & \cos\phi\sec\theta \end{bmatrix} \omega_c + \begin{bmatrix} \dot{\psi}\dot{\theta}\sec\theta + \dot{\theta}\dot{\phi}\tan\theta \\ -\dot{\psi}\dot{\phi}\cos\theta \\ \dot{\theta}\dot{\phi}\sec\theta + \dot{\psi}\dot{\theta}\tan\theta \end{bmatrix} \quad \textbf{(228)}$$

Now, the inner loop inversion can be formulated, as shown in equation (224), where $u_I=[\delta_{lat}\ \delta_{long}\ \delta_{ped}]^T$.

$$u_I = g_I^{-1}\left(\upsilon_I - f_I\left(x\right)\right) + u_{I_{trim}} \quad \textbf{(229)}$$

The individual blade control law is then defined as shown in equation (230).

$$\theta ft_i = \delta_{coll} - \delta_{lat}\cos\psi_i - \delta_{long}\sin\psi_i \quad \textbf{(230)}$$

5.2.2.2 Linearizing Transformation

Consider a nonlinear system defined by equation (231).

$$\ddot{y} = f\left(y, \dot{y}, \delta\right) \quad \textbf{(231)}$$

Where y(t) and its derivative are the state variables of the system with n degrees of freedom, and δ(t) are the inputs. All of them are vectors belonging to R^n. For practical reasons a pseudocontrol variable is defined in equations (232) and (233).

$$\ddot{y} = U_s \quad \textbf{(232)}$$

$$U_s = f\left(y, \dot{y}, \delta\right) \quad \textbf{(233)}$$

Then, if *f* is invertible, then the control inputs δ can be obtained from the states as shown in equation (234).

$$\delta = f^{-1}\left(y, \dot{y}, U_s\right) \quad \textbf{(234)}$$

The inverse of the model in this case will be the inverse of a linear model of the helicopter based on the nonlinear one for a specific trim condition. Thus, the inverse is only approximate, which results in the control law described in equation (235).

$$\hat{\delta} = \hat{f}^{-1}\left(y, \dot{y}, U_s\right) \quad \textbf{(235)}$$

Then, the closed-loop dynamics can be represented as shown in equation (236).

$$\ddot{y} = U_s + \chi\left(y, \dot{y}, U_s\right) \quad \textbf{(236)}$$

Where the function χ represents the inversion error and is defined in equation (237).

$$\chi\left(y, \dot{y}, U_s\right) = f\left(y, \dot{y}, \hat{\delta}\right) - \hat{f}\left(y, \dot{y}, \hat{\delta}\right) \quad \textbf{(237)}$$

5.2.2.3 Neural Network Based Adaptive Control

The adaptive control architecture is chosen as described by equation (238).

$$U_s(t) = U_{pd}(t) + \ddot{y}_c(t) - U_{ad}(t) \quad \textbf{(238)}$$

Where U_{pd} is a proportional and derivative control law used to shape the response of the system, y_c is the commanded acceleration vector and U_{ad} is the adaptive signal generated by the neural networks, whose purpose is to cancel out the inversion error. The control law defining U_{pd} is shown in equation (239).

$$U_{pd} = K_p(y_c - y) + K_d(\dot{y}_c - \dot{y}) \quad \textbf{(239)}$$

The tracking error for the system can be defined as shown in equation (240) and since χ is defined as the inversion error, the performance of the neural network can be estimated by the calculation of the value of U_{ad}-χ. This term will be used as one of the parameters to evaluate the performance of the different helicopter architectures: classic, swashplate and IBC, and swashplateless. A diagram describing the controller architecture is shown in Figure 83.

$$\dddot{\tilde{y}} + K_d\ddot{\tilde{y}} + K_p\dot{\tilde{y}} = U_{ad} - \chi \quad \textbf{(240)}$$

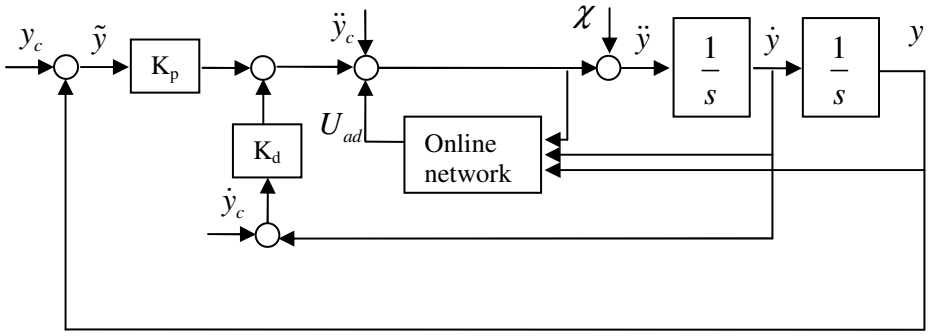

Figure 83 Interface of neural network within inner loop controller structure

5.2.2.4 Nominal Controller Synthesis

Since the plant to be controlled is a helicopter, a controller will be put in place to stabilize the rotational dynamics of the helicopter itself. In this case, the collective input will be analyzed as a slow variable in the control law and decoupled from the moment equations. The controls for the rotational variables are lateral and longitudinal cyclic stick inputs and pedal inputs for the classic swashplate configuration; in the case of the swashplate with individual blade control, the inputs are the same plus the additional input for each blade actuator; and finally in the case of the swashplateless architecture, with full IBC authority, the inputs are each of the blade actuators.

For the last two, the virtual swashplate approach will be used to translate inputs from cyclics to inputs to each of the blade actuators.

In terms of individual loops, the signal U_s is composed of each of the scalar signals shown in equations (241) to (242).

$$U_\phi = K_{p\phi}\left(\phi_c - \phi\right) + K_{d\phi}\left(\dot{\phi}_c - \dot{\phi}\right) + \ddot{\phi}_c - U_{ad\phi} \tag{241}$$

$$U_\theta = K_{p\theta}\left(\theta_c - \theta\right) + K_{d\theta}\left(\dot{\theta}_c - \dot{\theta}\right) + \ddot{\theta}_c - U_{ad\theta} \tag{242}$$

$$U_\psi = K_{p\psi}\left(\psi_c - \psi\right) + K_{d\psi}\left(\dot{\psi}_c - \dot{\psi}\right) + \ddot{\psi}_c - U_{ad\psi} \tag{243}$$

The dynamics for the Euler angles in the transformed system are specified by the proportional and derivative gains for each angular attitude angle according to equation (240).

5.2.2.5 Rotational Dynamics Inversion

The body axis rotational dynamics based on the linearized aerodynamics, is shown in equation (244), where ω is the body angular velocity vector consisting of the angular rates p, q, and r, $f(\omega)$ represents the inertial nonlinear moment terms, z is the vector of translational states and the collective variable (u,v,w,δ_{col}), and η is the vector of moment controls (δ_{lat}, δ_{long}, δ_{ped}). Δ represents perturbations from trim value. The NLDI and CC subscripts account for the corresponding moments generated by each loop, the classic controller (CC) and the nonlinear dynamic inversion (NLDI).

$$\dot{\omega} = A_1 \Delta z + A_2 \omega + B\left(\Delta\eta_{CC} + \Delta\eta_{NLDI}\right) + f\left(\omega\right) \tag{244}$$

Then, the model inversion control law gives the required perturbation controls, as shown in equation (245), where the body axis pseudocontrols ω_c are calculated by transforming the vector U_s from the Euler rates into the body frame angular rates.

$$\Delta\eta_{NLDI} = B^{-1}\left\{\dot{\omega}_c - A_1\Delta z - A_2\omega - f\left(\omega\right) - B\Delta\eta_{CC}\right\} \tag{245}$$

In terms of the individual angular rate components, the terms are described in equations (246) to (248), where the rates and angular accelerations are shown.

$$\dot{p}_c = U_\phi - U_\psi \sin\theta - \dot{\psi}\dot{\theta}\cos\theta \tag{246}$$

$$\dot{q}_c = U_\theta \cos\phi - \dot{\theta}\dot{\phi}\sin\phi + U_\psi \sin\phi\cos\theta + \dot{\psi}\dot{\phi}\cos\phi\cos\theta - \dot{\psi}\dot{\theta}\sin\phi\sin\theta \tag{247}$$

$$\dot{r}_c = -U_\theta \sin\phi - \dot{\theta}\dot{\phi}\cos\phi + U_\psi \cos\phi\cos\theta + \dot{\psi}\dot{\phi}\cos\phi\cos\theta - \dot{\psi}\dot{\theta}\sin\phi\sin\theta \tag{248}$$

The commanded rates and accelerations needed in equations (246) to (248) can be generated by filtering the commanded positions y_c using a second order filter as shown in Figure

84. It is to be noted that since only the rotational dynamics are included, for the system to be fully stable an additional outer loop to stabilize the translational dynamics is required.

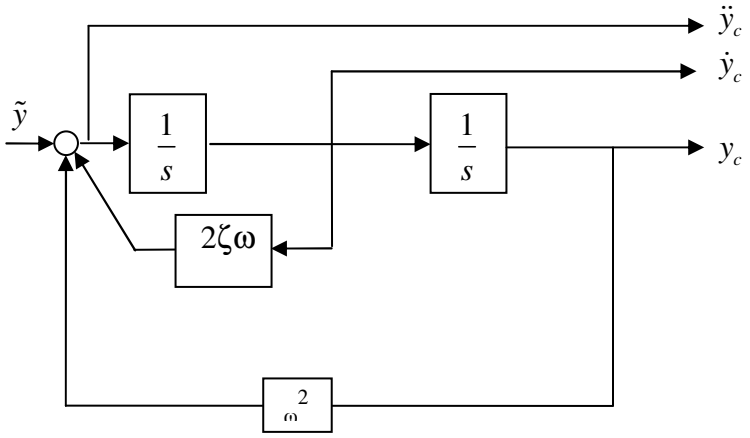

Figure 84 Command filter simulation diagram

5.2.2.6 Analysis of the Inversion Error

In the rotational dynamics inversion section, the dynamic control laws were developed based on the assumption of linear aerodynamics. For this assumption to be realistic, the stability and control matrices must change depending on the flight conditions from one trim condition to another. Thus a dynamic trim map is produced, representing the changes in the aerodynamics, based on th assumption that these quantities depend approximately on a polynomial function of forward and sideward velocities U and V as defined in equations (249) and (250), where the derivative of X and Y are the inertial northbound and eastbound speeds respectively, and ψ is the heading of the helicopter.

$$U = \dot{X}\cos\psi + \dot{Y}\sin\psi \quad \textbf{(249)}$$

$$V = -\dot{X}\sin\psi + \dot{Y}\cos\psi \quad \textbf{(250)}$$

A neural network will then be used to not having to schedule the stability and control matrices, and the state control trim values as functions of U and V, as well as to account for unmodeled variations in the dynamics, such as the failures. Thus the equation (244) can be rewritten as shown in equation (251).

$$\dot{\omega} = \left[\bar{A}_1 + \delta A_1 (U,V) \right] \Delta z + \left[\bar{A}_2 + \delta A_2 (U,V) \right] \omega + \left[B + \delta B (U,V) \right] \Delta \eta \tag{251}$$

$$\Delta z = \Delta \hat{z} - \delta z_{trim} (U,V) \tag{252}$$

$$\Delta \eta = \Delta \hat{\eta} - \delta \eta_{trim} (U,V) \tag{253}$$

The nominal control laws are based in equation (244), and the perturbation quantities in state and control are based on a nominal trim condition; therefore, Δz and $\Delta \eta$ can be approximated as shown in equations (254) through (256), where z_{trim} and η_{trim} are constant vectors that represent state and control trim values at the nominal flight condition.

$$\Delta \hat{z} = z - z_{trim} \tag{254}$$

$$\Delta \hat{\eta} = \Delta \hat{\eta}_{NLDI} + \Delta \hat{\eta}_{CC} \tag{255}$$

$$\Delta \hat{\eta}_{NLDI} = \bar{B}^{-1} \left\{ \dot{\omega}_c - \bar{A}_1 \Delta \hat{z} - \bar{A}_2 \omega - B \Delta \hat{\eta}_{CC} \right\} \tag{256}$$

The δ terms in equation (251) represent the variations of the stability and control matrices at trim as the flight condition changes. Applying the control law in equation (256) to the perturbed equations of motion in equation (251), the closed loop dynamics of the whole system can be found as described in equation (257).

$$\begin{aligned} \dot{\omega} = \dot{\omega}_c + \left[\delta A_1 - \delta B \bar{B}^{-1} \bar{A}_1 \right] \Delta \hat{z} + \left[\delta A_2 - \delta B \bar{B}^{-1} \bar{A}_2 \right] \omega + \delta B \bar{B}^{-1} \dot{\omega}_c - \bar{A}_1 \delta z_{trim} \\ - \bar{B} \delta \eta_{trim} - \delta A_1 \delta z_{trim} - \delta B \delta \eta_{trim} \end{aligned} \tag{257}$$

Equation (230) will be rewritten in a shorter form for convenience as shown in equation (258), and the term $\tilde{\dot{\omega}}$ will be known as the inversion error, because if this term is zero the inversion is perfect.

$$\dot{\omega} = \dot{\omega}_c + \tilde{\dot{\omega}} \tag{258}$$

Since the desired trajectories are Euler angles and angular rates, it is better to show equation (258) using Euler angles and Euler angular rates instead of of body axes angular rates, thus if we define the Euler angles as a vector $y=\{\varphi,\theta,\psi\}$, the body axis angular accelerations can be transformed into Euler angle second derivatives using equation (259), and in a similar way the commanded accelerations can be transformed using equation (260), where $L(\varphi,\theta)$ is shown in equation (261) and g is shown in equation (262).

$$\ddot{y} = L(\phi,\theta) \dot{\omega} + g(y, \dot{y}) \tag{259}$$

$$U_s = L(\phi,\theta) \dot{\omega}_c + g(y, \dot{y}) \tag{260}$$

$$L(\phi,\theta) = \begin{bmatrix} 1 & \sin\phi \tan\theta & \cos\phi \tan\theta \\ 0 & \cos\phi & -\sin\phi \\ 0 & \sin\phi \sec\theta & \cos\phi \sec\theta \end{bmatrix} \tag{261}$$

$$g\left(y,\dot{y}\right)=\begin{bmatrix}\dot{\psi}\dot{\theta}\sec\theta+\dot{\theta}\dot{\phi}\tan\theta\\ -\dot{\psi}\dot{\phi}\cos\theta\\ \dot{\theta}\dot{\phi}\sec\theta+\dot{\psi}\dot{\theta}\tan\theta\end{bmatrix} \tag{262}$$

Assuming that the pitch attitude angle will not be 90°, we can plug in equations (259) and (260) in equation (258), to obtain the equation (263), which then can be reduced to equation (264), and the Euler angle definition for the inversion error can be obtained as shown in equation (265).

$$L^{-1}\left(\phi,\theta\right)\left[\ddot{y}-g\left(y,\dot{y}\right)\right]=L^{-1}\left(\phi,\theta\right)\left[U_s-g\left(y,\dot{y}\right)\right]+\tilde{\dot{\omega}} \tag{263}$$

$$\ddot{y}=U_s+L\left(\phi,\theta\right)\tilde{\dot{\omega}} \tag{264}$$

$$\chi=L\left(\phi,\theta\right)\tilde{\dot{\omega}} \tag{265}$$

This inversion error is characterized by terms that include a bilinear contribution of δA_1, δA_2, and δB; terms that include a bilinear contribution from $\Delta\hat{z}$, ω, and $\dot{\omega}_c$; terms that are linear in δz_{trim}, $\delta\eta_{trim}$; products of δ quantities; and terms that include a bilinear contribution from each element of $L\left(\phi,\theta\right)$.

5.2.2.7 Development of the Neural Network Equations

The neural network architecture is based on the Sigma-Pi architecture, as described by Zhang et al[64]. Equation (240) will be re-written so it can be used for the different attitude angles φ, θ, and ψ as shown in equation (266), where a subscript i is put in place for each of these attitude angles, and the term $U_{ad_i}-\chi_i$ will be known from now on as the adjusted inversion error.

$$\dddot{\tilde{y}}_i+K_{d_i}\ddot{\tilde{y}}_i+K_{p_i}\dot{\tilde{y}}_i=U_{ad_i}-\chi_i \tag{266}$$

Then, equation (266) can be re-written for convenience in state space form. Each of the channels assigned to each of the attitude angles will have a second order error dynamics. The i subscripts will be dropped for convenience, as shown in equation (267).

$$\dot{e}=Ae+b\left(U_{ad_i}-\chi\right) \tag{267}$$

The error e, the matrix A, and the variable b are defined as shown in equations (268) to (270).

$$e = \begin{bmatrix} \tilde{y} & \dot{\tilde{y}} \end{bmatrix}^T \tag{268}$$

$$b = \begin{bmatrix} 0 & 1 \end{bmatrix}^T \tag{269}$$

$$A = \begin{bmatrix} 0 & 1 \\ -K_p & -K_d \end{bmatrix} \tag{270}$$

Then, the adaptive control law in each of the channels for the attitude angles can be defined as described in equations (271) and (272), where the vector g is a set of basis functions used to approximate the uncertainty and the vector w is the set of coefficients for each basis function.

$$U_{ad_i} = w^T g \tag{271}$$

$$\dot{w} = -ksg \tag{272}$$

The update law is designed based on the Lyapunov stability of the error signals, and the s term is an error metric dependent on the tracking errors for the helicopter system, as described in equation (273). For equation (273) λ is defined in terms of the Lyapunov equation used to prove the stability that will be described further on.

$$s = \left(\frac{1}{2K_p} \right) \tilde{y} + \left(\frac{1}{2\lambda K_p} \right) \dot{\tilde{y}} \tag{273}$$

Now, it is assumed that an optimal vector of weights (w^*), exists for each channel, then ŵ presented in equation (274) can be calculated as the difference between the actual weights and the optimal set of weights.

$$\tilde{w} = w - w^* \tag{274}$$

This approach allows for equation (267) to be written as described in equation (275).

$$\dot{e} = Ae + b\tilde{w}^T g + b\left(w^{*T} g - \chi \right) \tag{275}$$

And if ∈ is defined as the bound on the residual inversion error that is unmodeled by the neural network, as described in equation (276). In that same equation the vector ρ is defined by the composition of all the independent variables of the inversion error. Thus equation (276) in essence, represents the worst case difference between the inversion error for the given set of network inputs. Then it is assumed that a fixed point solution exists, and thus U_{ad} exists.

$$\in \equiv \sup_{\rho} \left| w^{*T} g(\rho) - \chi(\rho) \right| \tag{276}$$

5.2.2.8 Neural Network Structure

The structure of the neural network is aimed, as described previously, to reconstruct the inversion error. Based on the analysis of the error, a vector of basis functions g is defined as shown in equation (277).

$$g = kron\left[kron\left(C_1, C_2\right), C_3 \right] \tag{277}$$

Where C_1, C_2, and C_3, are vectors cotaining the values for the variables found in the previous chapter as the sources for the inversion error. The variables are described in equations (278) to (280) and are normalized so they range from -1 to 1.

$$C_1 = \left\{1, \bar{U}, \bar{V}, \bar{U}^2, \bar{V}^2, \bar{U}\bar{V}, \bar{U}^2\bar{V}, \bar{U}\bar{V}^2, \bar{U}^2\bar{V}^2\right\} \tag{278}$$

$$C_2 = \left\{1, \Delta\bar{u}, \Delta\bar{v}, \Delta\bar{w}, \Delta\bar{\delta}_{coll}, \bar{p}, \bar{q}, \bar{r}, \dot{p}_c, \dot{q}_c, \dot{r}_c\right\} \tag{279}$$

$$C_3 = \left\{1, \sin\phi\tan\theta, \cos\phi\tan\theta, \cos\phi, \sin\phi, \sin\phi\sec\theta, \cos\phi\sec\theta\right\} \tag{280}$$

The selection of the previous structure was based on the analysis of the inversion error presented in section 5.2.2.6 of this chapter. The selected structure is not unique, and can be tuned by adding variables that are sources of inversion error.

5.2.3 Stability Analysis

The analysis is based on Lyapunov's direct method for determining stability[65]. In this approach a Lyapunov function candidate V is defined for each of the channels, then using this function, a solution for the Lyapunov equation is found and specific characteristics for the neural network are defined such that the system is stable Since the operation of each of the attitude channels is the same, this analysis can be done for each of the channels indistinctively. Thus the functional form can be written as shown in equation (281), where e_c is a vector in R^2 that satisfies $\sqrt{(e_c^T P e_c)} = e_0$, which ensures the continuity of V across the radial boundary defined by e_0. V_p is defined as shown in equation (282).

$$V = \begin{cases} V_p(e) + \dfrac{\tilde{w}^T \tilde{w}}{2\gamma} & \text{when} \quad \sqrt{e^T P e} > e_0 \\ V_p(e_c) + \dfrac{\tilde{w}^T \tilde{w}}{2\gamma} & \text{when} \quad \sqrt{e^T P e} \le e_0 \end{cases} \tag{281}$$

$$V_p(e) = \frac{1}{2} e^T P e \qquad \text{with } P > 0 \tag{282}$$

Thus, the time derivative of the candidate Lyapunov function, for $\sqrt{(e_c{}^T P e_c)} > e_0$ is given by equation (283).

$$\dot{V} = \frac{1}{2}\dot{e}^T P e + \frac{1}{2} e^T P \dot{e} + \frac{\tilde{w}^T \dot{\tilde{w}}}{\gamma} \tag{283}$$

Then, substituting equation (275) in equation (283) this results in equation (284).

$$\dot{V} = \frac{1}{2} e^T A^T P e + \frac{1}{2} e^T P A e + \left\{ \tilde{w}^T g + \left(w^{*T} g - \chi \right) \right\}^T b^T P e + e^T P b \left\{ \tilde{w}^T g + \left(w^{*T} g - \chi \right) \right\} + \frac{1}{\gamma} \tilde{w}^T \dot{\tilde{w}} \tag{284}$$

Now, since A is a Hurwitz matrix[65] a symmetric positive definite solution P, to the Lyapunov equation exists as shown in equation (285), where Q is a symmetric positive definite matrix.

$$PA + A^T P = -Q \tag{285}$$

Thus, equation (284) becomes the equation (286), as shown as follows:

$$\dot{V} = -\frac{1}{2} e^T Q e + e^T P b \tilde{w}^T g + e^T P b \left(w^{*T} g - \chi \right) + \frac{1}{\gamma} \tilde{w}^T \dot{\tilde{w}} \tag{286}$$

And since $e^T Pb$ is a scalar quantity, equation (286) can be easily modified so that equation (287) is obtained.

$$\dot{V} = -\frac{1}{2} e^T Q e + e^T P b \left(w^{*T} g - \chi \right) + \tilde{w}^T \left\{ e^T P b g + \frac{1}{\gamma} \tilde{w}^T \dot{\tilde{w}} \right\} \tag{287}$$

Then if the update law is chosen as shown in equation (288), and plugged into equation (287), equations (289) to (292) are obtained.

$$\dot{w} = \dot{\tilde{w}} = -\gamma e^T Pbg \tag{288}$$

$$\dot{V} = -\frac{1}{2} e^T Qe + e^T Pb\left(w^{*^T} g - \chi \right) \tag{289}$$

$$\therefore \dot{V} \le -\frac{1}{2} e^T Qe + \left| e^T Pb \right| \left| w^{*^T} g - \chi \right| \tag{290}$$

$$\therefore \dot{V} \le -\frac{1}{2} e^T Qe + \in \left| e^T Pb \right| \tag{291}$$

$$\therefore \dot{V} \le -\frac{1}{2} \|e\|_2^2 \lambda_{\min}(Q) + \in \left| e^T Pb \right| \tag{292}$$

And since,

$$e^T Pe \le \lambda_{\max}(P) \|e\|_2^2 \tag{293}$$

Then, that allows that equation (292) can be rewritten as shown in equation (294) to equation (297).

$$\dot{V} \le -\frac{1}{2} \frac{e^T Pe}{\lambda_{\max}(P)} \lambda_{\min}(Q) + \in \left| e^T Pb \right| \tag{294}$$

$$\therefore \dot{V} \le -\frac{1}{2} \frac{e^T Pe}{\lambda_{\max}(P)} \lambda_{\min}(Q) + \in \left| e^T \sqrt{P} \right| \left| \sqrt{P} b \right| \tag{295}$$

$$\therefore \dot{V} \le -\frac{1}{2} \frac{e^T Pe}{\lambda_{\max}(P)} \lambda_{\min}(Q) + \in \sqrt{\left| e^T \sqrt{P} \right| \left| \sqrt{P} e \right|} \left| \sqrt{P} b \right| \tag{296}$$

$$\therefore \dot{V} \le -\frac{1}{2} \frac{e^T Pe}{\lambda_{\max}(P)} \lambda_{\min}(Q) + \in \sqrt{e^T Pe} \sqrt{\lambda_{\max}(P)} \tag{297}$$

Then, since the derivative of the Lyapunov function is negative when

$$\sqrt{e^T Pe} > \frac{2 \in \lambda_{\max}(P)^{\frac{3}{2}}}{\lambda_{\min}(Q)} \equiv e_0 \tag{298}$$

Thus, the boundedness is guaranteed for the region where $\sqrt{(e^T Pe)} > e_0$ because V is strictly positive, strictly increasing the function of e and $\tilde{w}$. Thus the update laws can be defined assuming that Q is defined as shown in equation (299).

$$Q = \begin{bmatrix} q & 0 \\ 0 & 1 \end{bmatrix} \tag{299}$$

And then, the solution to equation (285) can be found as defined in equation (300).

$$P=\begin{bmatrix}\left(\frac{K_d}{2K_p}+\frac{1}{2K_d}\right)q+\frac{K_p}{2K_d} & \frac{q}{2K_p}\\ \frac{q}{2K_p} & \frac{q+K_p}{2K_pK_d}\end{bmatrix} \tag{300}$$

Thus, equation (274) can be rewritten as shown in equation (301), and λ can be defined as shown in equation (302).

$$\dot{w}=\gamma\left(\frac{q}{2K_p}\tilde{y}+\frac{q+K_p}{2K_dK_p}\dot{\tilde{y}}\right)g \tag{301}$$

$$\lambda=\frac{K_dq}{\left(q+K_p\right)} \tag{302}$$

And since q has to be positive, this immediately implies that $0<\lambda<K_d$, and from that it can be implied that the value of k can be calculated as shown in equation (303).

$$k=\gamma q \tag{303}$$

Now, a value of λ must be chosen so that it gives a minimum dead zone, thus it is needed to minimize the expression for e_0. For simplicity, the values that minimize the ratio $\lambda_{max}(P)/\lambda_{min}(Q)$ are chosen, which then turns into giving Q equal to the identity matrix or q=1. Thus, λ is chosen as shown in equation (304).

$$\lambda=\frac{K_d}{\left(1+K_p\right)} \tag{304}$$

Now, if in case that the tracking error moves within the boundary defined by e_0, the derivative of the Lyapunov function is defined as shown in equation (305). For which the only choice is to set the derivatives of the weights to zero, $\dot{w}=\dot{\hat{w}}=0$, for which there is no more learning and the system has reached a steady state for the adaptation. The previous assumption implies, that according to equation (305). $\dot{V}=0$ when $e^TPe<e_0$. Thus, for global stability, a dead zone of radius e_0 is required so the adaptation is not being updated with time, which then implies that a set of basis functions are capable of cancelling the inversion error. However, even though the stability of the system is guaranteed no matter which structure of functions is selected, a wrong choice in this structure of functions, would entail a radius of e_0 reasonably large. Thus a good structure is needed so the work performed by the neural networks to reconstruct the inversion error is kept to a minimum.

$$\dot{V} = \frac{\dot{\tilde{w}}^T \tilde{w}}{\gamma} \tag{305}$$

According to the previous stability analysis a value of λ was chosen to be 1.998. Hence, values for K_p and K_d were set at 0.0001 and 2 respectively for all rotational states. Calculations were performed using equation (304). Also a learning rate k of 0.001 was set for the basis functions.

5.2.4 Pseudo Control Hedging

One of the main concerns regarding adaptive control schemes is the issue of saturation, even more so than for non-adaptive control. One method to prevent saturation in adaptive schemes, especially for those schemes that use neural networks, is Pseudo Control Hedging[66] (PCH). This technique allows for the reduction of saturation by creating a safety band close to saturation of the control. Once the plant goes inside this safety band, the difference between the set point and the threshold value for the safety band, is calculated. Using this difference, the effects on the rotational accelerations can be found (using the control derivatives) and then substract those from the commanded moments. The procedure is presented in the schematic shown in Figure 85.

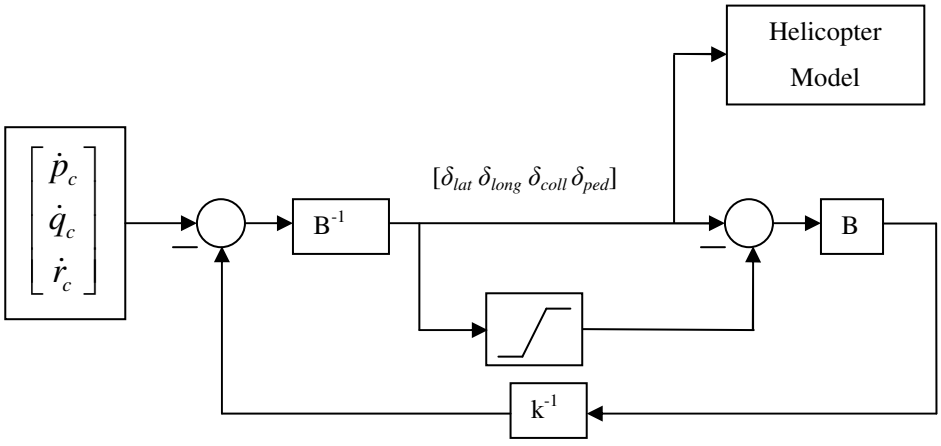

Figure 85 General diagram of the pseudo control hedging scheme

According to this diagram a PCH scheme was implemented for the rotational dynamics of the helicopter. Minimum and maximum values for the safety band are listed in Table 20.

Table 20 PCH parameters

Control	Min	Max
$\delta_{lateral}$	-1.4	0.3
$\delta_{longitudinal}$	-6	3
$\delta_{collective}$	-8.8	2.7
δ_{pedals}	-5.2	4.1

5.2.5 General Controller Architecture

A general diagram of the implemented controller scheme is presented in Figure 86. Inputs from the nonlinear dynamic inversion augmented with neural network compensation are added to the classic control architecture and the UH60 stability augmentation system. These inputs are then fed to the individual control scheme which then translates each of the inputs, except for the pedals, into blade angles for each of the blades. The individual blade control scheme itself contains the failure accommodation scheme presented in this chapter.

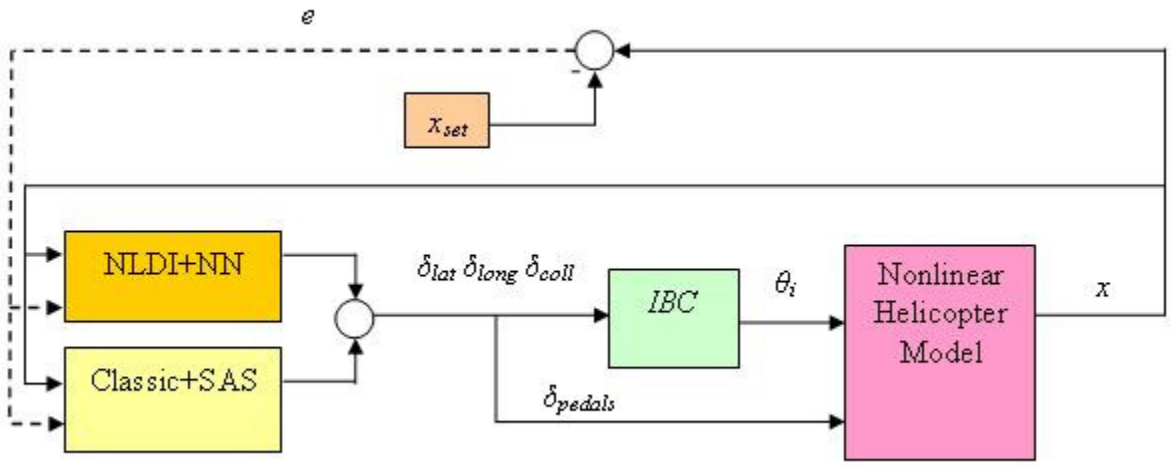

Figure 86 General diagram of the control scheme

6 Analysis of Controller Performance

A series of tests are executed in order to evaluate the performance of the controller, and are shown in this chapter. These tests include different architectures, failures, and flight conditions. A comparative analysis including the different architectures, classic swashplate, classic swashplate and individual blade control, and swashplateless will be done in order to confirm the ability of individual blade control to improve the fault tolerant characteristics of a helicopter.

6.1 Simulation Tests:

6.1.1 Nominal Conditions

As a benchmark, the nominal conditions for the architecture are shown for hover and a forward flight condition of 20 ft/s. Hover response after a step input are shown in Figure 87 through Figure 92.

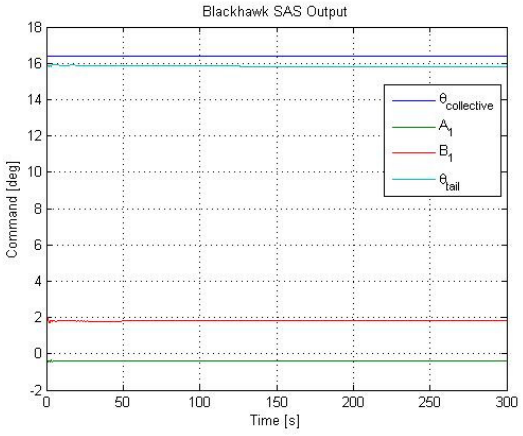

Figure 87 Actual main rotor command at hover

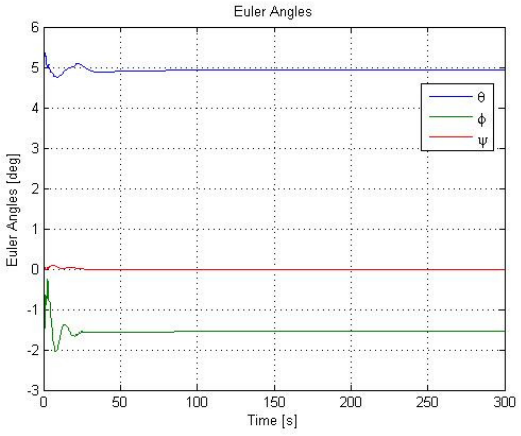

Figure 88 Euler angles at hover

After a initialization process for the states in the helicopter is performed, the classic control takes over from a defined set of initial conditions. In order to avoid initialization issues, after a 10 second period the loop containing the neural networks is habilitated, and after a 20 second period the NLDI and neural network scheme is habilitated as an input to the helicopter main scheme. As a result of this, small variations of the input can be observed for the first 30 second period, after which the transitory starts to attenuate, obtaining the hover condition around the 100 second mark, as can be seen in Figure 89. After this, the attitude of the helicopter is firmly set for a 4.9 deg in pitch and -1.5 deg in roll, as shown in Figure 88. Harmonic variation

of the blade pitch angle according to the azimuth angle can be observed in Figure 90, with the variation ranging from 14.7 deg to 18.2 deg.

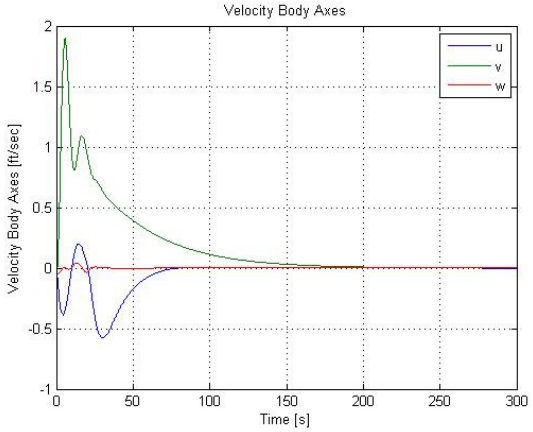

Figure 89 Body axes velocity at hover

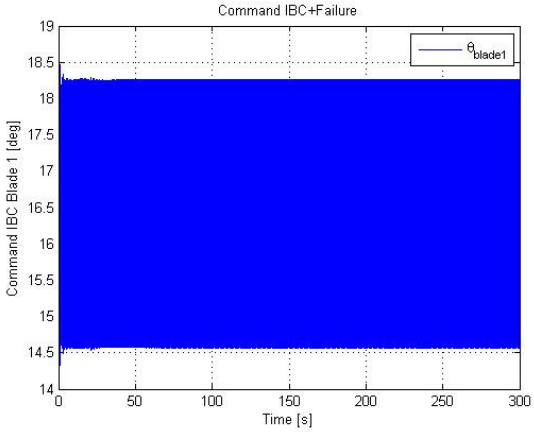

Figure 90 Blade #1 pitch angle at hover

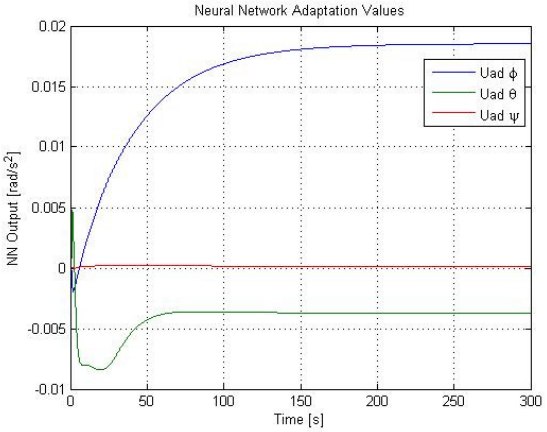

Figure 91 Adaptive output at hover

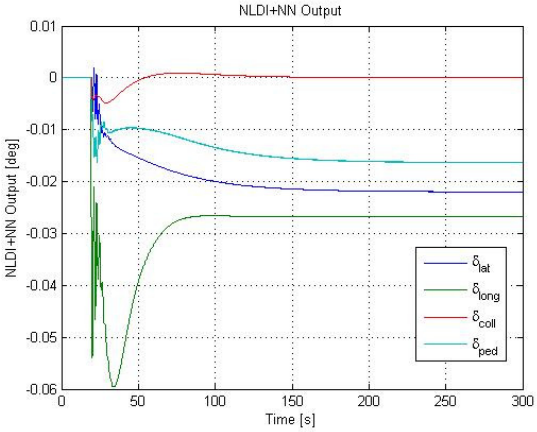

Figure 92 NLDI+NN output at hover

A forward flight condition is discussed next. The forward flight speed has been selected to be 20 ft/s, and its simulation results are shown in Figure 93 through Figure 98. In a similar way as for the hover condition, an initialization process has been performed. In this case the neural networks are included in the loop after a 12 second period and the NLDI is habilitated after a 10 second period.

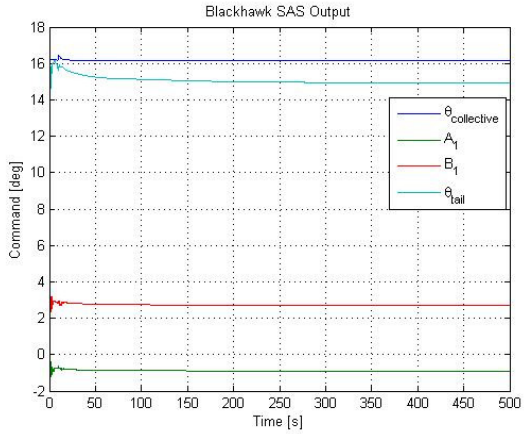

Figure 93 Actual main rotor command in forward flight

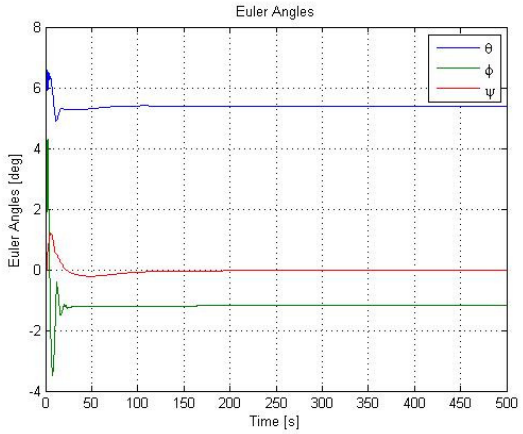

Figure 94 Euler angles in forward flight

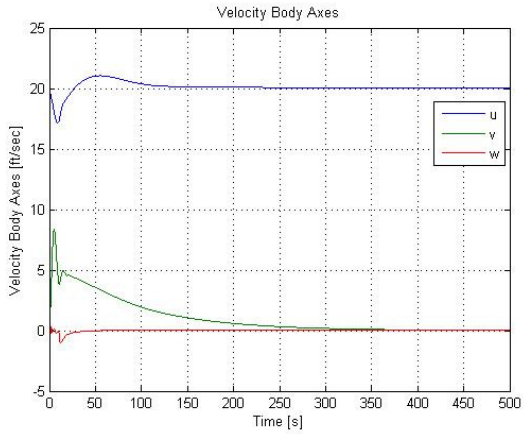

Figure 95 Body axes velocity in forward flight

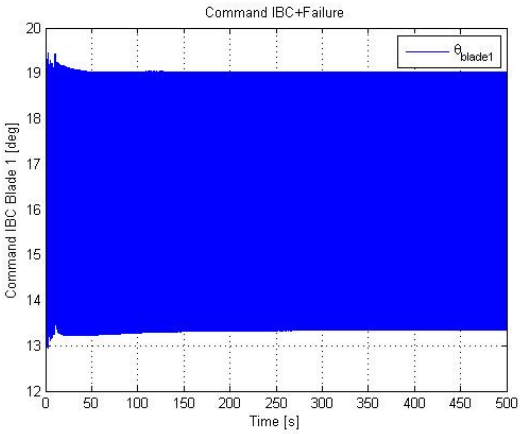

Figure 96 Blade #1 pitch angle in forward flight

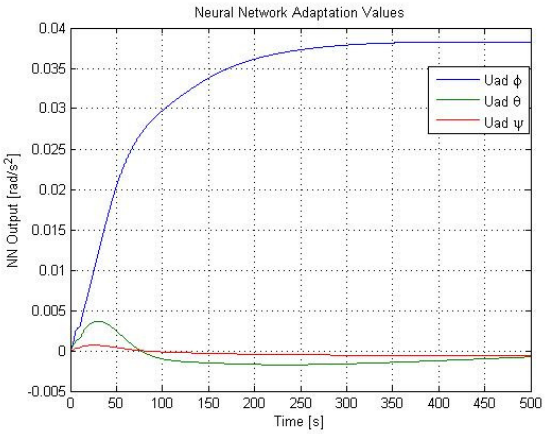

Figure 97 Adaptive output in forward flight

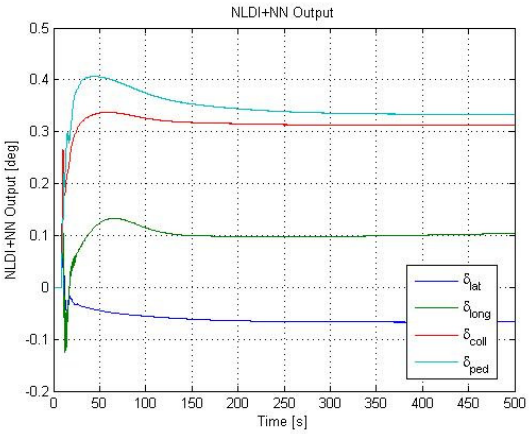

Figure 98 NLDI+NN output in forward flight

In a similar way as the hover case, the forward flight has a transitory period within each of the controlled and control variables are stabilized and eventually find their respective trim condition. As said before the forward flight condition of 20 ft/s has been established, and said

value can be observed clearly in Figure 95. Attitude for this trim condition occurs at a roll angle of -1.2 deg and a pitch angle of 5.4 deg, as shown in Figure 94.

Having shown the nominal cases, it is to be noted that the closed loop performance of the classic and NLDI controller was tuned in such a way that the response of the helicopter to perturbations, would be as smooth as possible. This characteristic was required in order to have an appropriate initialization of the online neural network that accompanies the nonlinear dynamic inversion. Hence, the response of the helicopter to initialization takes a relative long period of time. Furthermore, it is important to state that, under nominal conditions, all architectures show an equivalent performance of the helicopter, given that neither the trim attitude nor the velocity change no matter which particular controller or helicopter architecture is used.

6.1.2 Classic Swashplate Architecture

This configuration uses the classic swashplate architecture, for which a mechanical swashplate is changed in orientation by the lateral and longitudinal cyclics, and additional lift is generated using the collective. Since the physical architecture does not include the individual blade control, the associated individual blade controller is not used, however, the nonlinear dynamic inversion augmented with neural networks and the classic control architecture are used in order to fully assess the impact of the individual blade control as stability augmentation technique.

Tests were carried out for hover and a forward flight speed of 20 ft/s, and failures consisted of locked actuator were induced for the lateral and longitudinal cyclic and collective actuators as specific moments in time. Unless specified, the tests will be carried out so no delay and no bias are included in the simulations.

A failure on the lateral actuator is presented in Figure 99 through Figure 101 for the hover flight condition. The failure is induced after a period of 110 seconds after a step input is applied. In this case the lateral actuator is taken from the trim condition to a value of -0.5 degrees, with a first order transition time with a time constant of 1 second. As can be seen in Figure 100, the effect of the failure is immediate for the Euler angles, especially for the roll angle, as it is to be expected given that the failure occurs in this particular channel. Also, there is an immediate effect on the lateral velocity, and in a similar way it can be inferred that the helicopter turns unstable for this particular set of failure parameters.

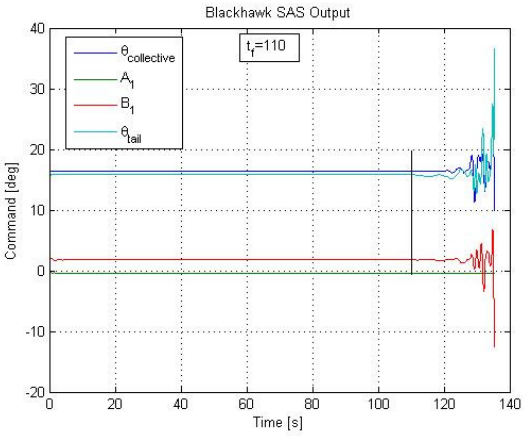

Figure 99 Actual main rotor command with failure at hover

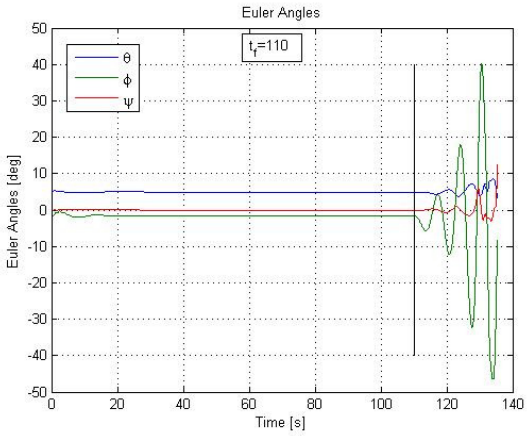

Figure 100 Euler angles lateral failure at hover

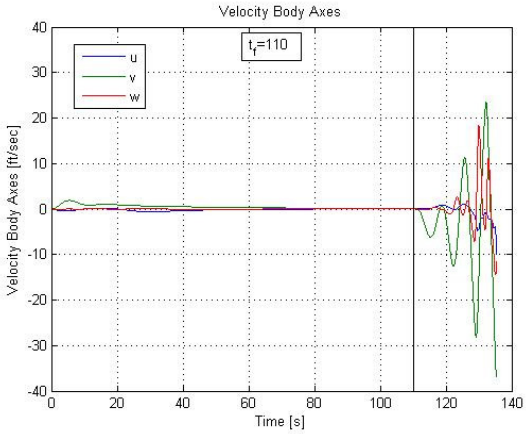

Figure 101 Body axes velocities lateral failure at hover

A similar failure is analyzed next, for the 20 ft/sec flight condition. The results for that simulation are shown next, in Figure 102 to Figure 104.

In a similar way as for the hover case, the failure has a prime impact on the lateral states of the helicopter, although in this case, the instability takes a longer period of time to manifest. Thus, showing the inability of the helicopter architecture and control scheme to cope with the failure under such circumstances.

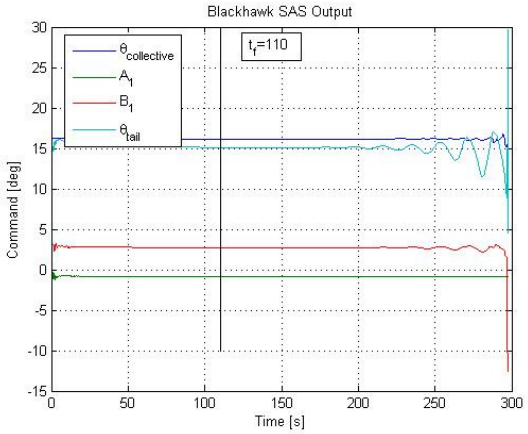

Figure 102 Actual main rotor command with failure at hover

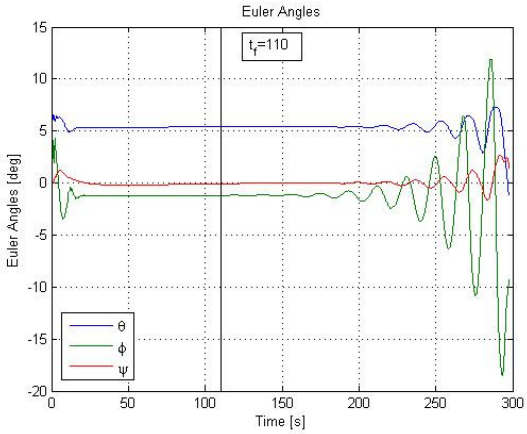

Figure 103 Euler angles lateral failure at hover

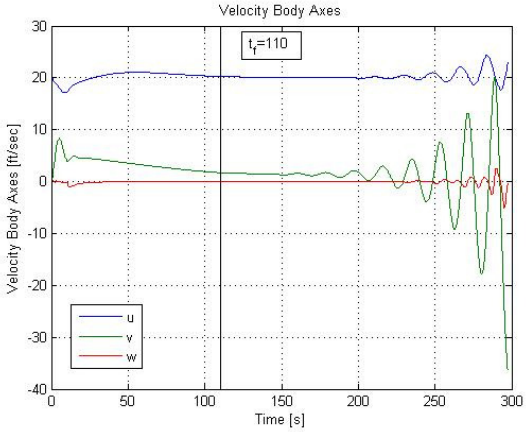

Figure 104 Body axes velocities lateral failure at hover

For the next scenario, the longitudinal actuator is subjected to a failure. For the hover case, the simulation results are shown in Figure 105 to Figure 107. As for the longitudinal failure, the helicopter shows an unstable behavior when the failure is applied, however in this case the instability takes a longer period of time to have a significant impact on the performance of the helicopter, than for the lateral case. This can be reasonably explained by the fact that the helicopter has less inertia in the lateral direction than in the longitudinal one.

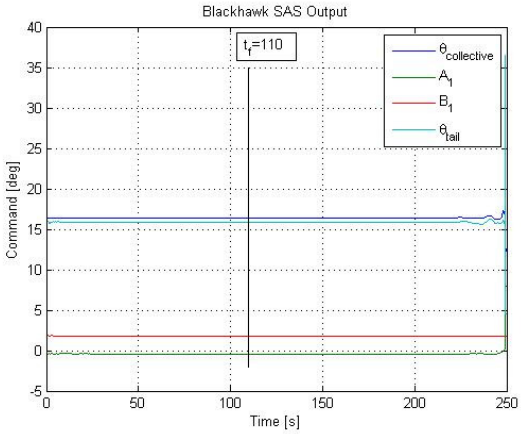

Figure 105 Actual main rotor command with failure in forward flight

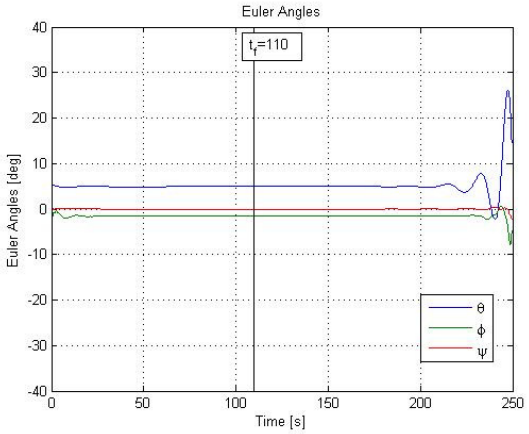

Figure 106 Euler angles longitudinal failure in forward flight

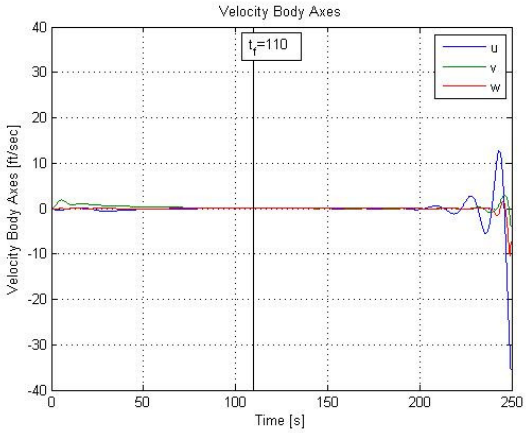

Figure 107 Body axes velocity longitudinal failure in forward flight

The case for the forward flight condition is analyzed next, and the simulation results are shown in Figure 108 to Figure 110. In a similar way as for the hover case, the stuck actuator generates an instability in the helicopter for which the controller architecture can not accommodate, even with the inclusion of the nonlinear dynamic inversion augmented with neural networks. However, in this case, the failure has a more immediate effect than in the hover case, leaving less time for any pilot reaction.

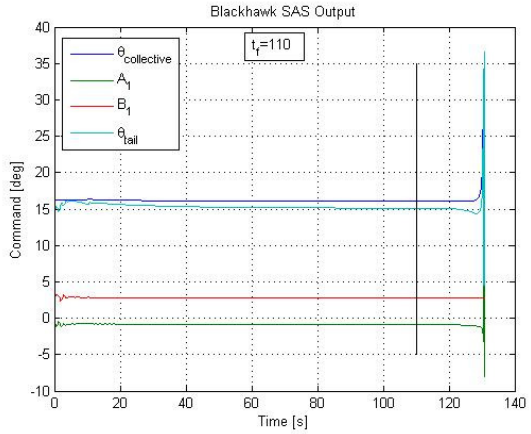

Figure 108 Actual main rotor command with failure in forward flight

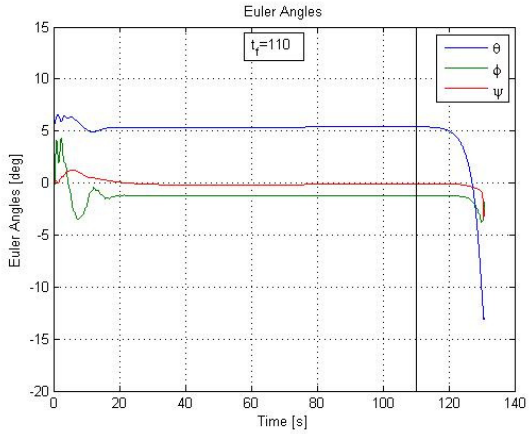

Figure 109 Euler angles longitudinal failure in forward flight

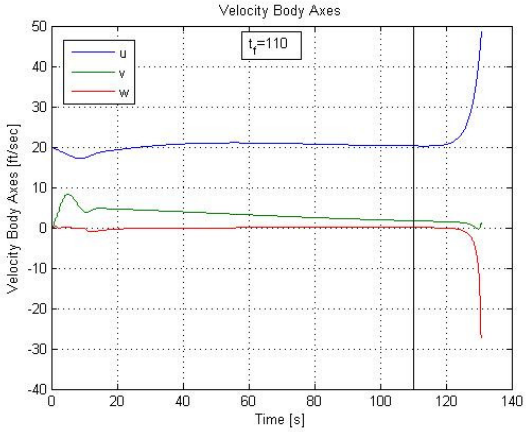

Figure 110 Body axes velocities longitudinal failure in forward flight

A collective actuator failure is simualted in Figure 113 to Figure 115 and is discussed next. The induced failure for the actuator is taken from the hover trim position and fixed at 15.5 degrees, with a time constant of 1 second. In contrast to the previous cases for the lateral and longitudinal failures, the control scheme, even without individual blade control, is able to stabilize the helicopter. However, as can be seen in Figure 115, the new flight condition is far from hover; since the failure has caused the helicopter to descent at a constant rate of 4.2 ft/sec, which depending on the altitude of the helicopter above ground can represent a dangerous flying condition. It is to be noted that the collective has its biggest impact on the heave mode, whichs is in itself a highly decoupled mode, allowing for a quick stabilization of the helicopter and moderate control. Furthermore, the adaptation to accommodate for the collective can be clearly seen in Figure 113, where the neural network cancels the inversion error for the new flight condition. The adaptation vector along with the nonlinear dynamic inversion values are added to

the SAS and classic control input and are shown in Figure 111. Calculation for the error metrics are shown in Table 21 and Table 22.

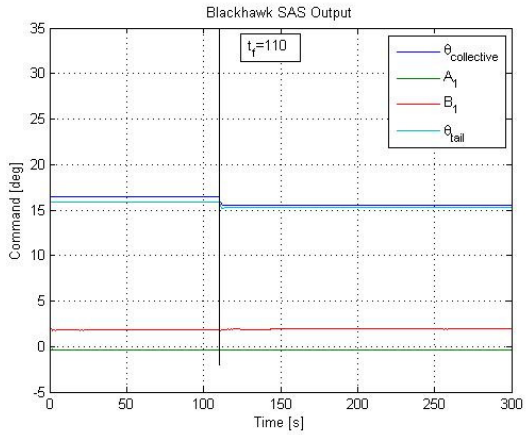

Figure 111 Actual main rotor command with failure at hover

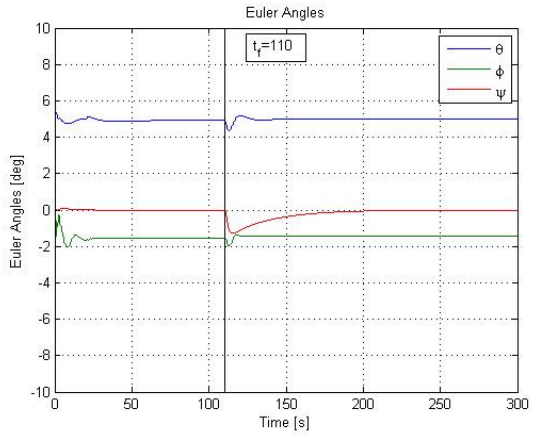

Figure 112 Euler angles collective failure at hover

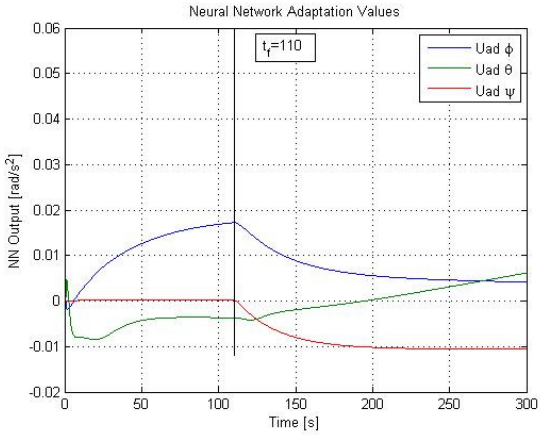

Figure 113 Adaptive output collective failure at hover

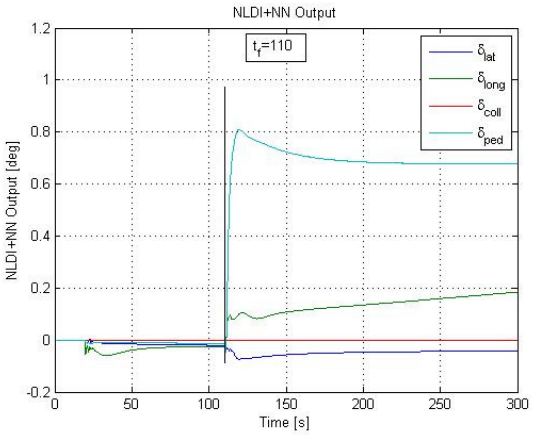

Figure 114 NLDI+NN output collective failure at hover

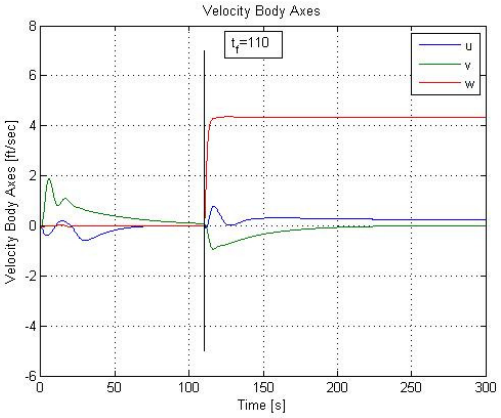

Figure 115 Body axes velocity collective failure at hover

The collective failure is now evaluated for the forward flight condition. In this case the actuator is taken from the trim condition value and taken to the 15 deg value. The transitioning is governed by a first order transfer function with a time constant of 1 sec. Simulation results are presented in Figure 116 through Figure 121.

In a similar way as for the hover case, the control scheme manages to stabilize the helicopter, as can be seen in Figure 118, where after the failure and a transitory period, the Euler angles stabilize to a new trim condition and stay there. In the case of the velocity, it can be seen that the forward flight speed comes back to the established set parameter, however the helicopter falls at a constant rate of approximately 4.5 ft/sec. The reduction in the helicopter given collective angle can be clearly observed in Figure 119, where the mean of blade pitch angle of the helicopter is reduced, hence showing the potential of the individual blade control to compensate for such reduction and obtain the desired trim conditions.

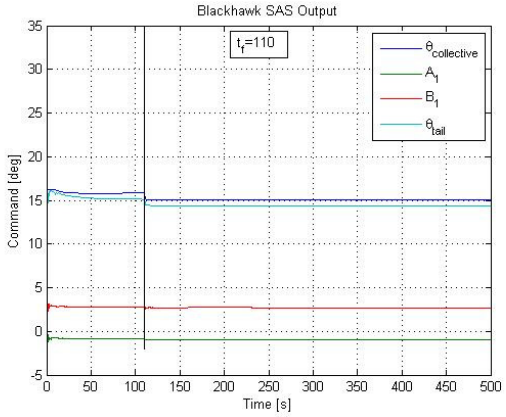

Figure 116 Actual main rotor command with failure in forward flight

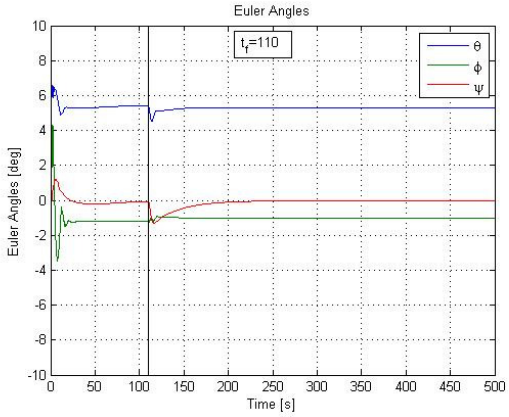

Figure 117 Euler angles collective failure in forward flight

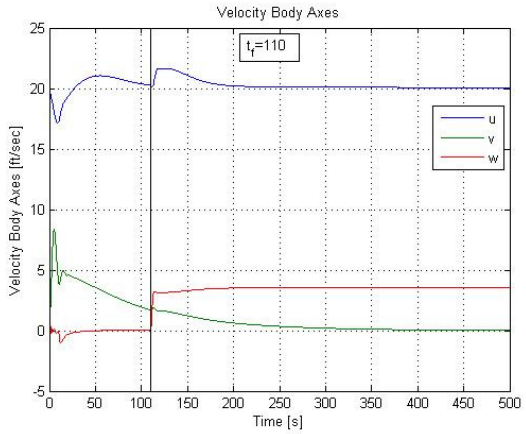

Figure 118 Body axes velocities collective failure in forward flight

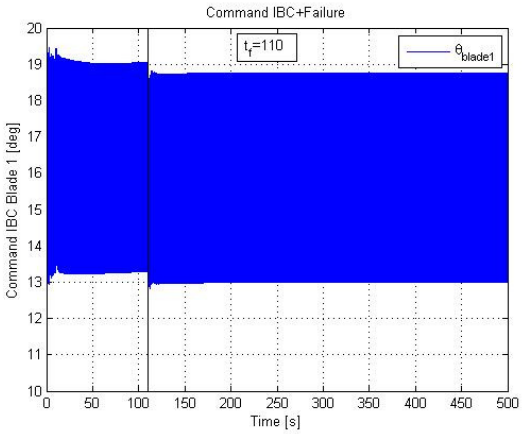

Figure 119 Blade #1 pitch angle in forward flight

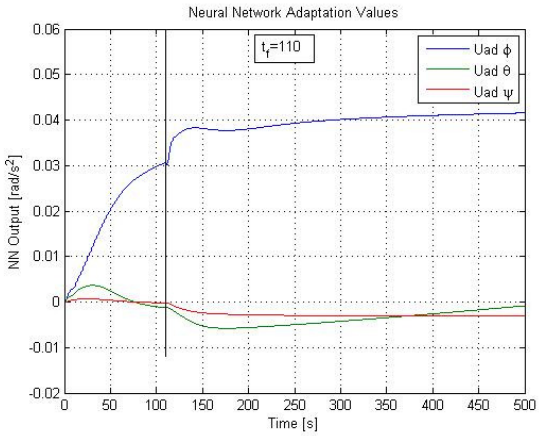

Figure 120 Adaptive output collective failure in forward flight

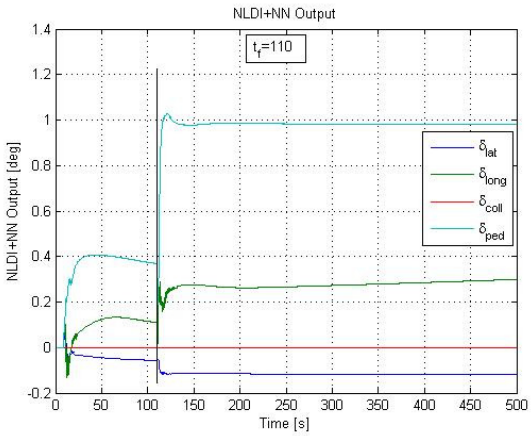

Figure 121 NLDI+NN output collective failure in forward flight

Having tested the failures for lateral and longitudinal swashplate actuator, for hover and forward flight conditions, it becomes clear that not even the effort made by the control scheme is capable of overcoming the failure for said channels. Also it is to be noted that the action of the controller to overcome the failure with the help of the natural coupling of the lateral and longitudinal dynamics had no impact on the stabilization of the helicopter itself.

In the case of the collective, the natural decoupling of the heave mode with respect to other modes, allows for easy stabilization of the helicopter under failure. This natural characteristic of the helicopter actually allows for the design of the two-scale controller for the NLDI. However, the helicopter still lacks enough lift to be able to match nominal conditions. Furthermore, the helicopter falls at a constant rate that in some cases can cause an impact with the ground if the pilot is not fast enough at recognizing the failure and enter in immediate autorotation.

6.1.3 Classic with Individual Blade Control Architecture

The case where the classic swashplate architecture is fitted with the individual blade actuators is discussed next.

Following the same testing pattern as for the classic architecture, lateral, longitudinal, and collective actuator failures are simulated next.

Lateral failure is discussed first for the hover condition, and the simulation results are shown in Figure 122 to Figure 127. The lateral failure is fixed at a value of -0.5 deg, a first order transfer function with a time constant of 1 second is used to smooth the signal between the trim and final fixed value.

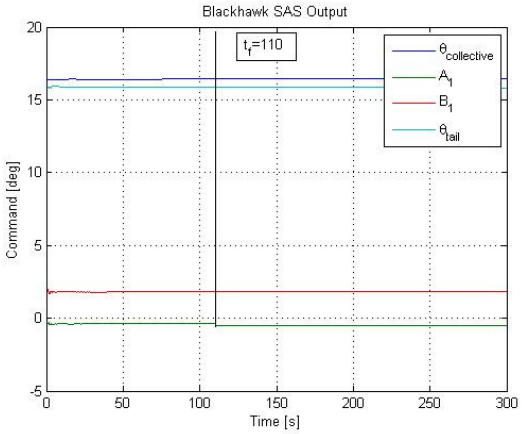

Figure 122 Actual main rotor command with failure at hover

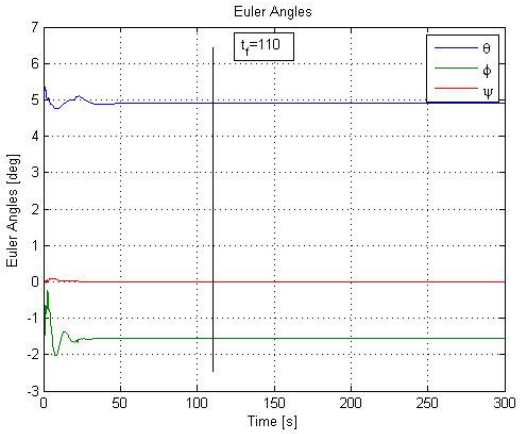

Figure 123 Euler angles lateral failure at hover

As can be seen in Figure 122, the failure is injected after a 110 second period, but there is no effect in the performance of the helicopter, as can be seen in the Euler angles and body axes velocity. This performance of the helicopter is attributed to the effective action of the individual blade controller, shown in Figure 126, which accommodates the fault by generating the compensation in each of the blades. This compensation is enough for the helicopter to perform under nominal conditions. Since there are not variations in the behavior of the helicopter itself, the nominal controller and the NLDI fitted with neural networks do not need to accommodate for the failure itself.

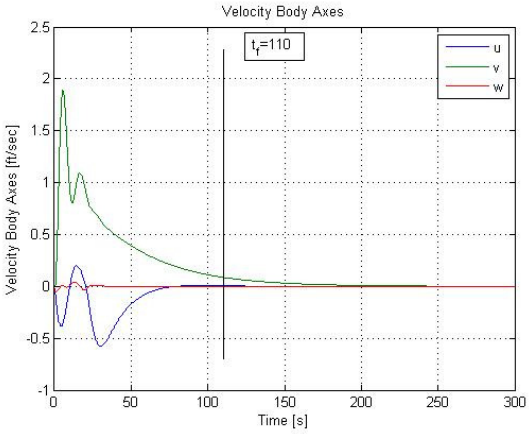

Figure 124 Body axes velocities lateral failure at hover

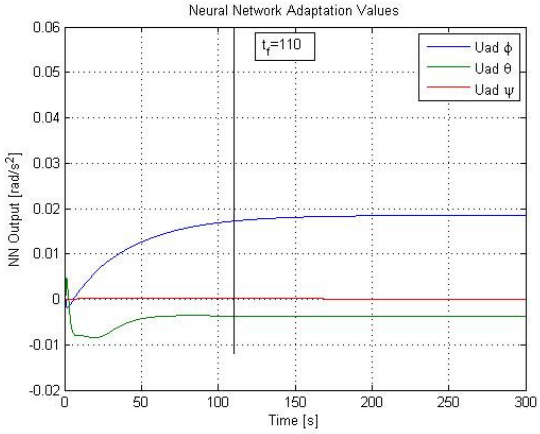

Figure 125 Adaptive output lateral failure at hover

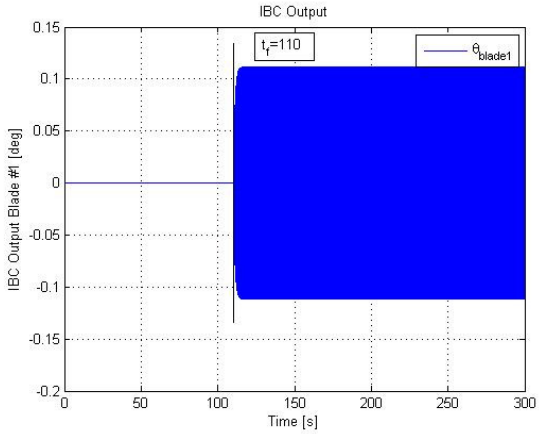

Figure 126 IBC controller output at hover

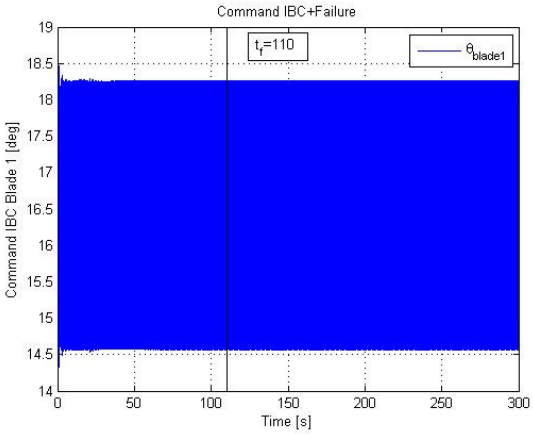

Figure 127 Blade #1 pitch angle at hover

Similarly the lateral failure is now tested for the forward flight condition. Simulation results are shown in Figure 128 through Figure 133. As can be clearly observed in Figure 129, the controller scheme not only stabilizes the helicopter but also allows for the helicopter itself to obtain the same flight characteristics as with the nominal condition. This behavior can be easily attributed, as with the hover case, to the compensation provided by the individual blade controller, whose action can be observed in Figure 132, compensating for the failure. Again, it is imperative for the controller scheme to have a fast response of the failure identification scheme in order to obtain a stable performance of the helicopter.

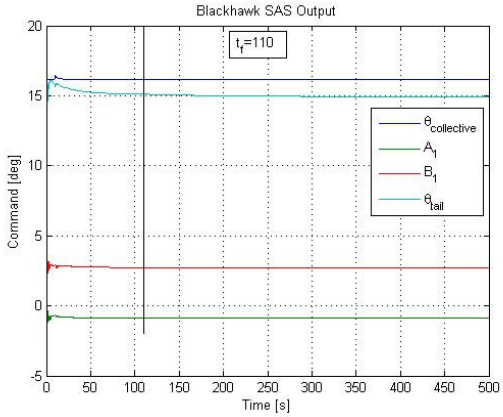

Figure 128 Actual main rotor command with failure in forward flight

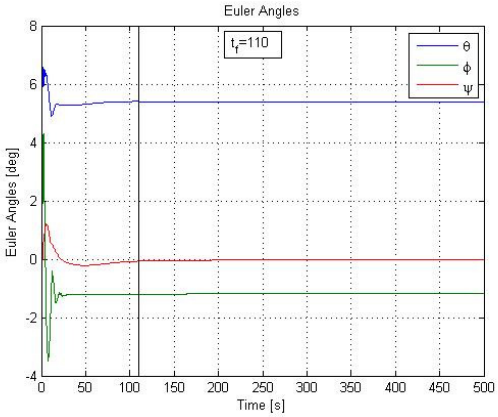

Figure 129 Euler angles lateral failure in forward flight

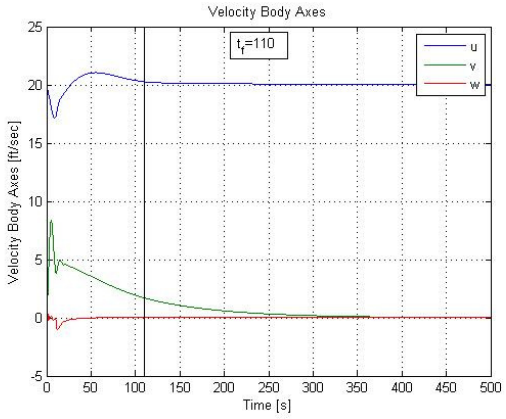

Figure 130 Body axes velocities lateral failure in forward flight

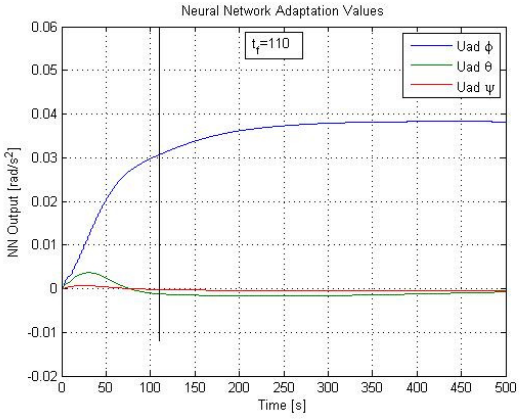

Figure 131 Adaptive output lateral failure in forward flight

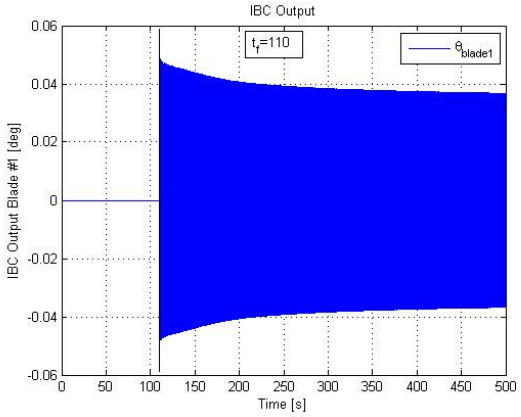

Figure 132 IBC controller output in forward flight

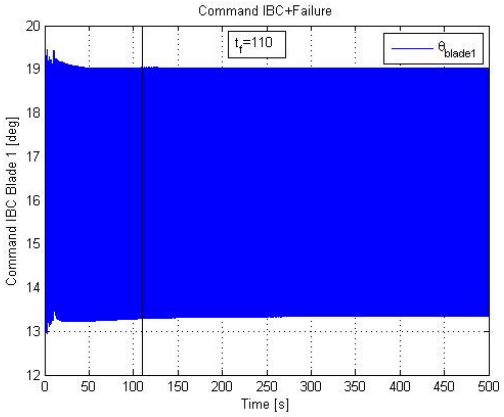

Figure 133 Blade #1 pitch angle in forward flight

Actuator failure for the longitudinal actuator is discussed next. First, the hover condition will be evaluated, and the simulation results can be observed in Figure 134 through Figure 139. In this case, the failure of the actuator occurs by fixing the actuator at the trim condition, and as for the other failures, the failure is injected after a 110 second period. As with the lateral case, the helicopter is not only stabilized but the flight conditions are maintained, as can be seen in the Euler angles and the body axes velocity in Figure 135 and Figure 136 respectively. In a similar way, the adaptation rates are not dissimilar, since there is no change in the flying characteristics of the helicopter itself, as shown in Figure 137. Hence the stabilization process as with the previous cases is performed thanks to the action of the individual blade controller, which compensates for the longitudinal failure.

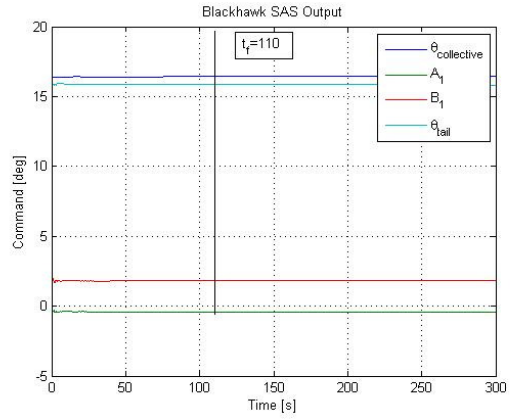

Figure 134 Actual main rotor command with failure at hover

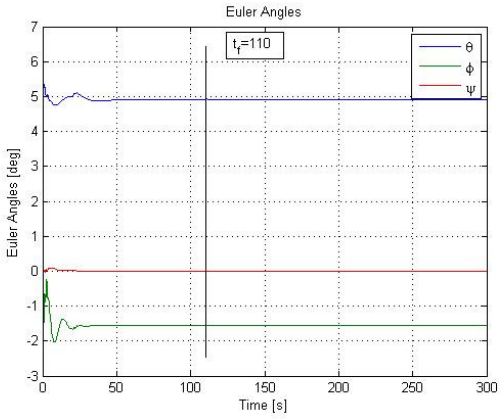

Figure 135 Euler angles longitudinal failure at hover

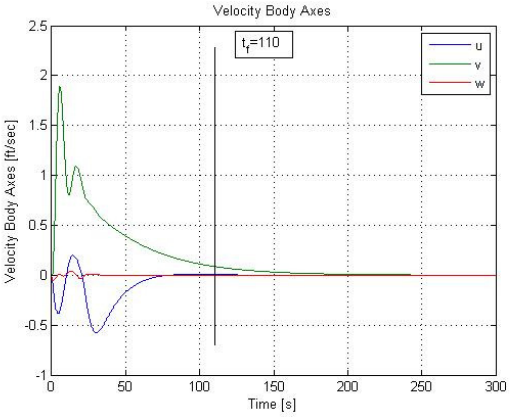

Figure 136 Body axes velocities longitudinal failure at hover

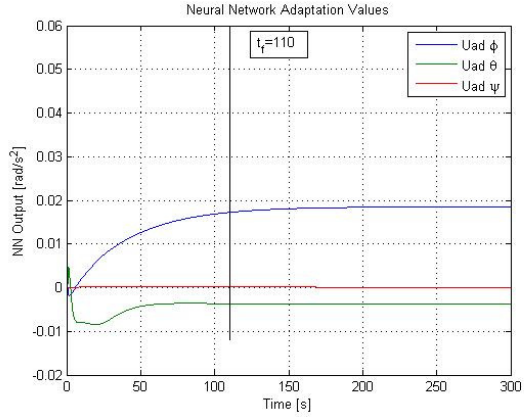

Figure 137 Adaptive output longitudinal failure at hover

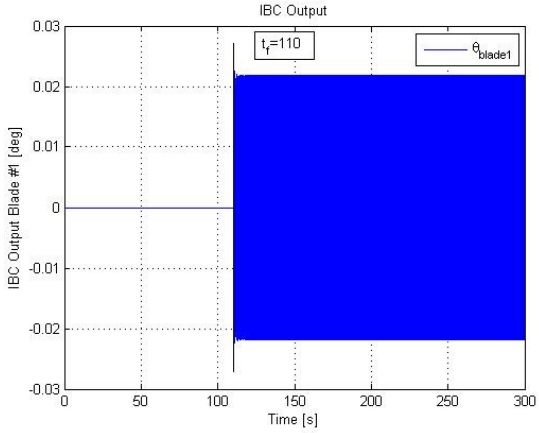

Figure 138 IBC controller output at hover

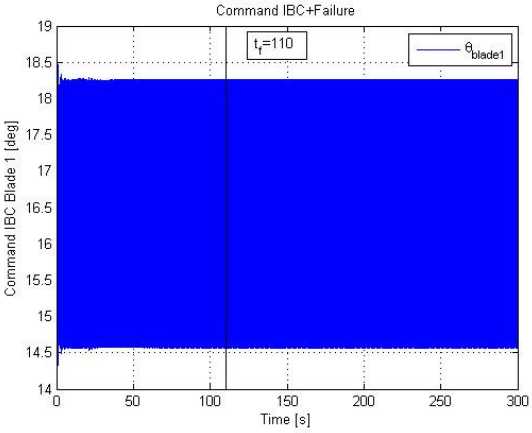

Figure 139 Blade #1 pitch angle at hover

The case for the forward flight condition under longitudinal failure is discussed next. Simulation results for this particular case are shown in Figure 140 through Figure 145. In this case, the failure of the actuator has been placed at the trim position, as can be seen in Figure 140.

As in previous cases, the individual blade controller scheme is not affected by the nature of the different forward speed, as with the hover case. This behavior can be clearly observed in Figure 142 where the forward speed is kept constant after the failure and no transitory effect is shown. The failure is compensated again by the individual blade controller, whose signal is shown in Figure 144 for the first blade. The input for the other three blades is shifted by an angle of 90 deg with respect to the first blade.

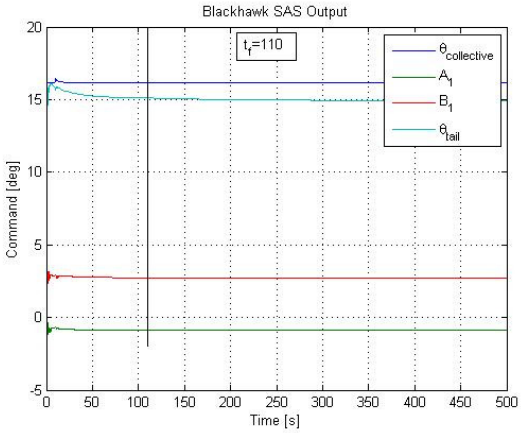

Figure 140 Actual main rotor command with failure in forward flight

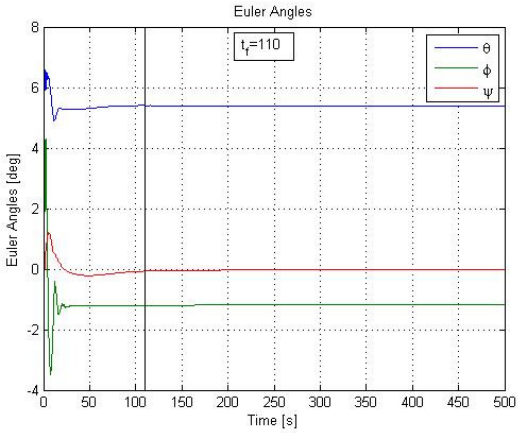

Figure 141 Euler angles longitudinal failure in forward flight

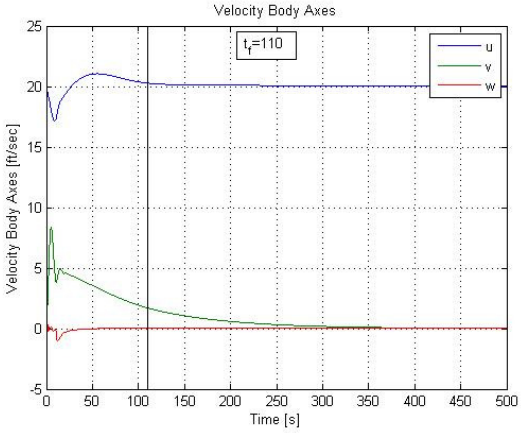

Figure 142 Body axes velocities longitudinal failure in forward flight

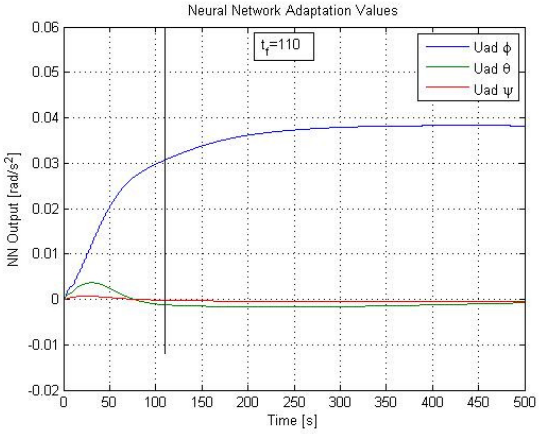

Figure 143 Adaptive output longitudinal failure in forward flight

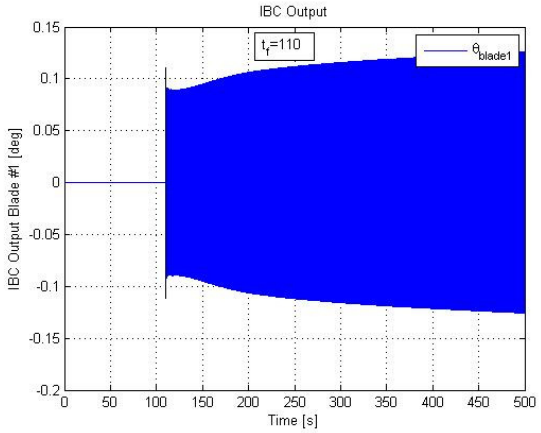

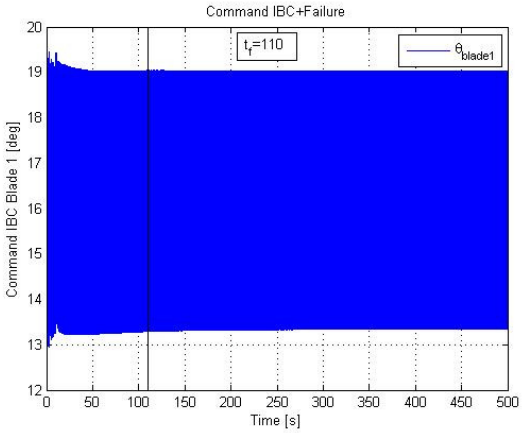

Figure 144 IBC controller output in forward flight **Figure 145 Blade #1 pitch angle in forward flight**

Analysis for the controller scheme for collective failure is discussed next. The case for the hover flight condition will be analysed first and the simulation results are shown in Figure 146 through Figure 151. As for the classic architecture case, the collective failure was set for the actuator to stuck at a value of 15.5 deg, a first order transfer function takes the signal from the trim value to the specified value with a time constant of 1 second. When this case was analyzed for the classic swashplate configuration, the simulation was stable; however there was a constant rate of descent of 4 ft/s, and as can be seen in Figure 148, the controller scheme is capable of accommodate for the failure without suffering from the rate of descent. This accommodation occurs at the individual blade controller, as for the lateral and longitudinal failure cases, as can be seen in Figure 150. In this case the value is a constant since does not vary with the azimuth angle, therefore, the same value is added to all the blades.

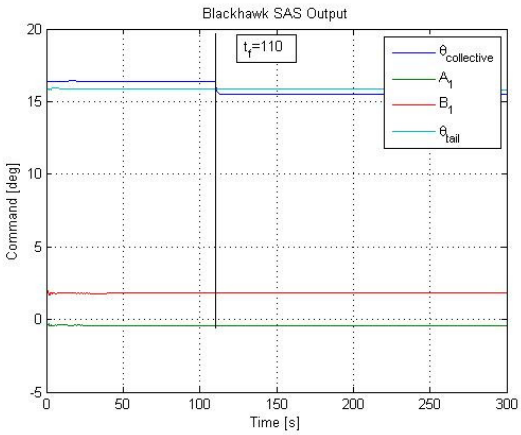

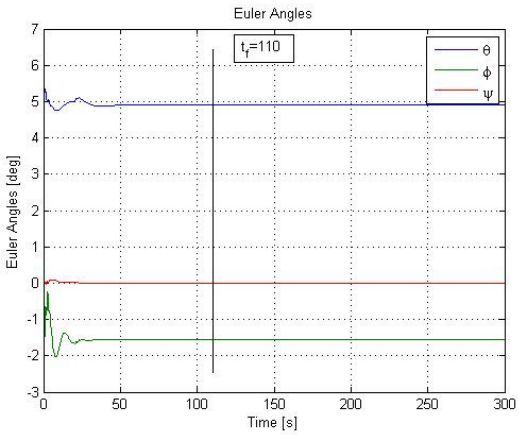

Figure 146 Actual main rotor command with failure at hover **Figure 147 Euler angles collective failure at hover**

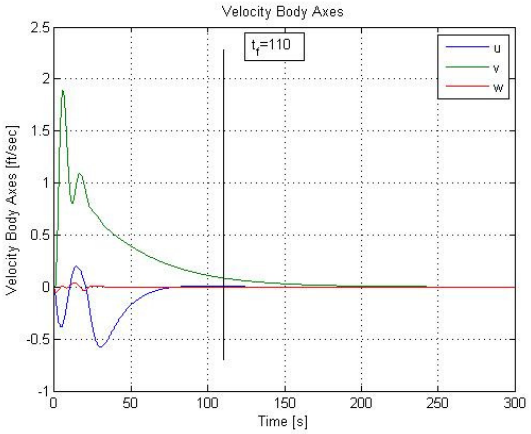

Figure 148 Body axes velocities collective failure at hover

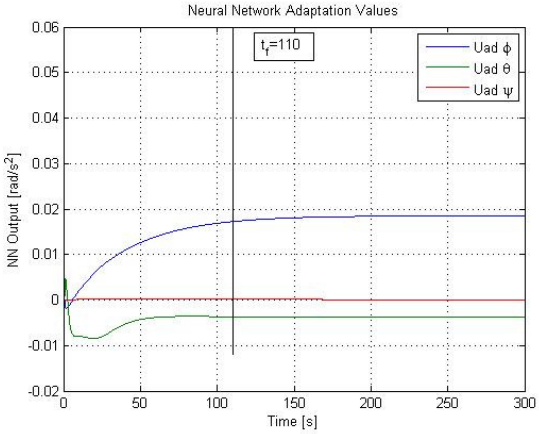

Figure 149 Adaptive output collective failure at hover

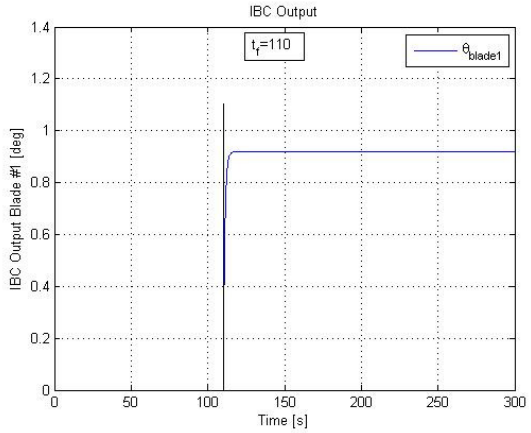

Figure 150 IBC controller output at hover

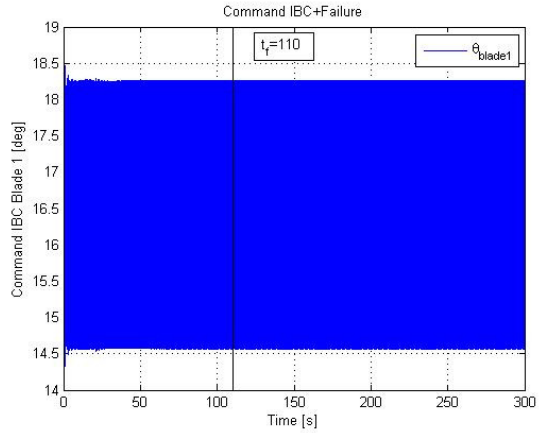

Figure 151 Blade #1 pitch angle at hover

The collective failure for the forward flight condition scenario is shown in Figure 152 to Figure 157. In this case, the helicopter collective actuator was locked at a deflection of 15 deg, with a transition from the trim value to the given value with a first order transfer function with a time constant of 1 second, as shown in Figure 152. In a similar pattern as the hover case, the controller scheme is capable to correct for the rate of descent, as can be seen in Figure 154, where said descent rate is kept at zero. Furthermore, since there is no change in the behavior of the helicopter due to the action of the individual blade controller, the adaptation values for the inversion error do not change from their nominal values. The input from the individual blade controller can be observed in Figure 156, where the constant value is added to blade #1 and the same amount is added to the other available blades.

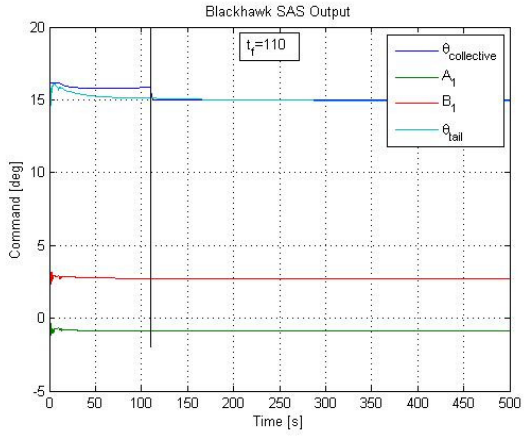

Figure 152 Actual main rotor command with failure in forward flight

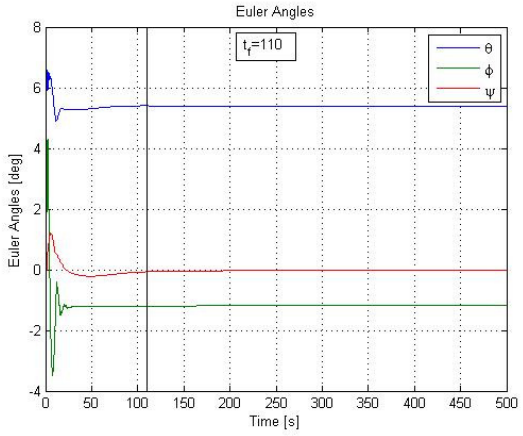

Figure 153 Euler angles collective failure in forward flight

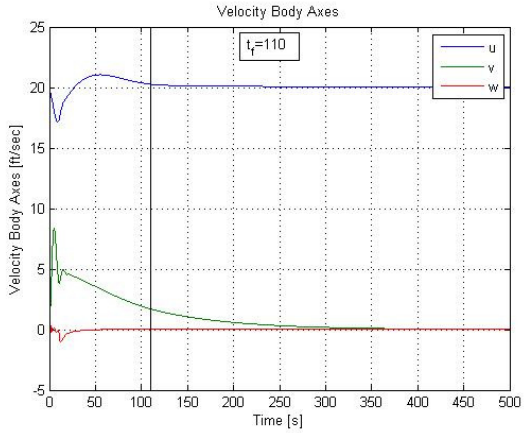

Figure 154 Body axes velocities collective failure in forward flight

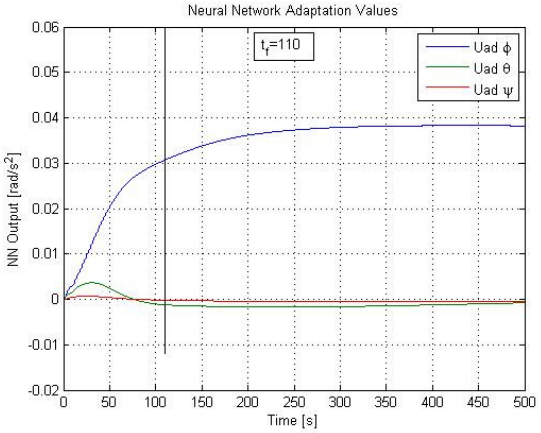

Figure 155 Adaptive output collective failure in forward flight

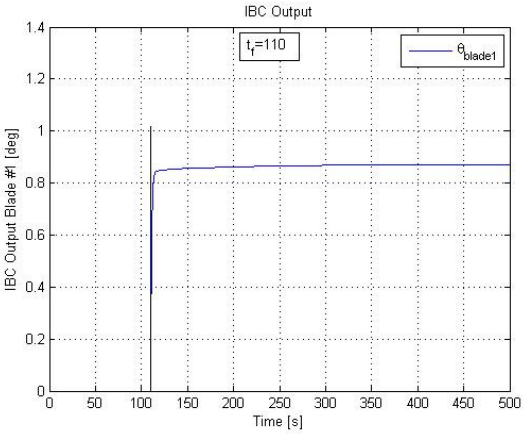

Figure 156 IBC controller output collective failure in forward flight

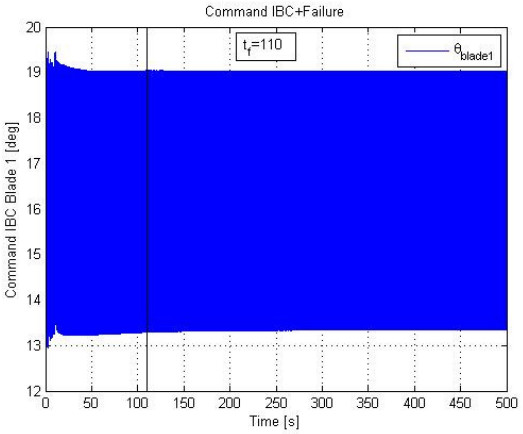

Figure 157 Blade #1 pitch angle collective failure in forward flight

As shown in chapter 5 of this work, the individual blade control scheme, is dependant on the failure identification scheme, to not only identify the failure, the time of the failure and the magnitude of the failure itself. In order to test the robustness of the individual blade control scheme augmented with the NLDI algorithm, a test was conducted for the controller inducing a lateral failure. The failure was induced so the actuator was stuck at the trim value for a forward flight condition of 20 ft/s. A bias of 0.2 deg was induced also in the swashplate failure measurement to establish the robustness of the scheme. Results for this simulation are shown in Figure 158 through Figure 174.

As can be observed in Figure 174, once the failure occurs, the individual blade controller comes into effect, however as can be seen in the same figure, the bias is immediately evident, since the mean of the output value is now 0.2 degrees instead of 0 (which would be the case as shown in the simulation example with the same characteristics without the bias in this chapter). This bias has an immediate effect on the performance of the helicopter, however the NLDI manages to identify the failure and compensate for it, as can be clearly identified by the increment on the adaptive values for the pitching and rolling moments shown in Figure 161. The adaptation has its biggest increase for the roll moment, since this is the specific area where the bias is. This adaptation of the control scheme is not only capable of stabilizing the helicopter for the specified set of speeds and failures, but also to overcome the effect of the bias and maintain nominal flight conditions. These nominal conditions are obtained after a transition of about 80 seconds, as can be clearly seen in the Euler angles and velocity in body axis shown in Figure 159 and Figure 160 respectively.

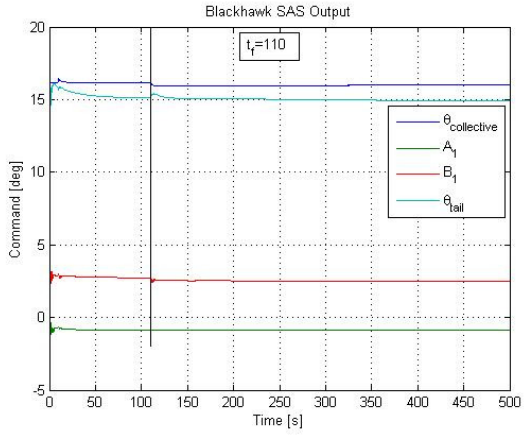

Figure 158 Actual main rotor command with failure in forward flight

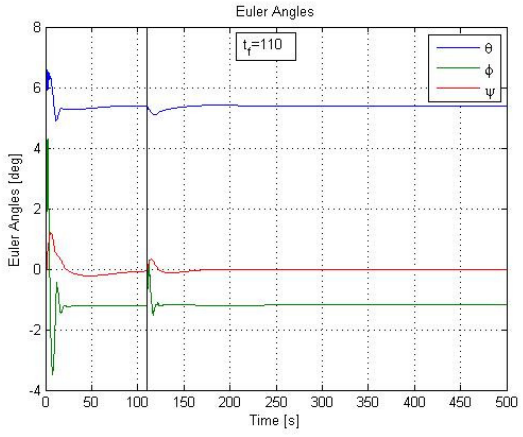

Figure 159 Euler angles lateral failure with bias in forward flight

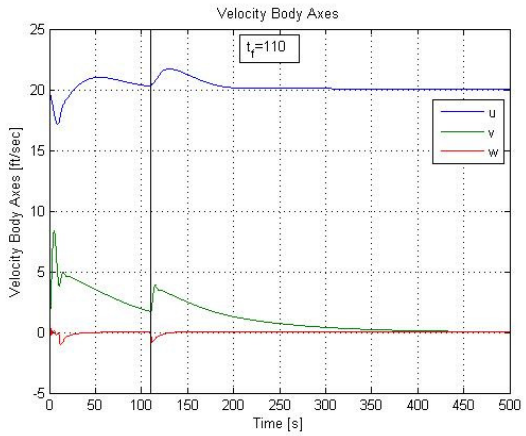

Figure 160 Body axes velocities lateral failure with bias in forward flight

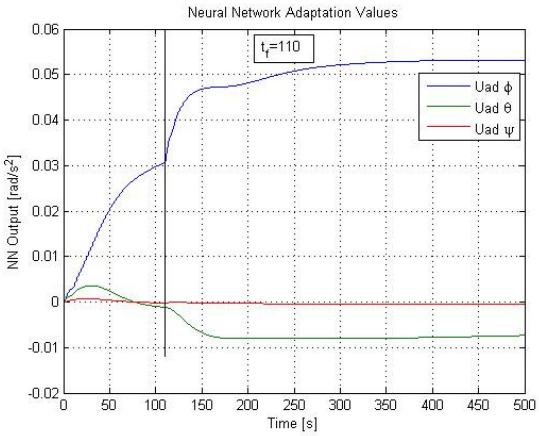

Figure 161 Adaptive output lateral failure with bias in forward flight

To test the habilities of the scheme using the PCH, a test for the 20 ft/s flight condition was simulated using values of 1.8 deg for the swashplate bias and a lateral failure at the trim condition. The results for this simulation set are shown in Figure 162 to Figure 167. As can be seen, the lateral failure and the swashplate bias have an immediate effect on the Euler angles and velocity in body axes of the helicopter. To compensate for the failure, the IBC controller starts to compensate for the failure as seen in Figure 164, however the bias effect causes that the neural networks increase its adaptation values at a high rate as seen in Figure 165, which in turn create very high values for the helicopter inputs, as shown in Figure 166. These high values are measured by the PCH scheme, and corresponding angular accelerations are calculated, as presented in Figure 167 so they are fed back into the commanded accelerations for the NLDI scheme, reducing the magnitude of the helicopter control inputs while a proper adaptation occurs and the helicopter is stabilized. Eventually, the PCH output is decreased when the inputs for the helicopter are within the safety boundaries set earlier on, and the controller scheme is capable of resuming nominal flight conditions.

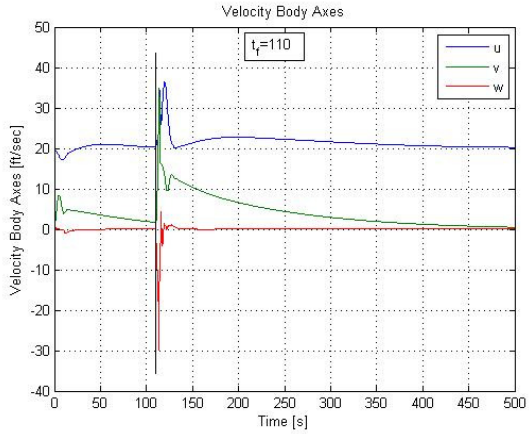

Figure 162 Body axes velocities lateral failure with bias in forward flight with PCH

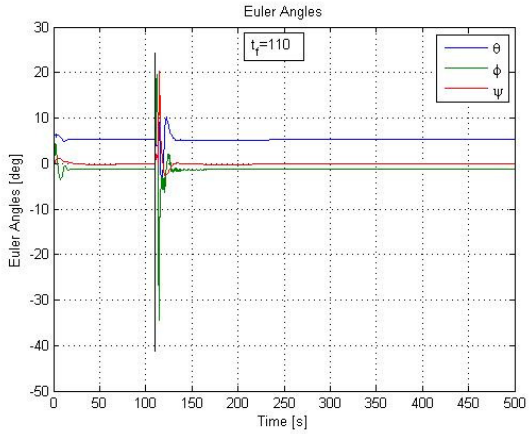

Figure 163 Euler angles lateral failure with bias in forward flight with PCH

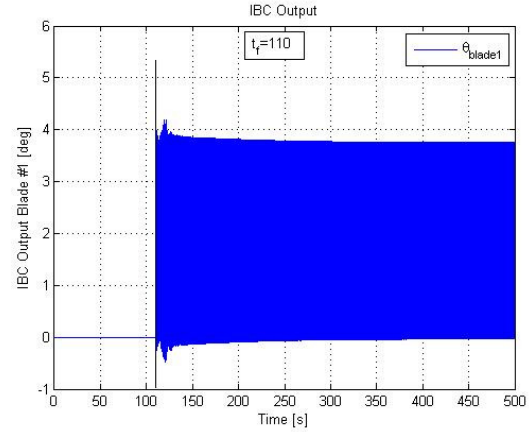

Figure 164 IBC controller output lateral failure with bias in forward flight with PCH

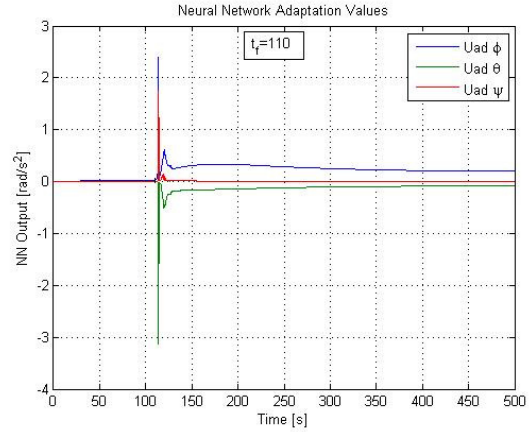

Figure 165 NN adaptation values lateral failure with bias in forward flight with PCH

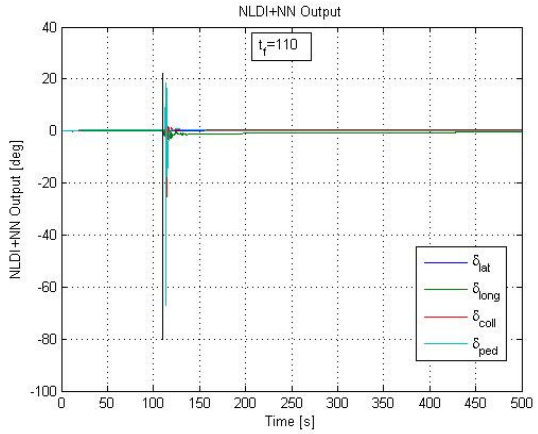

Figure 166 NLDI command lateral failure with bias in forward flight with PCH

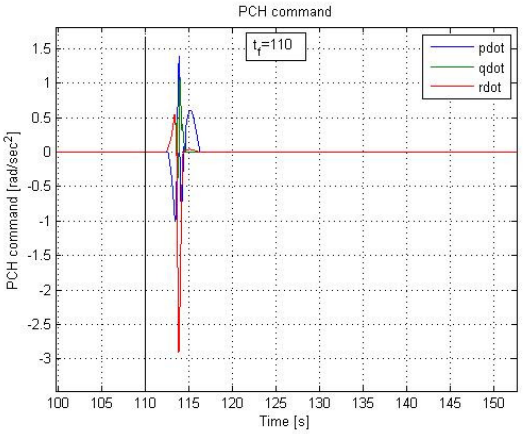

Figure 167 PCH output for lateral failure with bias in forward flight with PCH

A comparison of the previous simulation test can be done with the same failure and scheme without the action of the pseudo control hedging technique, and is shown in Figure 168 to Figure 172. As can be seen, without the action of the PCH scheme, the inputs to the helicopter

are saturated and go beyond the possible values that the actual helicopter can take, as seen in Figure 171, mainly as a consequence of the high adaptation values that the neural network calculates for the inversion error. Eventually these high values take the helicopter out of control.

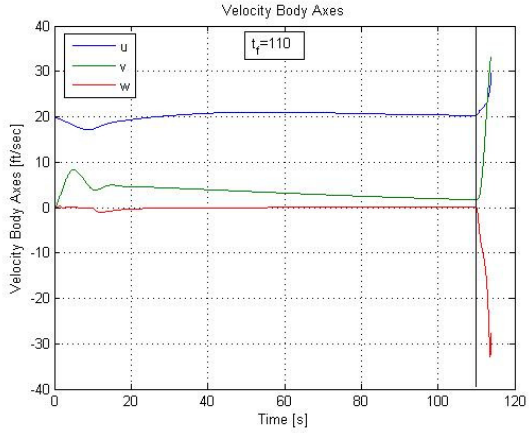

Figure 168 Body axes velocities lateral failure with bias in forward flight without PCH

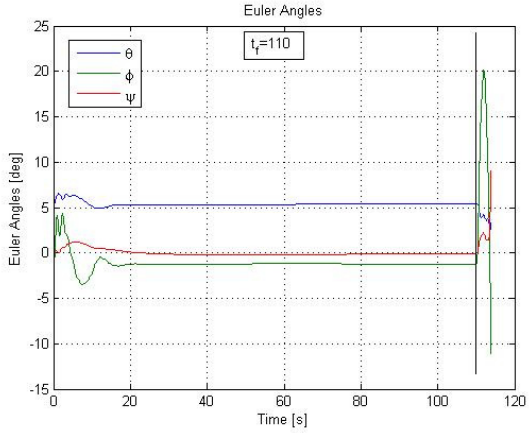

Figure 169 Euler angles lateral failure with bias in forward flight without PCH

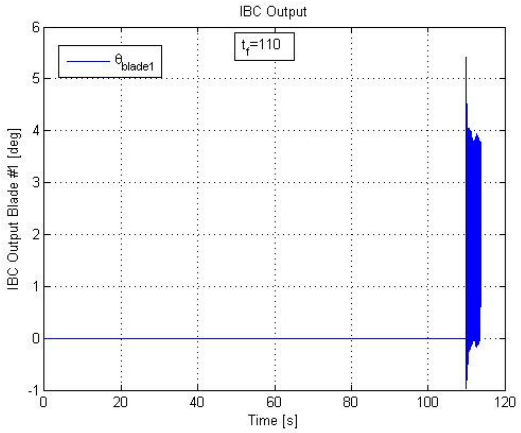

Figure 170 IBC controller output lateral failure with bias in forward flight without PCH

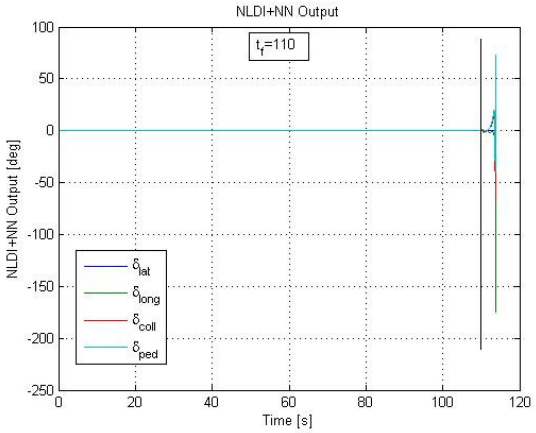

Figure 171 NN adaptation values lateral failure with bias in forward flight without PCH

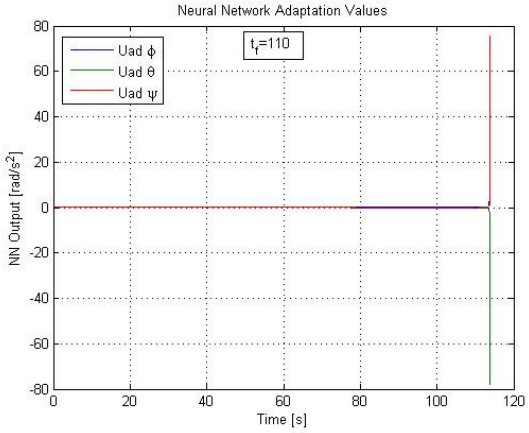

Figure 172 NLDI command lateral failure with bias in forward flight without PCH

Having performed all the tests for this particular configuration, it is pretty clear that the individual blade control presents a great advantage when it comes to the stabilization and performance improvement under failure conditions. Given that in all the failures previously described, the action of the IBC control law allows for failure accommodation and undisturbed trimmed flight conditions. As for the lateral and longitudinal actuator failure, the control scheme, stabilizes and reaches nominal conditions. In the case of the collective, since the helicopter was already stable, it provides the additional redundancy to obtain the same flight condidions as if the failure had not occured. Furthermore, the control laws used for the individual blade controller do not require the action of the classic and NLDI controller to obtain the nominal flight condition. Hence, no adaptation is necessary for either the hover or forward flight.

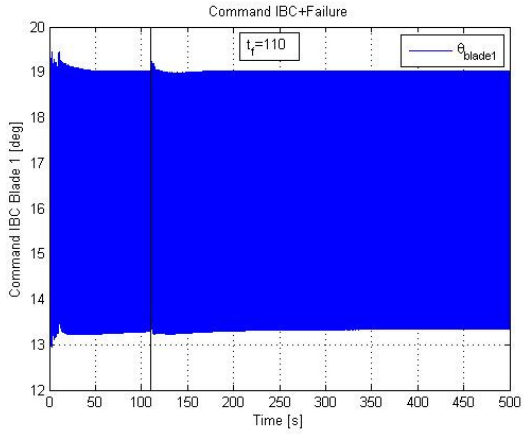

Figure 173 IBC controller output in forward flight

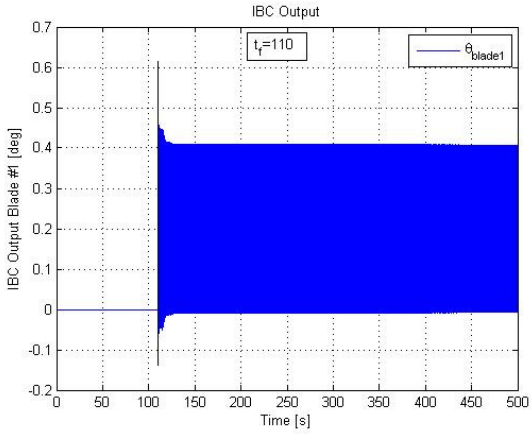

Figure 174 Blade #1 pitch angle in forward flight

As has been previously shown in this dissertation, the conjunction of the classic swashplate fitted with individual blade actuators architecture has some sensitivity issues regarding the timing and identification of the failure. The timing is associated with the period of time between the identification of the failure and the actual occurrence of the failure. The identification of the failure is associated with not only which actuator has failed but the position at which has failed. A bias in this measurement generates an offset in the nominal flight conditions when only the individual blade control law is applied, since the mean of the individual blade control output is offset by this same value. However, with the addition of the NLDI and the classic controller this offset is eradicated, which is mainly due to the action of the adaptation of the controller to the new characteristics of the helicopter. Hence showing that the developed

control architecture not only accounts for failures but also introduces some robustness into the overall scheme, by allowing a "safe zone" for the failure identification method to work, and yet obtain nominal flight conditions

6.1.4 Individual Blade Control Architecture

The individual blade control architecture investigated within this research effort requires the use of a "virtual swashplate" that takes the values for the lateral and longitudinal cyclics and calculates the blade pitch angle for each of the blades; therefore, the failures investigated here will be applied to the actuators of each of the blades for the previously described flight conditions.

The case where one blade actuator is failed in hover is discussed first. For this particular failure the stuck and hold option will be used from the different options for actuator failure. Simulation results are shown in Figure 175 to Figure 180. As can be observed in Figure 176 and Figure 177, the blade actuator failure has an immediate effect on all the attitude and body axes velocities. High frequency motion can be observed in both the velocities and the Euler angles given the fact that the failed blade generates an unbalanced load on the main rotor. Given that the blade is stuck at a value of around 18 degrees, this generates a decrease in the lift of the blade on the retreating side but an increase on the advancing side, thus creating the high frequency motion in the Euler angles and the velocity in body axis. In this case, the nonlinear dynamic inversion augmented with neural networks notices the existence of an error in the outputs, given the nominal inputs, reflected in the difference between the nominal model and the new conditions, and starts to adapt the inputs of the system to obtain nominal conditions under failure. The biggest variation occurs for the pitching moment, as can be observed in Figure 178, since the failure causes the biggest variation in the velocity along the x axis of the body reference frame. Given the coupling that exists for the lateral and longitudinal dynamics in the helicopter, the rolling moment requires to be adjusted also, therefore having the second largest change in the adaptive signal to account for the difference. As said before, the blade pitch angle is larger than in the nominal condition on the advancing side, therefore there is an increase in the main rotor torque, which requires to be adjusted by the tail rotor in order to obtain nominal flight conditions. Hence, the pedal input is increased thanks to the action of the inversion and a small compensation on the inversion error by the neural network.

As can be observed after a transitory period the classic and nonlinear dynamic inversion scheme is capable of not only stabilizing the helicopter, but also to take it to nominal hover conditions. As expected, the attitude of the helicopter has changed slightly to accommodate for the failure, as can be observed in Figure 176. Changes occur mainly in the roll and pitch angle of the helicopter, since the heading angle remains unchanged.

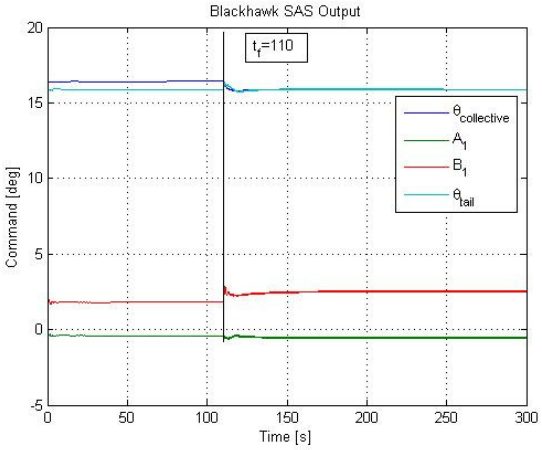

Figure 175 Actual main rotor command with failure at hover

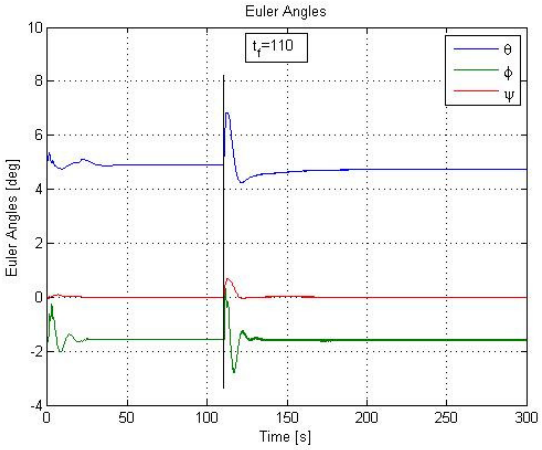

Figure 176 Euler angles IBC actuator failure at hover

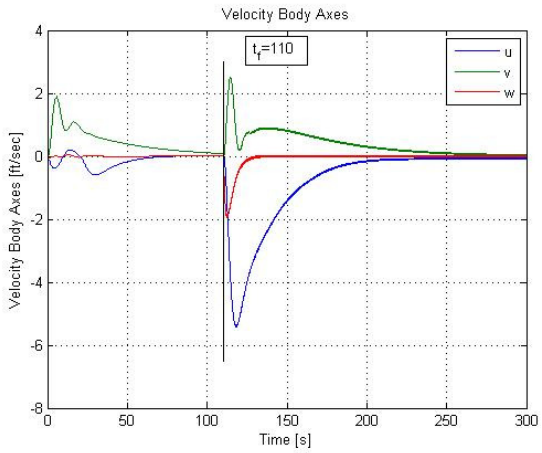

Figure 177 Body axes velocity IBC actuator failure at hover

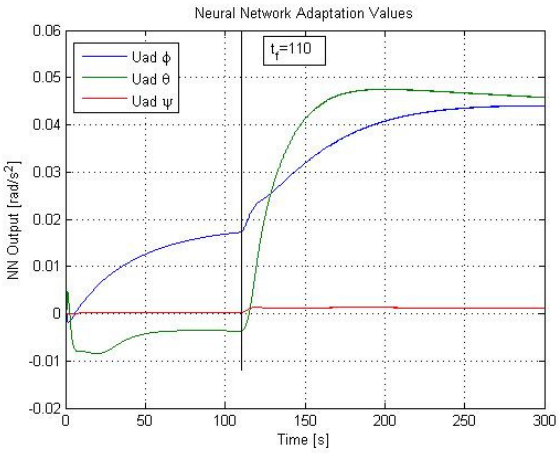

Figure 178 Adaptive output IBC actuator failure at hover

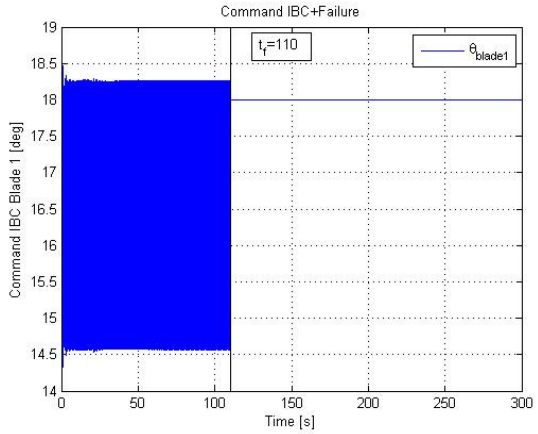

Figure 179 Blade #1 pitch angle at hover

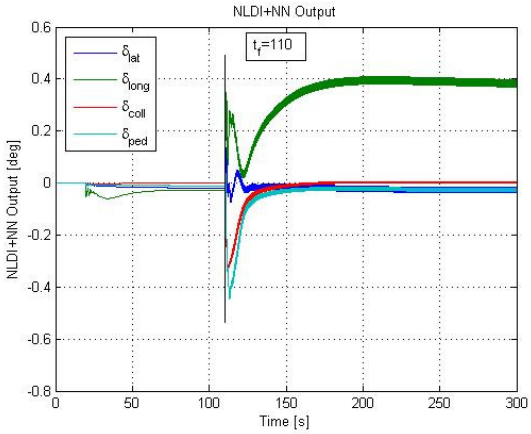

Figure 180 NLDI+NN output at hover

The failure scenario in which a blade fails under forward flight condition is discussed next. Simulation results for this particular failure can be observed in Figure 181 to Figure 186. As for the hover case, the failure induced for the first blade as shown in Figure 185, has an immediate impact on all the rigid body variables of the helicopter, but the classic and NLDI augmented with neural networks scheme provides a stabilization of the helicopter, even resuming the nominal conditions albeit of the associated main rotor vibration. Following the same trend as when the blade actuator fails in hover, most of the stabilization process occurs by adjusting the pitching and rolling moment, as can be seen in Figure 184. However for the forward flight condition the amount of adaptation for the inversion error in the rolling and pitch moment is very similar, which can be attributed to the fact that in forward flight, the motion of the helicopter is more affected by aerodynamic forces on the fuselage, which act as a damper to the fuselage of the aircraft.

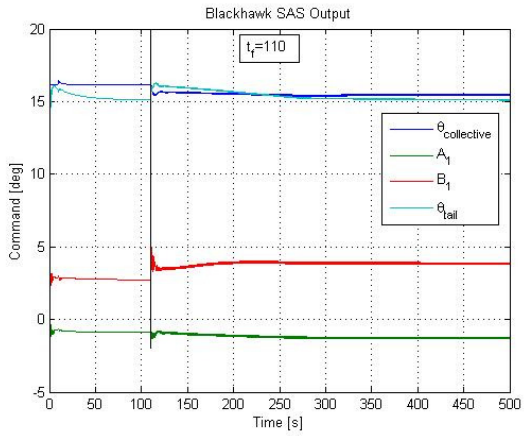

Figure 181 Actual main rotor command with failure in forward flight

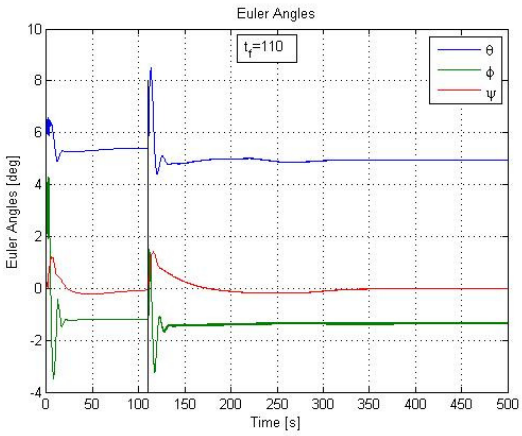

Figure 182 Euler angles IBC actuator failure in forward flight

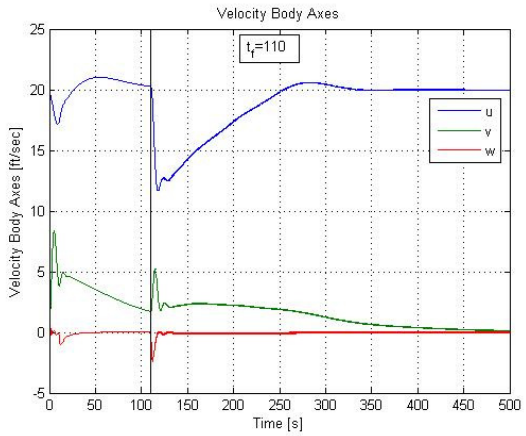

Figure 183 Body axes velocities IBC actuator failure in forward flight

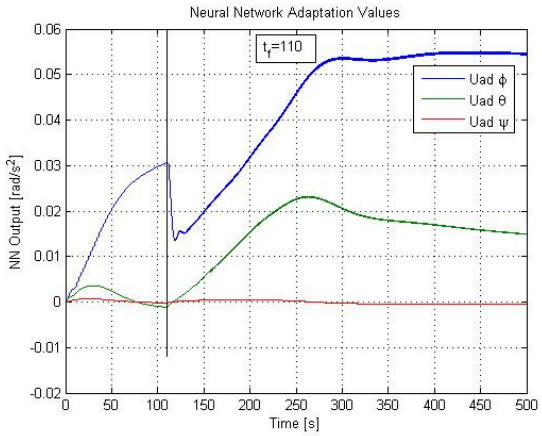

Figure 184 Adaptive output IBC actuator failure in forward flight

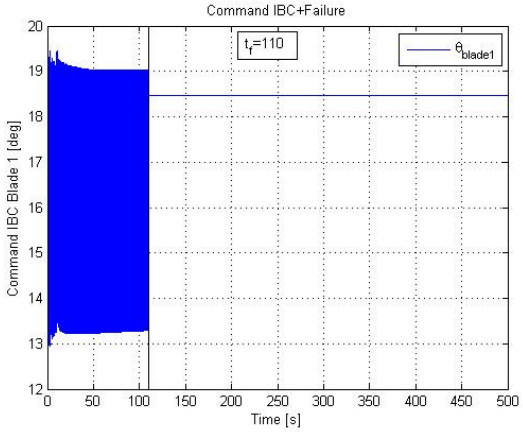

Figure 185 Blade #1 pitch angle in forward flight

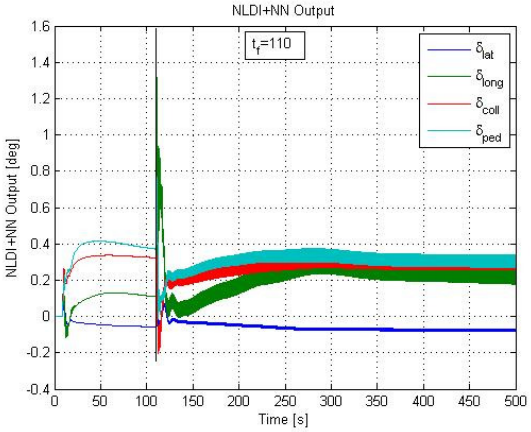

Figure 186 NLDI+NN output in forward flight

The scenario in which two blades fail at the same time is discussed next. Hover results for the failure of blade #1 and blade #2 are shown in Figure 187 to Figure 192. In this case the failure of both blades has a sliaghtly larger impact on the behavior of the helicopter when compared to the one blade failure case. However, the controller scheme is capable of stabilizing the helicopter and resume nominal hover conditions after a transitory period. As is to be expected larger values for the adapatation occur in this case since it's a more degraded state than for the one blade failure.

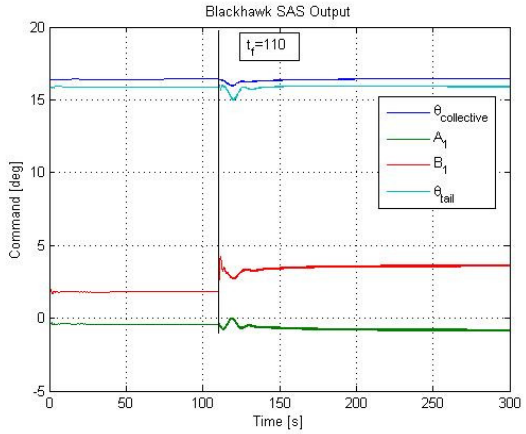

Figure 187 Actual main rotor command with failure at hover

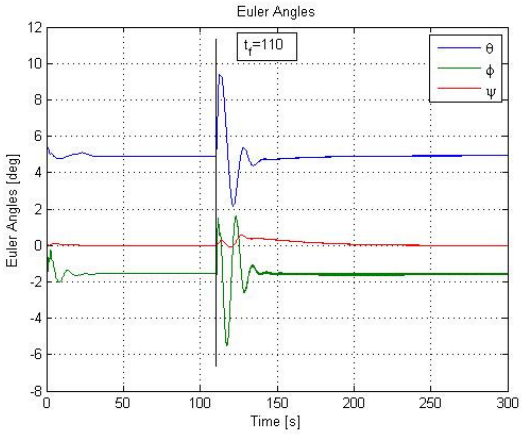

Figure 188 Euler angles IBC actuator failure at hover

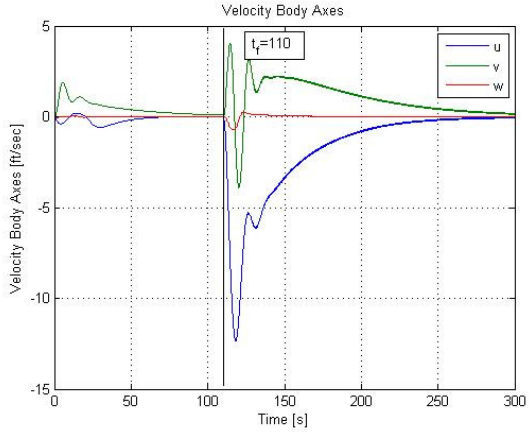

Figure 189 Body axes velocities IBC actuator failure in hover

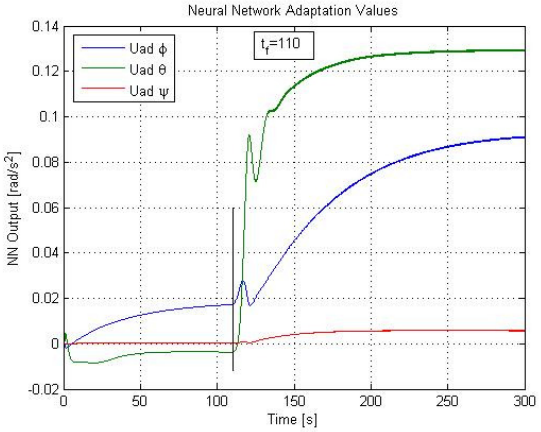

Figure 190 Adaptive output IBC actuator failure in hover

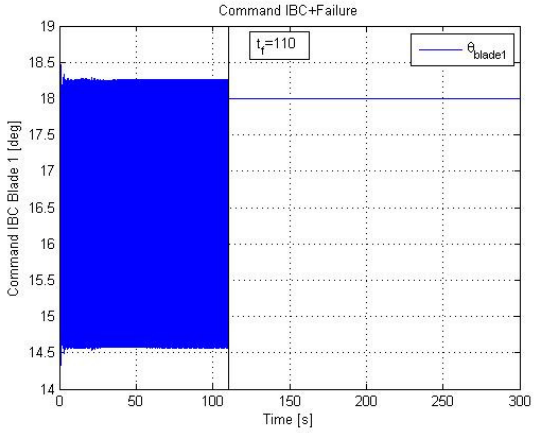

Figure 191 Blade #1 pitch angle in hover

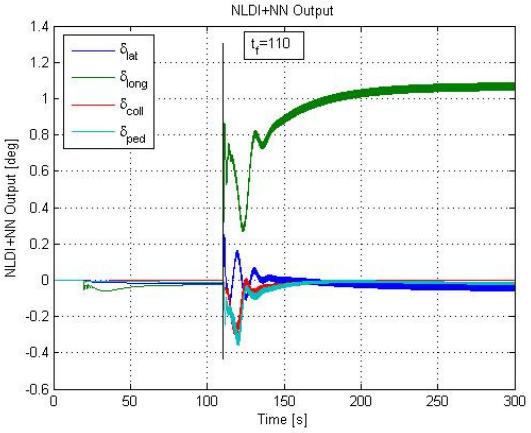

Figure 192 NLDI+NN output in hover

The case for which the helicopter is in forward flight condition is presented next. Simulation results are shown in Figure 193 to Figure 198. In similar case as for the one blade failure in forward flight condition, there is an immediate effect of the failure in the Euler angles

and body axes velocities but with increased amplitude. Hence, adaptation values for the roll and pitch moments are also higher in comparison with the one blade failure.

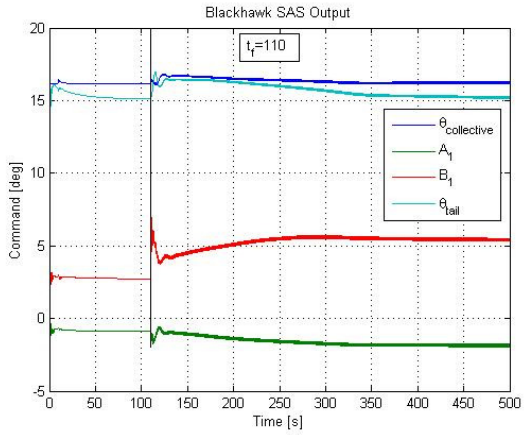

Figure 193 Actual main rotor command with failure in forward flight

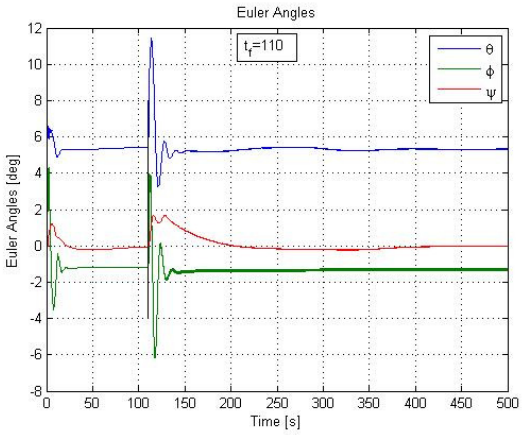

Figure 194 Euler angles IBC actuator failure in forward flight

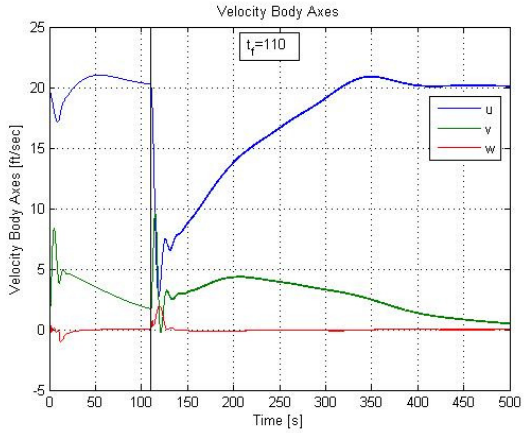

Figure 195 Body axes velocities IBC actuator failure in forward flight

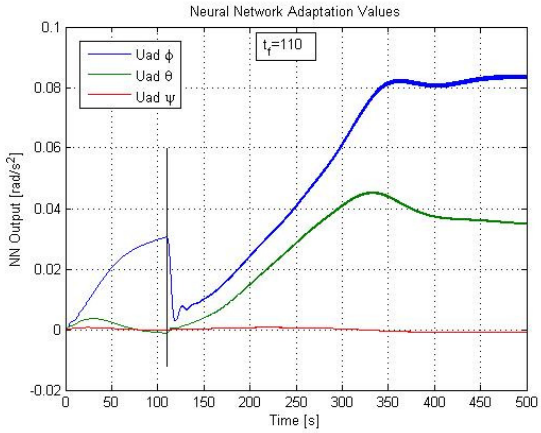

Figure 196 Adaptive output IBC actuator failure in forward flight

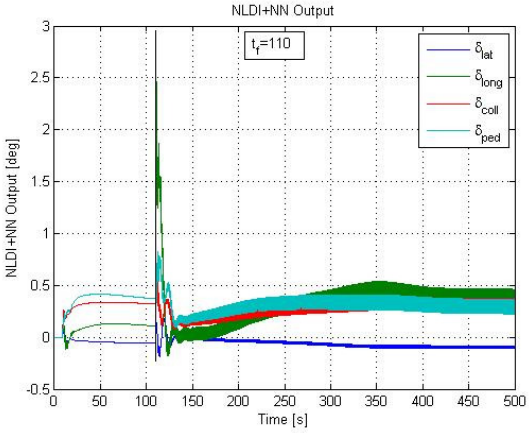

Figure 197 Blade #1 pitch angle in forward flight

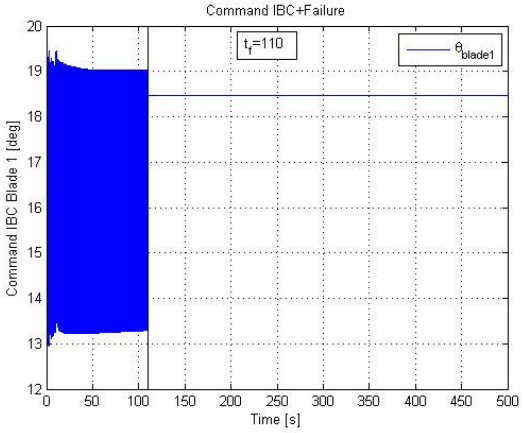

Figure 198 NLDI+NN output in forward flight

As a test of the effectiveness of the NLDI approach as a stabilizing technique for an individually controlled helicopter, it was decided to make a test with a failure in one of the actuators for one of the blades with only the classic control loop, and then compare it with the classic control with the NLDI augmentation. Results are shown in Figure 199 to Figure 203. As can be observed in Figure 202 the induced failure to blade #1 is the same as the one discussed previously for the hover flight condition. In the same way as the classic controller augmented with the NLDI technique, the classic control alone is capable of not only stabilize the helicopter, but also resume nominal flight condition, as can be seen in the Euler angles and velocity in body axes shown in Figure 200 and Figure 201 respectively. However, the addition of the NLDI improves the overall performance of the controller by reducing not only the overshoot but also by increasing the damping of the response of the helicopter to the failure, as can be clearly observed in Figure 203. There it can be seen that the NLDI reduces the overshoot by 2.8 ft/s and increases the damping by reducing oscillations in the response.

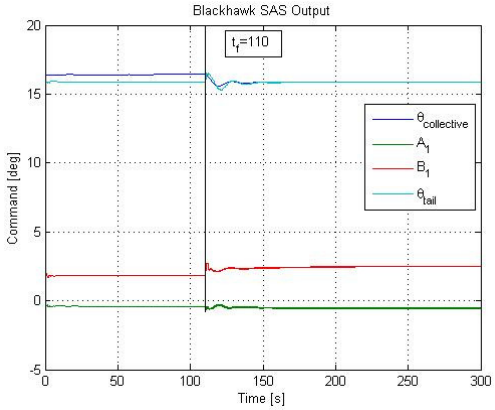

Figure 199 Actual main rotor command with failure at hover

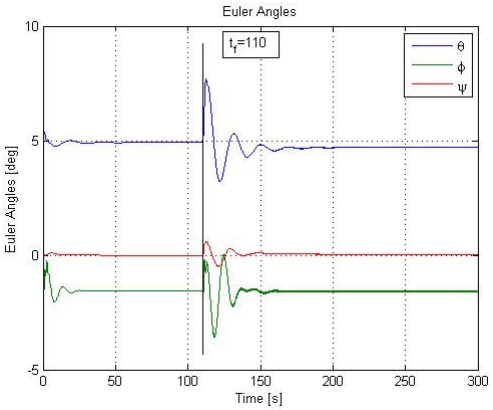

Figure 200 Euler angles IBC actuator failure at hover

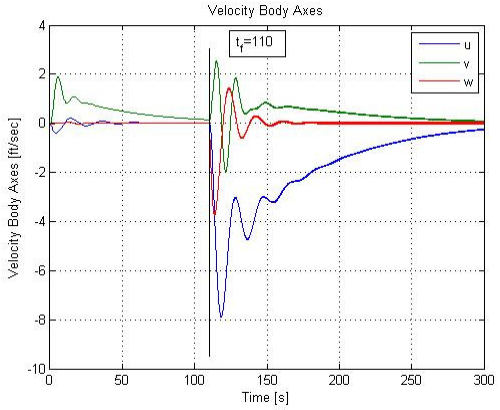

Figure 201 Body axes velocities IBC actuator failure at hover

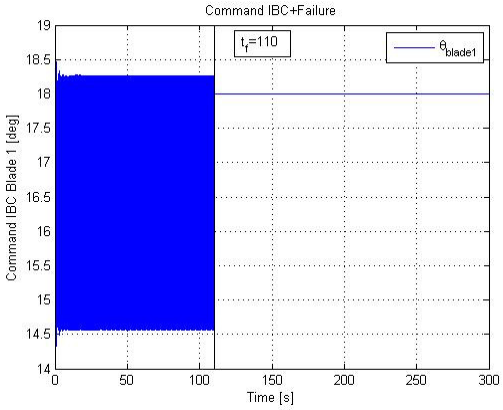

Figure 202 Blade #1 pitch angle at hover

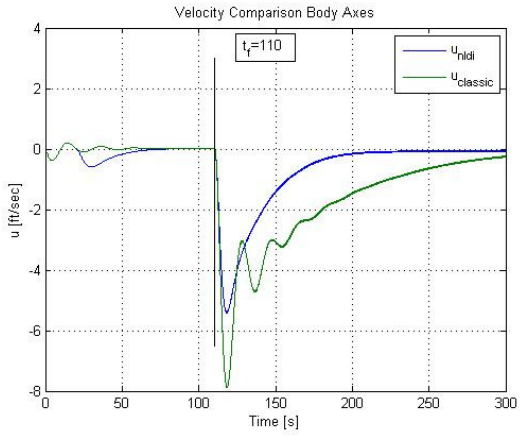

Figure 203 Adaptive output IBC actuator failure at hover

Error metrics according to equation (212) were calculated for both hover and forward flight condition tests. The results of these tests are shown in Table 21 and Table 22 respectively. Values for unstable simulations could not be calculated; hence their values were represented by "N/A".

Table 21 Error metrics for hover flight condition under failure

Test/Failure	E						
	u	v	w	Θ	Φ	Ψ	ΣE
Classic/Lat	N/A	N/A	N/A	N/A	N/A	N/A	N/A
Classic/Long	N/A	N/A	N/A	N/A	N/A	N/A	N/A
Classic/Coll	0.068	0.055	0.784	0.232	0.294	0.304	1.739
IBC/Lat	1.37e-4	0.0024	1.11e-5	1.31e-5	1.91e-4	1.81e-4	0.0029
IBC/Long	1.43e-4	0.0023	1.19e-5	9.25e-5	1.81e-4	1.78e-4	0.0030
IBC/Coll	1.37e-4	0.0023	1.15e-5	8.74e-6	1.19e-4	1.78e-4	0.0028
IBC/B1	0.25	0.12	0.06	0.68	0.28	0.06	1.47
IBC/B1(no NLDI)	0.46	0.18	0.16	0.87	0.38	0.12	2.21
IBC/B1 & B2	0.57	0.37	0.03	0.65	0.61	0.16	2.39

As can be observed in both tables, the lower values of the error metrics are consigned for the classic swashplate fitted with additional individual blade control actuators, for which flight conditions are very close to nominal conditions.

In the case of hover, the highest value for the error metrics is assigned to the double individual blade control actuator failure with NLDI compensation, which had the most degraded state in all tests, considering that two actuator blades failed. The second highest value is is for the single individual blade actuator failure without NLDI compensation; this value is then compared against the same failure with the NLDI, for which the case where the system has NLDI compensation is lower than the one that does not. Hence, this fact reassures the previous

assessment on the stabilizing and performance improvement nature of the NLDI control architecture, especially when a failure for an individual blade control actuator occurs.

The third highest value comes from the collective failure for the classic swashplate architecture. In this case, values should be compared against the same failure for the IBC architecture, in which case it can be clearly observed that the IBC architecture with NLDI surpasses the performance of the classic architecture, since the first one has lower values of error metrics than the second one. The biggest difference of the classic architecture in the error metrics lies in the value assigned for the speed in the z direction, which is logical, considering that the collective failure induces a steady state error for this particular variable.

Table 22 Error metrics for forward flight condition under failure

Test/Failure	E						
	u	v	w	Θ	Φ	Ψ	ΣE
Classic/Lat	N/A	N/A	N/A	N/A	N/A	N/A	N/A
Classic/Long	N/A	N/A	N/A	N/A	N/A	N/A	N/A
Classic/Coll	0.0514	0.0381	0.503	0.1442	0.203	0.1625	1.1022
IBC/Lat	0.0047	0.0311	3.16e-4	2.69e-4	0.0011	0.0022	0.0397
IBC/Long	0.0047	0.0311	3.17e-4	2.91e-4	8.31e-4	0.0022	0.0395
IBC/Coll	0.0047	0.0311	4.33e-4	5.17e-4	0.0011	0.0023	0.0401
IBC/B1	0.3166	0.1836	0.0551	0.6853	0.4201	0.2031	1.8637
IBC/B1 & B2	0.6722	0.4189	0.0492	0.5253	0.6596	0.3703	2.6955

The error metrics for the forward flight condition will be discussed next. In a similar way as the hover case, the lowest values are assigned to the individual blade control architecture with classic swashplate approach. This assessment is solidly backed by the fact that when a lateral, collective or longitudinal actuator failure occurs, the performance of the helicopter is very close to nominal conditions. These values should be compared against the classic architecture for the same actuator failure, however, since the helicopter is unstable for this flying condition even fitted with an NLDI scheme, numerical comparisons can not be made. The highest values for the error metrics are shown for the individual blade control actuator failure, for the case in which one and two blades fail. These values are relatively high, especially when compared against the IBC collective failure, however the in the latter case a steady steate error prevails, which is not the case for the blade actuator failures.

The previous chapter shows how the individual blade control laws augmented with classic control and the nonlinear dynamic inversion is a comprehensive alternative to obtain not only redundancy for helicopters under failure, but also to stabilize them in the event that one of the blade actuators fails.

This scheme, however, does have some drawbacks. These drawbacks can be asserted as the requirement of a fault detection, identification and estimation scheme -for the classic swashplate with individual blade actuators- and the lack of stabilization capacity for a two blade actuator failure in hover conditions. For the first case, a technique was provided in this work to assess the impact of the delay in the helicopter performance, even though it was not fully covered for the full IBC+NLDI scheme, it is proposed as a future work in the same area.

7 Conclusions

- A comprehensive and integrated simulation environment for an individual blade control system for helicopters has been successfully implemented and has been demonstrated to provide a powerful tool for the development of fault tolerant techniques for helicopters fitted with this novel technology. This simulation environment includes not only actuator but also sensor and surface delamination failure and includes additional reality enhancing modules such as virtual reality and turbulence models.
- The development of this work has shown a new reconfiguration architecture for which the redundancy of the helicopter, defined as the capability of the helicopter to be qualified to resume nominal or close to nominal conditions after failure, is not only increased but also its actuator disposition allows for better fault tolerance capability. A mathematical analysis for the classic swashplate configuration fitted with individual blade pitch actuators has been developed that proves this assumption.
- A comparison under failure conditions between three different architectures, classic swashplate, classic swashplate fitted with individual blade pitch actuators, and a full authority individually controlled blade system proved the capability of the proposed IBC configuration for improvement of survivability of the helicopter under failure conditions.
- Individual blade control proves to be a technology that is not only valuable for passenger comfort improvement, but also to increase the fault tolerant capabilities of the helicopter; provided that an appropriate control scheme, such as the nonlinear dynamic inversion augmented with neural networks, is implemented.
- This work initiates the analysis of individual blade control as an alternative technique to improve fault tolerant capabilities using blade pitch actuators, with the use of computational tools. Furthermore, this novel approach has allowed for the development of specific adaptive control techniques such as reconfiguration and nonlinear dynamic inversion augmented with neural networks.
- The set of performance metrics proposed in this work, can potentially represent a powerful design tool and evaluation criteria for failure detection and evaluation schemes.

8 Future work

- Given the sensitivity of the classic swashplate fitted with IBC actuators to failure identification and estimation, a fault detection scheme is necessary for the controller to perform properly. Hence, the development of a fault detection and estimation scheme would complete the fault tolerant package necessary for an adequate implementation in full scale applications. Error metrics and the technique to determine appropriate time delays and swashplate biases have been defined in this work for this purpose.
- Even though this work covers the implementation of the individual blade control by means of the blade pitch technology, other technologies such as blade circulation method have been developed at West Virginia University with some satisfactory results. Thus, the following natural step would be to include that technology for research in the feasibility for fault accommodation techniques.
- Given that this work was intended only to test the feasibility of individual blade control and the nonlinear dynamic inversion as a fault tolerant control scheme, and since it was successfully implemented, it is the belief of the author that in order to exploit the full potential of the individual blade control, a frequency domain modeling, instead of a time domain one would increase the performance of both NLDI and IBC techniques
- The research presented in this text has evolved around the virtual swashplate concept. After the evaluation of this concept, it has been concluded that within individual blade control exists more potential to exploit referring to fault tolerance capabilities. Thus, more research in this area without the virtual swashplate concept is suggested, given the infinite possibilities that this technology carries within helicopter stability and control.

9 Bibliography

1. http://www.ntsb.gov/Recs/letters/2009/A09_87_96.pdf

2. Perhinschi, M.G., Campa, G., Fravolini, M.L., Lando, M., Massotti, L., "Performance Comparison of Fault Tolerant Control Laws Within the NASA IFCS F-15 WVU Simulator", Proceedings of the American Control Conference, Denver , CO. 2003

3. Perhinschi, M.G., Burken, J. Campa, G. "Comparison of Different Neural Augmentations for the Fault Tolerant Control Laws of the WVU YF-22 Model Aircraft. Mediterranean Conference on Control and Automation, 2006.

4. Heiges, Michael W. "Reconfigurable Controls for Rotorcraft-A Feasibility Study". Aeromechanics Technology and Product Design for the 21st Century Conference. Bridgeport, CT. 1995.

5. Drozeski, G.R., Saha, B., Vachtsevanos, G.J., "A Fault Detenction and Reconfigurable Control Architecture for Unmanned Aerial Vehicles",IEEE Aerospace Conference, March, 2005.

6. Enns, R. et al. "Helicopter Flight Control Reconfiguration for Main Rotor Actuator Failures". Journal of Guidance, Control and Dynamics. Vol. 26 No. 4, July-August. 2003.

7. Leitner, J. "Analysis of Adaptive Neural Networks for Helicopter Flight Control" AIAA Guidande, Navigation and Control Conference. Baltimore, MD., 1995.

8. Kumar, M. V. "Reconfigurable Neural Controller for Helicopter" 32nd European Rotorcraft Forum. Maastricht, The Netherlands. 2006.

9. http://www.navysbir.com/05_2/124.htm

10. Qi, J et al. "An adaptive Threshold Neural-Network Scheme for Rotorcraft UAV Sensor Failure Diagnosis". Advances in Neural Networks. Vol 4493. 2007.

11. Cork, Lennon and Walker, Rodney. "Sensor Fault Detection for UAVs using a Nonlinear Dynamic Model and the IMM-UKF Algorithm". IEEE Information Decision and Control Conference.2007.

12. Qi, Juntong and Wu, Zhenwei. "Rotorcraft UAV Actuator Failure Estimation with KF-based Adaptive UKF Algorithm". American Control Conference . Seattle, WA. 2008.

13. Garcia, R.D., Valavanis, K. P. and Kandel, A. "Autonomous Helicopter Navigation Turing a Tail Rotor failure Utilizing Fuzzy Logic". 2007 Meditearranean Conference on Control and Automation. July, 2007. Athens, Greece.

14. Ham, N. “Helicopter Individual Blade Control and its Applications”. 39th Annual Forum of the American Helicopter Society. St Louis, MO. 1983.

15. McKillip, Robert. “Periodic Control of the Individual Blade Helicopter Rotor”. Vertica. Vol #9, No 2. pp 199-225. 1985.

16. Shen, J. and Chopra, I. “Swashplateless Helicopter with Triling Edge Flaps”. Journal of Aircraft. Vol 1, No 2. 2004.

17.Shen, J., Yang, M., Chopra, I. “Swashplateless Helicopter Rotor with Trailing-Edge Flaps for Flight and Vibration Control”. Journal of Aircraft. Vol 43, No 2. 2006.

18. Arnold, U.T. P., Furst, D. “Closed loop IBC results from CH-53G flight tests”. Aerospace Science and Technology. Vol 9. 2005.

19. Millot, T., Welsh, W. “Helicopter active noise and vibration reduction”. 25th European Rotorcraft Forum. Rome. 1999.

20. Haber, Axel., Jacklin, Stephen A., DeSimone, Gary. “ Development, Manufacturing, and Component Testing of an Individual Control System for a UH-60 Helicopter Rotor”. American Helicopter Society Aerodynamics, Acoustics, and Test and Evaluation Technical Specialists Meeting. San Francisco, CA. January, 2002.

21. Jacklin, Stephen., Haber, Axel., DeSimone, Gary., Norman, Thomas., Kitaplioglu, Cahit., Shinoda, Patrick. “Full Scale Wind Tunnel Test of an Individual Blade Control System for a UH-60 Helicopter”. 58th Annual Forum of the American Helicopter Society. Montreal, Canada. June 2002.

22. Nguyen, K. “Active Control of Blade Stall”. Journal of Aircraft. Vol 35, No 1. 1998.

23. Malpica, C and Celi, R. “Simulation-Based Bandwith Analysis of a Swashplateless Rotor Helicopter”. 63rd Annual Forum and Technology Display at the American Helicopter Society International. Virginia Beach, VA. 2007.

24. Arnold, U., et al. “Development of an integrated Electrical Swashplateless Primary and Individual Blade Control System”. American Helicopter Society 63rd Annual Forum. Virginia Beach, VA. 2007.

25. Ganguli, R. Jehnert, B., Wolfram, J., Voersmann, P. “Survivability of helicopter with individual blade primary control failure”. The Aeronautical Journal. October, 2007.

26. Stevens, Patricia Lynn. “Active Interrogation of Helicopter Main Rotor Faults Using Trailing Edge Flap Actuation”. Doctoral Thesis. The Pennsylvania State University. May 2001.

27. Kiddy, Jason., Pines, Darryll. “An Eigenstructure Assignment Technique for Damage Detection in Rotating Structures”. AIAA Journal. Vol 36, Issue 9. Spet 1998.

28. http://www.griffin-helicopters.co.uk/accidents.asp?acregn=G&cause=92

29. http://www.helicoptersafety.org/commonaccidents.asp

30. Johnson, W. “Helicopter Theory”, 1st ed. Princeton University Press, Princeton , 1980

31. Gessow, Alfred., Myers, Garry. “Aerodynamics of the Helicopter”. College Park Pr. 1st Edition, 1999.

32. Prouty, R. “Helicopter Performance, Stability and Control”. Krieger Pub Co. 2002 Edition. 2001.

33. Bramwell, A. R. S., Sutton, George T., Balmford, David. “Helicopter Dynamics”. Butterworth - Heinemann. 2nd Edition. 2001.

34. Leishmann, Gordon, J. “Principles of Helicopter Aerodynamics” Cambridge University Press. 2nd Edition. 2006.

35. Howlett, J., “Black Hawk Engineering Simulation Program: Volume I”, National Aeronautics and Space Administration, 1981, NASA-CR-166309.

36. Ballin, Mark. “Validation of a Real Time Engineering Simulation of the UH-60A Helicopter. Nasa Technical Memorandum #88360. National Aeronautics and Space Administration. Februaly 1987.

37. Bailey. “Simplified Theoretical Method of Determining the characteristics of a Lifting Rotor in Forward Flight”. NACA report 716.

38. McFarland, R.E. et al. “Simulation of Rotor Blade Element Turbulence”. Nasa Technical Memorandum #108862. National Aeronautics and Space Administration. January 1995.

39. http://www.aerospaceweb.org/design/helicopter/cyclic.shtml

40. http://en.wikipedia.org/wiki/File:Blackhawk.jpg

41. http://en.wikipedia.org/wiki/File:KamowK32A.jpg

42. http://en.wikipedia.org/wiki/File:CH-47_2.jpg

43. http://en.wikipedia.org/wiki/File:DF-SN-82-00891.JPEG

44. Lorkowski et al. “Rotor Blade with Control Flaps”. United States Patent #6663345 B2. Dec. 16, 2003.

45. Straub, F. K., “A Feasibility Study of Using Smart Materials for Rotorcraft”, *Smart Materials and Structures,* Vol 5 No 1, 1995

46. Wilbur, M., Yeager, W., Wilkie, W., “Hover Testing of the NASA-Army Active Twist Rotor Prototype Blade”, 56th Annual Forum of the American Helicopter Society, Virginia Beach, VA, May 2-4, 2000.

47. Kaman, C., “Rotary/fixed wing aircraft”, Kaman Aircraft Corp, United States Patent Patent #2455866. December 1948.

48. http://collections.nasm.si.edu/media/full/A19571016000cp04.jpg

49. Domzalski et al. “Helicopter rotor blade flap actuator government interest”. United States Patent #6135713. Oct 24, 2000.

50. Shen, J., Chopra I. “Swashplateless Helicopter Rotor with Trailing Edge Flaps”, *Journal of Aircraft*, 2004, Vol 41 No 2

51. Zimmer, H., “Helicopter Rotor Blade Control”. Dornier GmbH,*United States Patent*. Patent # 4799859. January 1989

52.http://www.upwind.eu/Shared%20Documents/EWEC2007%20Presentations/070510%20WP1B3%20Harald%20Bersee.pdf

53. Arnold, U.T.P., Neuheuser, T., Bartels, R., “Development of an Integrated Electrical Swashplateless Primary and Individual Blade Control System”, Proceedings of the American Helicopter Society, Virginia Beach, VA.May 1-3 2007

54. http://www.aviationweek.com/aw/blogs/defense/index.jsp?plckController=Blog&plckScript=blogScript&plckElementId=blogDest&plckBlogPage=BlogViewPost&plckPostId=Blog%3a27ec4a53-dcc8-42d0-bd3a-01329aef79a7Post%3a1224e60e-4c96-4213-a896-82d0b35c9709

55. Tamayo, Sergio., Perhinschi, Mario. “A Simulation Environment for Individual Blade Control Helicopters“ AIAA Conference in Modeling and Simulation Technologies. Chicago, IL. August, 2009.

56. Takashi, M. D. “A Flight-Dynamic Helicopter Mathematical Model with a Single Flap-Lag-Torsion Main Rotor”. Nasa Technical Memorandum 1C2267. National Aeronautics and Space Administration. February 1990.

57. Tamayo, Sergio., Zinchiak, Andrew., Perhinschi, Mario G. “Development of Linear Models for Individual Blade Control Helicopter” submitted to the AIAA Conference in Modeling and Simulation Technologies. Portland, OR. August, 2011.

58. Padfield, Gareth D. “Helicopter Flight Dynamics: The Theory and Application of Flying Qualities and Simulation Modeling” AIAA Education Series. 1996.

59. McFarland, M., Calise, A. “Neural Networks and Adaptive Nonlinear Control of Agile Antiair Missiles”. Journal of Guidance, Control, and Dynamics. Vol 23, No 3. 2000.

60. Calise, A. J., Lee, S., Sharma, M. “Development of a reconfigurable Flight Control Law for Tailless Aircraft”. Journal of Guidance, Control, and Dynamics. Vol 24., No.5. 2001.

61. Leitner, J., Calise, A., Prasad, J. V. R. “Analysis of Adaptive Neural Networks for Helicopter Flight Control”. Journal of Guidance, Control, and Dynamics. Vol 20, No. 5. 1997.

62. Tamayo, Sergio., Perhinschi Mario G. “Simulation of Individual Blade Control Helicopter for Analysis of Fault Tolerance Capabilities”. AIAA Conference in Modeling and Simulation Technologies. Toronto, CA. August, 2010.

63. Erdman, A. G., Sandor, G. “Mechanism Design: Analysis and Synthesis”. Fourth Edition. Prentice Hall. 2001. Conference on Evolutionary Computation (ICEC-94). IEEE. 1994.

64. Zhang, Byoung-Tak., Mühlenbein, Heinz. “Synthesis of Sigma-Pi Neural Networks by the Breeder Genetic Programming”.

65. Khalil, H. “Nonlinear Systems”. MacMillan, New York, 1992.

66. Johnson, Eric., Calise, Anthony. “Pseudo Control Hedging: A New Method for Adaptive Control”. Advances in Navigation Guidance and Control Technology Workshop. Redstone, Alabama. November 1-2, 2000.